FACULTY
OF MATHEMATICS
AND PHYSICS
Charles University

DOCTORAL THESIS

Gergely Németh

Investigation of titanium alloys using neutron diffraction

Department of Physics of Materials

Supervisor of the doctoral thesis: prof. RNDr. Kristián Mathis, Ph.D., DrSc.

Study programme: Physics

Specialization: Physics of Condensed Matter and
Materials Research

Prague 2021

I declare that I carried out this master thesis independently, and only with the cited sources, literature and other professional sources.

I understand that my work relates to the rights and obligations under the Act No. 121/2000 Coll., the Copyright Act, as amended, in particular the fact that the Charles University has the right to conclude a license agreement on the use of this work as a school work pursuant to Section 60 paragraph 1 of the Copyright Act.

In Prague 01/06/2021 Gergely Németh

Acknowledgements

In the first place, I would like to express my huge appreciation above all to my supervisor Prof. Krisztián Máthis for his constant support, active guidance and inspirative approach during my studies. His deep expertise and immense knowledge have continually encouraged me.

My gratitude also goes to my colleagues at the Department of Physics of Materials for their valuable advice and discussions. Especially, I am thankful to Dr. Fekete for her helpful attitude during electron microscopy investigations. I also appreciate the help of Dr. Jozef Veselý with transmission electron microscopy measurements and the expertise of Ing. Jana Kálalová and Marta Čepová during sample preparations.

Moreover, I am incredibly grateful to Dr. Pavel Strunz who introduced me to the practical aspects of neutron diffraction technique. I would like to thank my colleague and friend Dr. Farkas whose insightful comments and suggestions were extremely helpful. My gratitude extends to colleagues at the Department of Neutron Physics at the Nuclear Physics Institute of the Czech Academy of Science for their helpfulness.

Also, I would like to thank COMTES FHT a.s. for providing the studied material.

Last but not least, I owe a debt of gratitude to my family, friends and especially to my wife, Michaela, for their support, faith and encouragement.

Title: Investigation of titanium alloys using neutron diffraction

Author: Gergely Németh

Department / Institute: Department of Physics of Materials

Supervisor of the master thesis: prof. RNDr. Kristián Mathis, Ph.D., DrSc.,
Department of Physics of Materials

Abstract: Titanium grade 2 was treated by multiple passes of the continuous equal-channel angular pressing technique (CONFORM ECAP) and, after each pass, additionally by rotary swaging. The residual strain field in samples processed by only CONFORM ECAP was studied by neutron diffraction strain scanning. In order to elucidate the microscopic background and calculate the related residual stress field, the local microstructure was thoroughly investigated by various experimental techniques. The microstructure and the deformation behavior of the rotary swaged samples was studied by transmission electron microscopy and by in-situ neutron diffraction during compression.

The results of the analyses indicated that microstructural gradients were present in the material as the result of the inhomogeneous deformation during the CONFORM ECAP treatment. These gradients were identified as the main reason of the presence of residual stress fields. The distributions of stress fields calculated based on microstructural parameters were in correlation with simulation results. The additional rotary swaging treatment resulted in a nanocrystalline grain structure with increasing homogeneity as the number of previous CONFORM ECAP passes increased. Deformation twinning was identified as a major deformation mechanism whose role was gradually reduced by the decreasing overall grain size.

Keywords: Titanium, severe plastic deformation (SPD), residual stresses, neutron diffraction, deformation twinning

Název práce: Studium slitin titanu s využitím neutronové difrakce

Autor: Gergely Németh

Katedra: Katedra fyziky materiálů

Vedoucí disertační práce: prof. RNDr. Kristián Mathis, Ph.D., DrSc., Katedra fyziky materiálů

Abstrakt: Titan grade 2 byl zpracován vícery průchody kontinuální metodou protlačování lomeným kanálem stejného průřezu (CONFORM ECAP) a po každém průchodu navíc rotačním kováním. Pole zbytkové deformace ve vzorcích zpracované pouze CONFORM ECAP-em bylo studované skenem neutronové difrakce. Za účelem objasnění mikroskopického pozadí a vypočítání souvisejícího pole zbytkového napětí byla lokální mikrostruktura podrobně prozkoumaná různými experimentálními technikami. Mikrostruktura a deformační chování rotačně kovaných vzorků byly zkoumány transmisním elektronovým mikroskopem a in-situ neutronovou difrakcí během stlačení.

Výsledky analýz naznačili, že gradienty mikrostruktury byly přítomny v materiálu jako důsledek nehomogenní deformace během CONFORM ECAP-u. Tyto gradienty byly identifikovány jako hlavním důvodem přítomnosti zbytkových napěťových polí. Rozložení napěťových polí vypočítané na základě mikrostrukturních parametrů byla v korelaci s výsledky simulací. Dodatečné rotační kování mělo za následek nanokrystalickou strukturu zrn s rostoucí homogenitou odpovídající zvyšujícímu se počtu předchozích CONFORM ECAP průchodů. Deformační dvojčatění bylo identifikováno jako jedno z hlavních deformačních mechanismů, jehož role se postupně snižovala podle zmenšování celkové velikosti zrn.

Klíčová slova: Titan, intenzivní plastická deformace (SPD), zbytková napětí, neutronová difrakce, deformační dvojčatění

Contents

Preface

The excellent properties of titanium and its alloys, such as corrosion resistivity, nontoxicity in biological environment, low density and high strength enables its extensive use in many industrial fields. Owing to its biocompatibility combined with high strength, the role of titanium as structural material in body implants is essential in the biomedical industry [1]. However, in some cases, the strength needs to be further increased, which can be conventionally achieved by alloying. It has been shown that some of the extensively used alloying elements can be potentially harmful if they are released in human body which in the end sets boundaries for biocompatible use. Therefore, there is an increased scientific demand for new approaches by which the desired mechanical properties of titanium can be obtained.

Through grain refinement and increased lattice defect concentration, severe plastic deformation processes have been proved as very successful techniques to prepare ultra-fine grained polycrystalline materials with enhanced mechanical properties [2]. Among these techniques, the most widely used method is the equal-channel angular pressing (ECAP). In this method, the material is severely deformed by pressing through two intersecting channels. The advantage of using ECAP is that the geometrical integrity of the billet is kept in contrast to other processes like extrusion [3]. Nevertheless, the limited dimensions of specimen and the limited industrial scale application of ECAP can be classified as a main disadvantage. This can be overcome by CONFORM ECAP (C-ECAP) technique [4]. This is a combination of the continuous forming and the conventional ECAP, where the billet is pressed through a curved die by friction forces. At the exit of the die, the regular ECAP process is applied as the specimen is forced to turn to leave the die channel. A study shown that after the application of C-ECAP, a heterogeneous microstructure with distorted and defect free grains was achieved [5]. This can indicate an in-homogeneous deformation in the samples volume which leads to the rise of residual stress fields in specimens [6].

The presence of residual stresses may be responsible for many negative changes in engineering components during their service time, such as distortion or even crack initiation and premature failure. Therefore, their study is inevitable in cases where the replacement of components is problematic such as implants in human body.

Diffraction based techniques, such as neutron or synchrotron radiation, turned to be as successful probes in the mapping of residual stress field in bulk specimens due to their large penetration depth in materials [7]. However, the accurate representation and elucidation of the origin of these stresses requires additional experimental methods.

In some applications, C-ECAP processed materials can be considered as semi-finished products. Therefore, wire drawing methods, like rotary swaging can be applied to achieve the desired shape. This further treatment often results in nanocrystalline structured materials, which deformation response can be different compared to coarse- or fine-grained counterparts [8]. Therefore, the study of their deformation mechanism is of key importance in the further potential applications. In-situ neutron diffraction can help in this since it provides representative information about the microstructure from the whole bulk in contrast to microscopic methods.

1 Theoretical background

1.1 Basic properties and applications of titanium

Titanium is a shiny, silver colored metal which is the 9th most abundant element on Earth. It can exist in the form of mineral sands which contain ilmenite ($FeTiO_3$) or rutile (TiO_2). Some basic physical properties of high purity Ti at 25°C are listed in the Table 1.1. Ti was discovered by William Gregor in 1791 and it was first isolated in pure form by Matthew Albert Hunter in 1910. The invention of the industrial production of Ti belongs to Wilhelm Justin Kroll, who developed the so-called "Kroll process" in 1932 [9].

Density	4.51 g/cm^3
Elastic modulus	105 GPa
Shear modulus	44 GPa
Poisson ratio	0.33
Thermal expansion coefficient	8.36 10^{-6} K^{-1}
Thermal conductivity	14.99 W/mK]
Specific heat capacity	523 J/kgK
Electrical resistance	564.9 [10^{-9} Ωm]

Table 1.1 Basic properties of Ti

Ti and its alloys belong to the lightweight structural metals. Their strength is comparable to some of the commonly used types of steels, but they possess much lower density [9]. They can reach even 200 MPa/gcm^{-3} at room temperature. This property enables Ti alloys to be used in engineering areas where weight reduction is required while keeping mechanical performance high. Ti has also high melting point (1670 °C) as compared to other lightweight structural metals like aluminum (660°C) or magnesium (650°C). Thus, Ti has advantage over the mentioned metals in higher temperature structural applications. However, oxygen is highly reactive with Ti and because of this the maximum use temperature cannot exceed more than 550°C. Beyond this temperature, oxygens diffusion is accelerated, and the oxygen enriched part of the material becomes brittle [10]. On the other hand, the thin Ti oxide layer formed on the surface during the oxidation process at ambient temperature protects the rest of the material in various environments. Thanks to this layer, this material is excelling with corrosion resistance for example in human body or sea water.

These excellent properties make Ti and its alloys a widespread used structural material. Their commercial use is concentrated mainly in the aerospace industry, but automotive, chemical, power, sport, and jewelry industry together with medicine could find their application also.

1.2 Titanium equilibrium phases and alloy classification

Pure Ti has two stable structural modifications: a hexagonal (hcp) α phase at lower temperatures and a body-centered β phase at higher temperatures (Fig.1.1). The lattice parameters of the α phase are a=2,95 Å and c=4,68 Å at room temperature [11]. The resulting c/a ratio is 1.586 which is smaller than the ideal value for hcp structure $\left(\sqrt{\frac{8}{3}} \cong 1.633\right)$. In the case of BCC β phase the lattice parameter is a=3.31 Å at 1000°C [12]. The α and β phase has space group $P6_3/mmc$ and $Im\bar{3}m$, respectively.

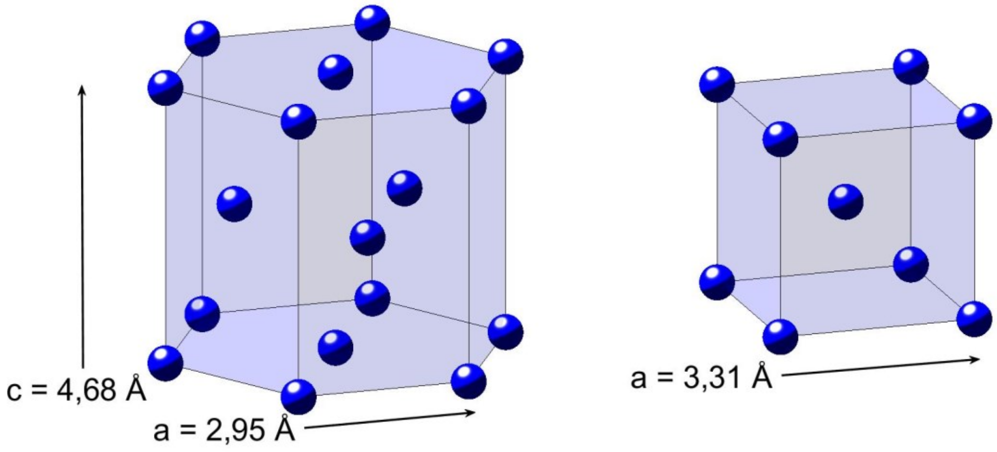

Fig. 1.1 HCP and BCC unit cells of Ti

At atmospheric pressure, the allotropic transformation of pure Ti occurs at temperature 882°C. By adding so called α/β stabilizing elements, this temperature can be shifted. Elements like Al, O, C, N, Ga, Ge belong to α stabilizers and they shift the transformation temperature upwards while β stabilizers are decreasing it. Two family of β stabilizers exist depending on the nature of the resulting binary phase diagram. Mb, V, Nb, Hf and Ta are parts of β-isomorphous stabilizers. β-eutectoid stabilizers include e.g. Fe, Cr, Si, Ni, Mn and Cu. Elements like Sn, Zr and Hf have no or very small effect on the transformation temperature. Depending on the alloying element concentration and the resulting phases at room temperature, generally, Ti alloys are divided into α, β and α+β alloys.

1.2.1 Commercially pure titanium

Commercially pure (CP) Ti belongs to α alloys, since they contain only limited amount of alloying elements and the α phase dominates the microstructure at room temperature. According to American Society for Testing and Material (ASTM) CP Ti is divided into four grades depending on O and Fe content (table 1.2) [10]. The presence of Fe can be surprising since it belongs to β stabilizers. It can be added deliberately, or it can be diffused during the preparation process. Nevertheless, due to low solubility in α phase, Fe forms dispersed β phase particles, which prevent the grain growth of the α phase during recrystallization [10].

	Grade 1	Grade 2	Grade 3	Grade 4
O [wt.%]	0.18	0.25	0.35	0.40
Fe [wt.%]	0.20	0.30	0.30	0.50

Table 1.2 Grade classification of CP Ti

CP Ti is primarily used in industrial fields, where its excellent corrosion resistance and good general workability can stand out. Therefore, their main usage is focused primarily in chemical and petrochemical industry as tubing material. Nevertheless, novel processing techniques enables to increase mechanical properties of CP Ti almost on the same level of the famous Ti-4Al-6V alloy [13]. This makes

CP Ti an attractive material in fields where increased mechanical properties are required also.

The mechanical properties of CP Ti can be controlled by slight altering of the composition or by thermo-mechanical processing. In the first case, for example the increasing O content (higher grades) increases the yield strength, however, the ductility is reduced [14, 15, 16]. The yield strength of CP Ti grade 4 can be almost three times higher (from 170 MPa to 480 MPa) than of CP Ti grade 1 while the O content is doubled (from 0.18 wt.% to 0.4 wt.%) [10].

The processing methods involve various thermomechanical treatments, which enable to control the texture formation and/or the grain size. This can be achieved by application of severe plastic deformation processes without any change in the chemical composition (see chapter 1.4). As a brief introduction, it is worth to mention in a few words which mechanisms are essentially responsible for changed mechanical properties of CP Ti in this case.

It is well-known that textured hcp metals possess mechanical anisotropy due to their hcp lattice and its limited deformation mechanisms [17, 18]. The mechanical response is strongly connected with the mutual orientation of loading axis and the $\vec{c}$ direction of the hcp crystallites, as it was shown for the textured CP Ti also [19, 20, 21].

The second thermomechanical processing approach to control CP Ti’s mechanical properties leads through grain boundary strengthening. Grain boundaries of a polycrystalline material are obstacles for dislocation motion which is responsible for plastic deformation of materials.

More detailed explanation of these mechanisms will be given in later chapters (chap. 1.3 and 1.4).

1.3 Deformation mechanisms in hcp metals and in pure α titanium

The mechanical behavior of metals is very closely related to their deformation mechanisms occurring at microscopical scale. In hcp metals, dislocation slip and twinning are the effective plastic deformation carriers.

1.3.1 Dislocation slip modes in α titanium and other hcp metals

In hcp structure, the most closely packed direction is the $\langle 11\bar{2}0\rangle$ and the most densely packed planes, which contain this direction, are basal (0001), prismatic $(10\bar{1}0)$ and pyramidal $(10\bar{1}1)$. These three planes with a given type of burgers vector altogether give 12 slip systems: three from basal, three from prismatic and six from pyramidal slip system. However, if considering the independence of each slip system, this number can be further reduced to only 4 independent slip systems.

Taking into account the Von Mises criterium [22], which states that at least 5 independent slip systems are needed for homogenous plastic deformation of polycrystals, then at least, one of the non-basal burgers vector needs to be active. This can be a $\vec{c}$ or a $\vec{c}+\vec{a}$ type. The latter type is favorable since it can provide deformation in $\vec{a}$ and in $\vec{c}$ direction too. This type of dislocations has been observed experimentally in various α titanium alloys [23, 24] and also in other hcp metals like Zn, Cd and Mg [25]. The possible slip planes containing $\vec{c}+\vec{a}$ type burgers vector are the $(10\bar{1}1)$ and $(11\bar{2}2)$ planes. The basic characteristics of the main slip systems are summarized in the Table 1.3 and schematically they can be seen in Fig. 1.2.

Name	Slip plane	Burgers vector type	Total number of slip systems	Number of independent slip systems
Basal	(0002)	$\langle 11\bar{2}0\rangle$	3	2
Prismatic	$(10\bar{1}0)$	$\langle 11\bar{2}0\rangle$	3	2
Pyramidal	$(10\bar{1}1)$	$\langle 11\bar{2}0\rangle$	6	4
1st Pyramidal	$(10\bar{1}1)$	$\langle 11\bar{2}3\rangle$	12	4
2nd Pyramidal	$(11\bar{2}2)$	$\langle 11\bar{2}3\rangle$	6	5

Table 1.3 Basic parameters of main slip systems in α-Ti

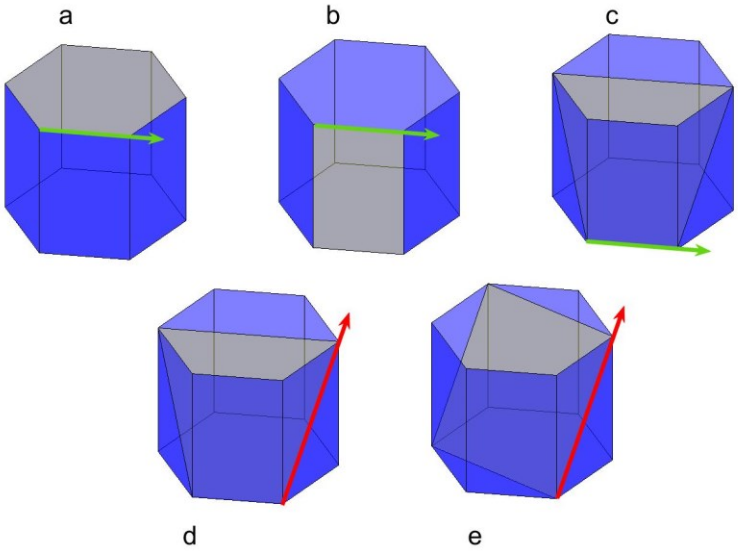

Fig. 1.2 Possible slip systems in hcp metals. (0002), $(10\bar{1}0)$ and $(10\bar{1}1)$ slip planes with Burger's vector $\vec{a} = \langle 11\bar{2}0 \rangle$ are shown on *a, b* and *c*, respectively. $(10\bar{1}1)$ and $(11\bar{2}2)$ slip planes with Burger's vector $\vec{c} + \vec{a} = \langle 11\bar{2}3 \rangle$ in *d* and *e*

Generally, the c/a ratio of a given hexagonal structure has a large effect on a given mechanism of the plastic deformation due to the longer or shorter distances between atoms in a particular plane. In materials like Ti, Zr, Gd, Y where the c/a ratio is significantly lower than the ideal, the principal slip plane for $\vec{a} = \langle 11\bar{2}0 \rangle$ and $\vec{c} + \vec{a} = \langle 11\bar{2}3 \rangle$ type dislocations are the prismatic $(10\bar{1}0)$ and pyramidal $(10\bar{1}1)$ planes, respectively. While in materials like Zn, Cd which possess larger c/a ratio, or in materials with almost the ideal c/a ratio like Mg, Co, the principal slip plane for the same types of burgers vectors are basal (0001) and 2nd order pyramidal $(11\bar{2}2)$ planes, respectively [26].

As it was mentioned earlier, to fulfill the Von Mises criterium, the activation of slip systems with $\vec{c} + \vec{a}$ type of burgers vector is needed. However, at the ambient temperature, the critical resolved shear stress (CRSS) of these systems are generally much higher than for slip systems with $\vec{a}$ type burger vector [27]. Therefore, in a texture free polycrystalline material, the $\vec{c} + \vec{a}$ slip will be activated only a limited number of grains. Nevertheless, due to thermal activation at higher temperatures or due to the presence of alloying elements, the difference between CRSS of the two types of slips can be reduced [28].

1.3.2 Mechanical twinning in α titanium and other hcp metals

The additional deformation mechanism, which provides deformation in direction $\vec{c}$ is mechanical twinning. In the meaning of crystal lattice geometry, twinning is a phenomenon when a part of a lattice flips to mirror symmetrical position with respect to the original crystal. From the deformation point of view, it is a homogeneous simple shear of the parent lattice. The twinned part is basically identical to the parent lattice, just it has different orientation. Furthermore, the parent and twinned part of the crystal shares a common plane, which is called twin or mirror plane.

According to their origin, generally three types of twins can be distinguished in materials:

- During crystal growth, *growth twins* may appear
- Recrystallization or heat treatment can cause *annealing twins* in the material
- In the loaded material, *mechanical twins* can nucleate

To uniquely characterize each twinning mode, certain crystallographic planes and directions can be selected. These are called invariants and they give the geometry description of twinning shear: κ_1, η_1, κ_2, and η_2 (Fig.1.3). κ_1 is the twinning plane, or mirror plane. This plane also contains the shear direction η_1. The second invariant plane is κ_2 and it is denoted as conjugate plane. This plane holds the so-called conjugate shear direction η_2. Normals of planes κ_1 and κ_2 with η_1 defines the plane of shear *S*. During twinning, κ_2 is rotated to κ_2' together with η_2 to η_2'. κ_2 and κ_2' are inclined to κ_1 by θ. From these four invariants, only two are independent, κ_1 and η_2 or κ_2 and η_1. The shear magnitude g is function of θ, precisely $g = 2\cot\theta$ [29].

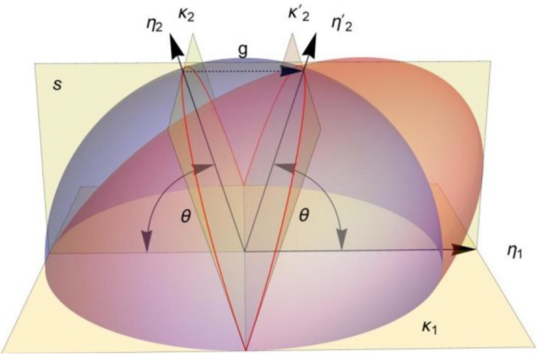

Fig. 1.3 Geometric description of twinning shear. Taken from [30]

During twinning, the magnitude of the displacement of atoms is dependent on the atoms position from the twinning plane and generally it is not an integer number of interatomic distances (Fig. 1.4). To recover the original lattice after twinning, both shear and small displacement of atoms are needed. These small displacements are called *shuffles*. Thus, twinning is a qualitatively and quantitatively different mechanism than in the case of dislocation slip, where the displacement is characterized by burgers vector, which is exactly one interatomic distance in a certain plane. Moreover, twinning involves sudden, coordinated movement of atoms in the three-dimensional volume while during slip the changes in the lattice occurs only in a certain crystallographic plane. Another important feature of twinning is its polarity. This means that for a given orientation of a crystal different twinning modes are activated in uniaxial compression or tension. The amount shear *g,* carried by a certain twinning mode, can be expressed as a function of $\gamma = c/a$.

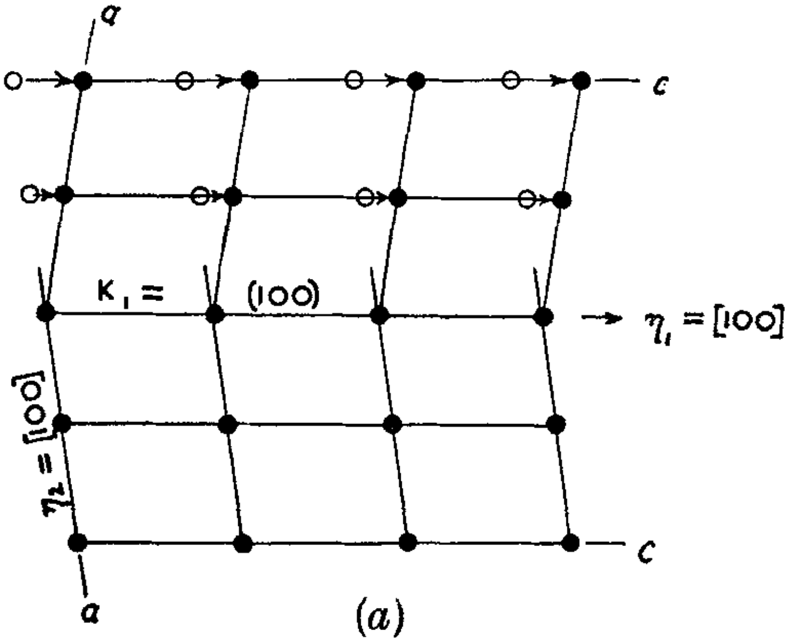

Fig. 1.4 Displacements of atoms during twinning [29]

In hcp metals, mainly four twinning modes are observed experimentally (Table. 1.4). However, the number of predicted twinning modes in hcp metals is 18 [31].

κ_1	η_1	κ_2	η_2	S	g
$\{11\bar{2}2\}$	$1/3\,\langle 11\bar{2}\bar{3}\rangle$	$\{11\bar{2}\bar{4}\}$	$1/3\,\langle 22\bar{4}3\rangle$	$\langle 1\bar{1}00\rangle$	$\dfrac{2(\gamma^2-2)}{3\gamma}$
$\{10\bar{1}2\}$	$\pm\langle 10\bar{1}\bar{1}\rangle$	$\{\bar{1}0\bar{1}2\}$	$\pm\langle 10\bar{1}1\rangle$	$\pm 1/3\,\langle 1\bar{2}10\rangle$	$\dfrac{\gamma^2-3}{\gamma\sqrt{3}}$
$\{10\bar{1}1\}$	$\langle 10\bar{1}\bar{2}\rangle$	$\{10\bar{1}\bar{3}\}$	$\langle 30\bar{3}2\rangle$	$1/3\,\langle 1\bar{1}00\rangle$	$\dfrac{4\gamma^2-9}{4\gamma\sqrt{3}}$
$\{11\bar{2}1\}$	$1/3\,\langle \bar{1}\bar{1}26\rangle$	(0002)	$1/3\,\langle 11\bar{2}0\rangle$	$\langle 1\bar{1}00\rangle$	$\dfrac{1}{\gamma}$

Table 1.4 The four main twinning modes with their invariants and induced shear deformations *g*

Twinning modes can be classified into two groups depending on their effect in the $\vec{c}$ direction of the crystallites. If a particular twinning mode causes shortening in this direction, then it is called *contraction twinning*. The opposite effect, i.e. lengthening in the $\vec{c}$ direction, is caused by the activation of *tensile twinning*. The classification of each twinning mode for a certain hcp material is dependent on materials c/a ratio, as it can be seen in Fig. 1.5 or in tab. 1.4 in the last column. Twinning mode $\{10\bar{1}2\}\pm\langle 10\bar{1}\bar{1}\rangle$ acts as tension twinning mode in materials like Ti, Mg, Co, Zr ($\gamma < \sqrt{3}$) and in materials Zn and Cd ($\gamma > \sqrt{3}$) acts as contraction twinning mode. The rest twinning modes have the same character for every mentioned hcp materials, i.e. $\{11\bar{2}1\}\,1/3\,\langle\bar{1}\bar{1}26\rangle$ is tension twinning, while $\{10\bar{1}1\}\langle 10\bar{1}\bar{2}\rangle$ and $\{11\bar{2}2\}\,1/3\,\langle 11\bar{2}\bar{3}\rangle$ are contraction twinning mode.

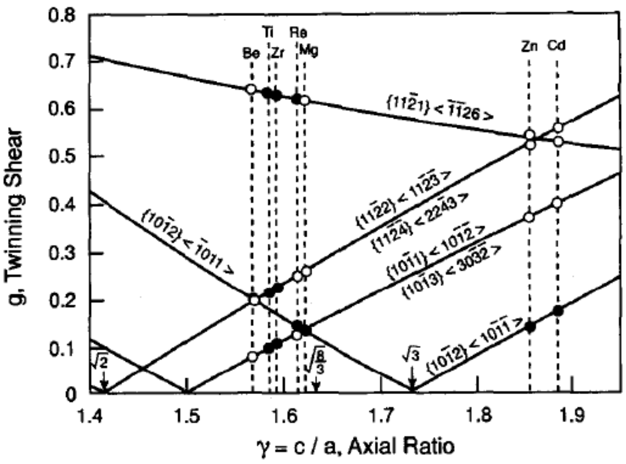

Fig. 1.5 Twinning shear as function of the c/a ratio. Negative slope represents tension twinning [32]

For α Ti, all of the above listed twinning modes have been reported. They are schematically shown in Fig. 1.6 together with the calculated shear *g* and the angle between $\vec{c}$ direction of the original and twinned lattice for α Ti. According to Backofen and Paton [33], $\{11\bar{2}2\}\,1/3\,\langle 11\bar{2}\bar{3}\rangle$ compression twins are dominantly active in the temperature region between room temperature and 300°C while $\{10\bar{1}1\}\langle 10\bar{1}\bar{2}\rangle$ twins are active above 400°C. Glavicic et al [34] estimated the relative proportion of $\{11\bar{2}2\}\,1/3\,\langle 11\bar{2}\bar{3}\rangle$, $\{10\bar{1}2\} \pm \langle 10\bar{1}\bar{1}\rangle$ and $\{11\bar{2}1\}\,1/3\,\langle \bar{1}\bar{1}26\rangle$ twins during cold rolling of CP Ti at 20°C as 40%, 30% and 30% respectively. However, the volume fraction of twins decreased rapidly as the rolling temperature increased. S. Zaefferer studied the active deformation systems of Ti with different O content and found that with increasing presence of O, the twinning activity is suppressed [35]. This is also true for Al addition, as it was showed by Williams et al [28]. In both cases, the twinning was substituted by activation of $\vec{c}+\vec{a}$ type dislocation slip.

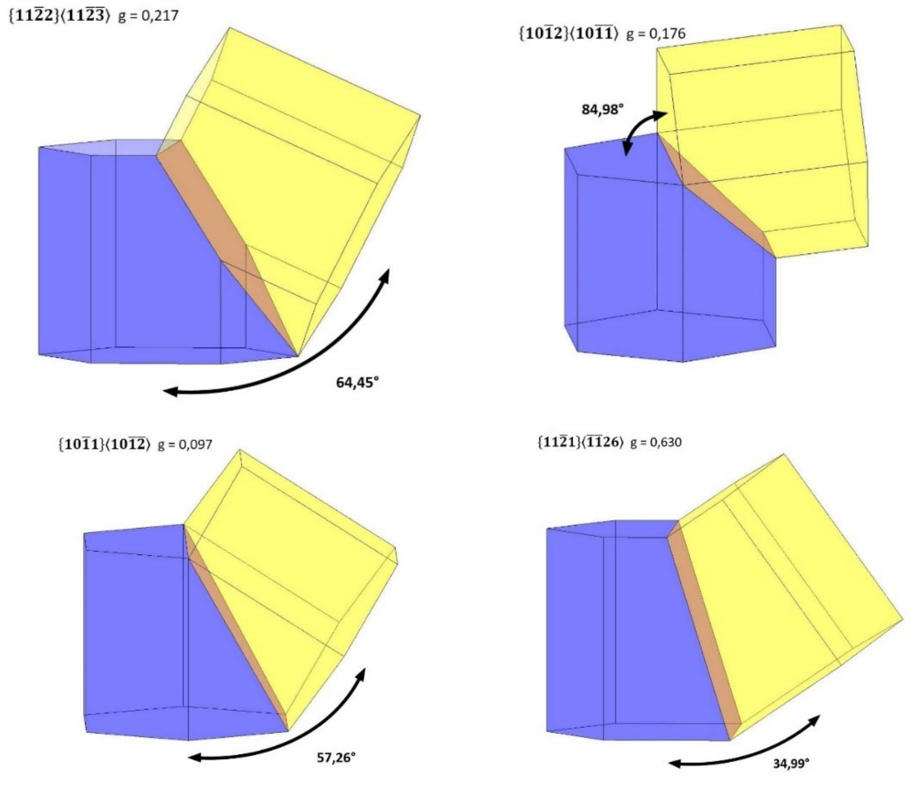

Fig. 1.6. Twins in α Ti. Blue is the parent lattice, yellow is the twinned lattice

1.4 Metal forming processes: CONFORM ECAP and Rotary Swaging

Metal forming processes are widespread used bulk forming tools to produce structural parts having particular geometry. Concurrently, alternation of the mechanical properties can be achieved. A subset of metal forming processes, so called *severe plastic deformation* (SPD) processes, are highly effective methods to produce bulk ultra-fine grained (UFG) materials. This SPD processed materials exhibits higher strength, crack initiation and fatigue resistance. However, their ductility is often limited [36, 37]. During the SPD process, very large plastic strain is imposed on the material and large number of crystal defects are generated [38]. The rearrangement of the dislocation structure to low energy configurations, such as low angle grain boundaries, takes place.

Consequently, the UFG structure has an in increased density of grain boundaries. These serve as obstacles for dislocation propagation during straining and hence strengthening occurs. The relation between the yield strength $\sigma_{0,2}$ and the mean grain size d is the well-known Hall-Patch equation (1) [39, 40]:

$$\sigma_{0,2} = \sigma_0 + kd^{-\frac{1}{2}} \tag{1}$$

σ_0 and k are the friction stress and a material constant, respectively.

The most widely used SPD methods are the Equal-Channel Angular Pressing (ECAP), High Pression Torsion (HPT) and Accumulative Roll Bonding (ARB). The ECAP process was introduced by Segal V. M. [41] and further developed by Valiev [42]. The beginnings of HPT can be dated to 1943 when Bridgman published its finding that a bar could bear more torsion in the presence of longitudinal compression than without it [43]. Nevertheless, HPT has been used as SPD method for grain refinement only in the last 30 years [44]. The ARB process developed by Saito is basically a repeated rolling process [45]. After every rolling session, the sheet is cut half and stacked together. The next rolling session is fed by the stacked sheet.

The above-mentioned processes are the conventional methods which form the basic principles of other advanced techniques. These can be combinations of standard metal forming processes like extrusion with conventional SPD techniques, or a combination of two kinds of basic SPD processes[46].

In the next chapter the principle of the conventional ECAP will be discussed in detail because it gives the basic principle of a more advanced technique, called CONFORM ECAP which is relevant for the present thesis.

1.4.1 ECAP and CONFORM-ECAP

CONFORM ECAP is a relatively novel technique, which enables to produce UFG materials in industrial scale. It is based on the conventional ECAP thus first this is discussed.

During the ECAP process, a billet is pressed through two intersecting channels with the same cross section (Fig.1.7 a). In the most cases, the inner angle Φ between the two channels is 90° or 120°. Since the channels have the same cross section, the process on the same billet can be repeated many times. The outer curvature angle Ψ represents the sharpness of intersection at the bottom part.

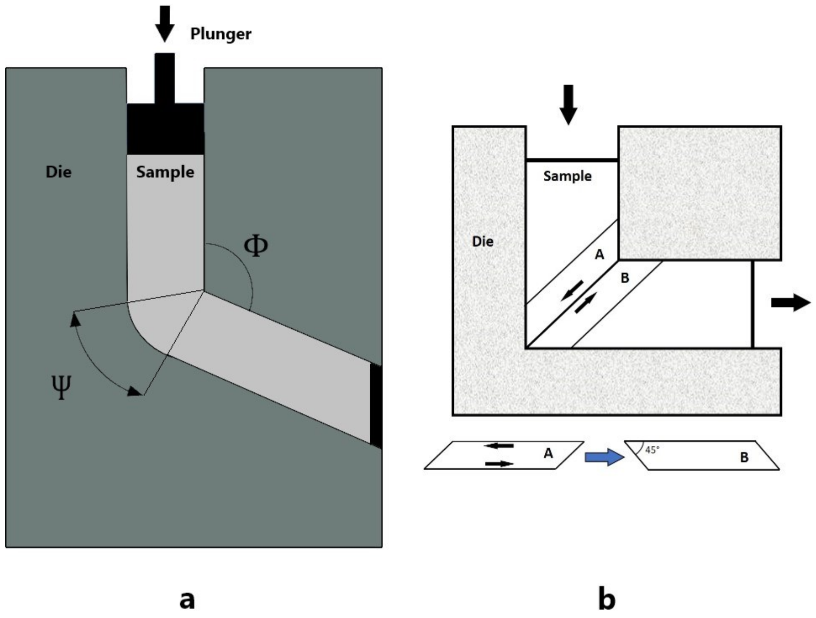

Fig. 1.7 *a* general scheme of the ECAP die design, *b* scheme of the shear deformation in a die with $\Phi = 90°$ and $\Psi = 0°$

When the sample passes through the channels, it deforms by shear on a plane which is inclined from the cross-section plane by half angle of the inner angle of channels intersection (i.e. by 45° if $\Phi = 90°$ Fig.1.7 b). The equivalent imposed strain ε_N after *N* passes through the ECAP die depends on the die parameters and can be calculated by the following equation (2) [47]:

$$\varepsilon_N = \frac{N}{\sqrt{3}}\left[2\cot(\Phi/2 + \Psi/2) + \Psi\csc(\Phi/2 + \Psi/2)\right] \qquad (2)$$

Between each passes the sample can be rotated around its longitudinal axis which also changes the shear plane in the sample (Fig. 1.8). Route A corresponds to state when no rotation is applied. If route B_C is applied, then sample is rotated by 90° in the same direction between each pass, while if the 90° rotation has alternating direction, then it is called route B_A. When the sample is rotated by 180° then it is referred by route C.

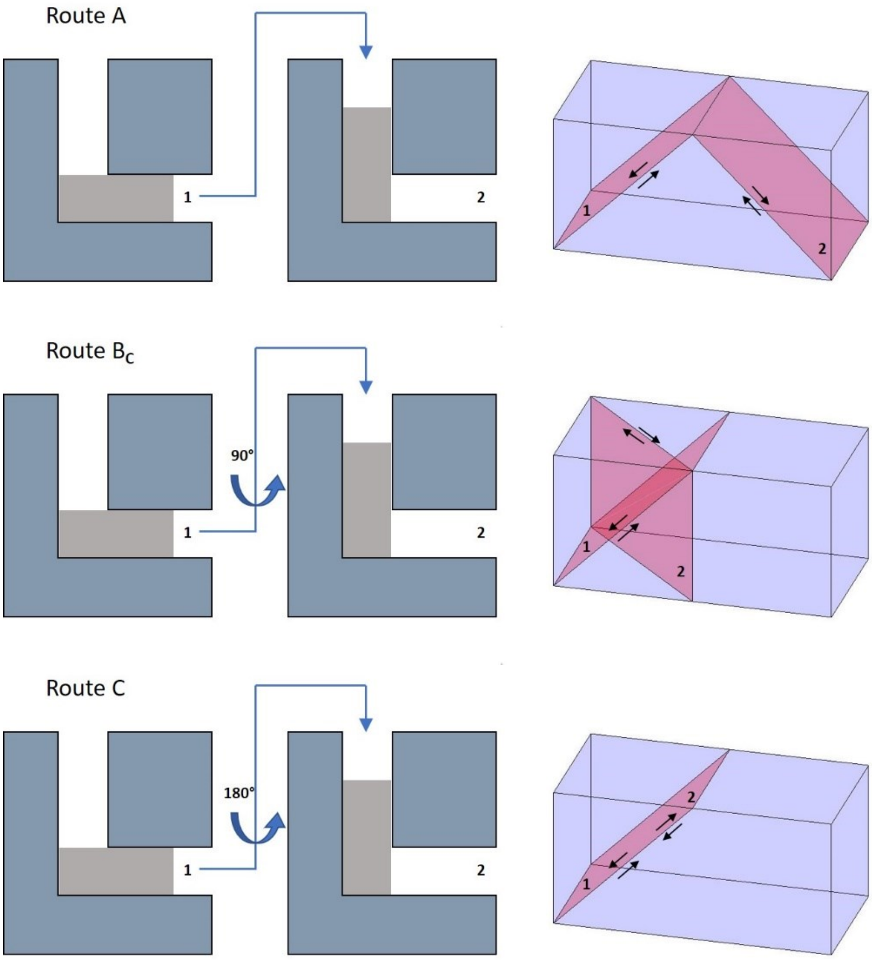

Fig. 1.8 Scheme of different routes with indicated shear planes in the work-piece after the first and second pass

Since its invention, the conventional ECAP was successfully applied on many different materials at different processing temperature resulting in UFG microstructure [48, 49, 50, 51]. Even though it is capable to produce bulk UFG materials for structural applications, the conventional die design has some dimension limitations. The length to diameter ratio of the sample is upper limited by a critical value otherwise it will not pass through the bended channel. The increasing diameter of the sample increases also the force required to press the sample through the die. However, the maximum applicable force is limited by die which can bear without breaking. Moreover, a significant part of both ends of the sample is not utilizable due to the present macro-crack and non-uniform microstructure. This makes conventional ECAP a discontinuous process and not applicable in commercial use.

These limitations were overcome by introduction the so-called CONFORM ECAP (C-ECAP) technique developed by Raab and his colleagues [52]. This technique combines the continuous extrusion, introduced by Etherington, with the principle of ECAP (Fig 1.9 a). During the C-ECAP process, a long rod is driven forward in a curved die by friction forces until it reaches the abutment. At this position the principle of the ECAP is applied since the work-piece is forced to turn an angle by shear. The length of the rod in this die design can be even several meters which is a huge improvement compared to the conventional ECAP.

The die concept by Raab was slightly modified at company COMTES FHT a.s. (Fig. 1.9.b). In their die design, the feedstock is fed from the top of die, while in the original design it was fed from the bottom of the die. They successfully applied this method on CP-Ti grade 2 and 4, producing UFG microstructure in both materials [13, 53, 54].

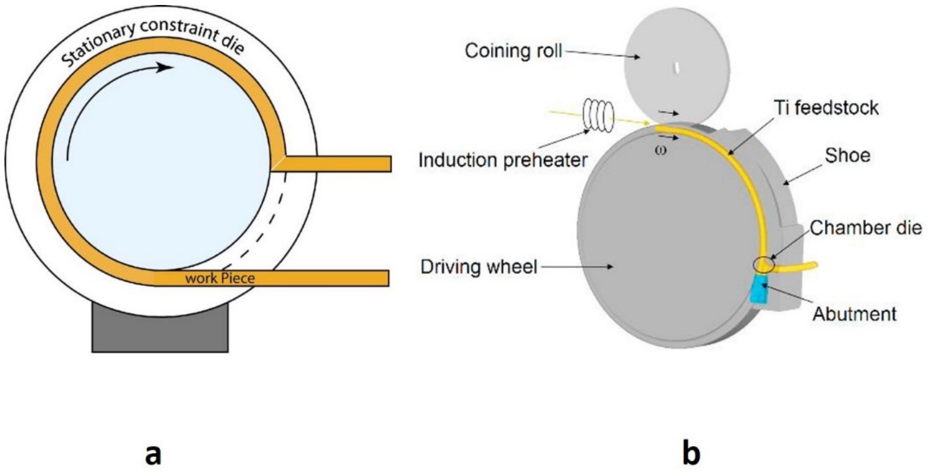

Fig.1.9 *a* Scheme of CONFORM ECAP by Raab [52] and *b* by COMTES FHT a.s. [53]

1.4.2 Rotary Swaging

C-ECAP-ed rods can be considered as semi-finished products, which often require further manufacturing process to achieve the desired geometry or even more increase their mechanical properties. One of these processes can be rotary swaging which is used for precision forming of tubes or wires [55]. It is an open forging and net-shape forming process. During rotary swaging, dies arranged uniformly around the circumference of the rod are simultaneously stroking the work-piece with high frequency in radial direction. At the same time, they are revolving around axial direction (Fig. 1.10). The number of stroking dies can be three, four or eight.

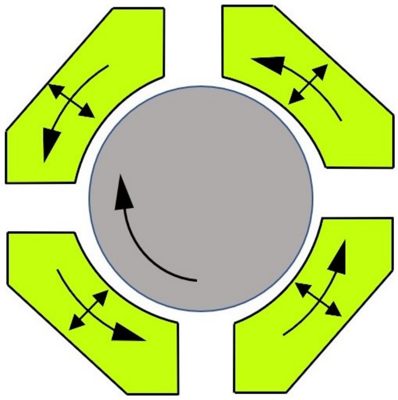

Fig. 1.10 Rotary swaging dies around the rotating work-piece (grey)

Thanks to this processing, local uniform necking of the rod takes place, which finally leads to an overall reduction of the diameter of the whole rod. The true strain ε_{RS} imposed on the work-piece during this process can be calculated as following:

$$\varepsilon_{RS} = ln\left(A_0/A_f\right) \tag{3}$$

where A_0 and A_f represents the initial and final cross section area, respectively.

If the rotary swaging is provided below the materials recrystallization temperature, additional work hardening occurs which increases the material strength [55]. Moreover, thanks to its post C-ECAP application, CP Ti rods with nanocrystalline microstructure and unique mechanical properties can be produced [13, 56].

1.5 Residual stresses

In previous chapters, the benefits and properties of plastic deformation applied during metal forming processes were discussed. However, plastic deformation can also give rise of residual stresses in the workpiece, if inhomogeneities of the deformation appear during the process. Based on their nature, these stresses can influence either positively or negatively the brittle fracture, fatigue life, distortion, dimension stability, corrosion resistance and even yield strength of materials or engineering components [57, 58]. Therefore, understanding their origin, their measurement and analysis play an important role in the optimization of the manufacturing processes, and in the design of the engineering parts and structures.

1.5.1 Definition and classification of residual stresses

Residual stresses can be defined as self-equilibrating stresses locked-in a solid body which is free of any external load or thermal gradient. They are present almost in all solid-state materials, engineering components, however with different magnitude and length scale.

The self-equilibrating property of residual stresses can be expressed with the following equation (5):

$$0 = \int_A \sigma_n \, dA = \int_A \sigma . \vec{n}_A dA \tag{5}$$

where $\vec{n}_A$ represents the unit normal vector to the are A depicted in Fig.1.11. This equation says that residual stresses must balance across arbitrary cross section area of the body.

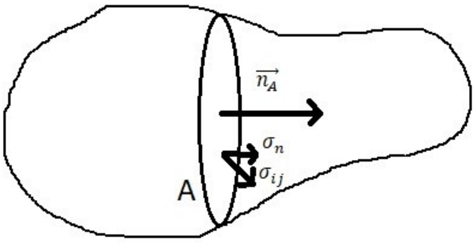

Fig. 1.11. Normal stresses σ_n averages to zero over any cross-sectional area A within a body in static equilibrium

Residual stresses can be categorized into three main groups according to length scale on which they are observed, or they self-equilibrate [59].

Type I stresses

These kinds of stresses self-equilibrate on the macroscopic scale, which is comparable to the sample size (i. e. mm to cm range). They are generated by non-uniform plastic deformation, welding or quenching of a hot sample. Since they vary continuously over macroscopic distances, often they are assigned by name *macrostresses*.

Type II stresses

Type II stresses are present on the grain size scale and they self-equilibrate on the length scale comparable to grain structure (in µm range). In a single-phase polycrystalline material, they are almost always present due to the different thermal and elastic properties of the neighboring grains with different orientation. They can be more significant in the case of multiphase materials, especially in composite materials where the elastic misfit between the strengthening phase and the matrix, and often the difference between the thermal expansion coefficients, is obviously large.

Type III stresses:

These stresses can vary on a subgrain level and self-equilibrate over distances smaller than a grain. They are caused by crystal defects, like dislocations, vacancies, interstitials, etc. which stress fields act on the atomic scale.

Type II and III stresses are sometimes treated together as *microstresses*. Each types of residual stresses are schematically depicted in Fig. 1.12.

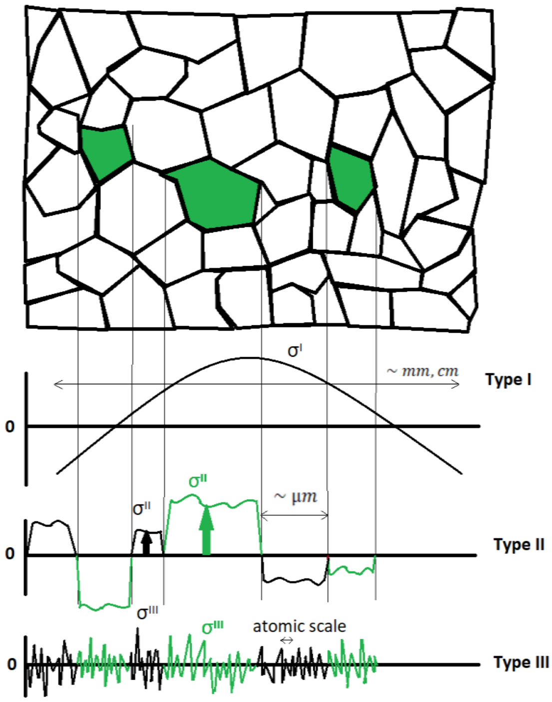

Fig. 1.12. Different types of residual stresses with their typical length scales

2 Experimental methods

2.1 Measurement and calculation of residual stresses

Measurement of residual stresses is not straightforward. Since there is no technique, which is able to directly measure the stress state of the body at a given point, other stress-related parameters are measured. Usually, this parameter is the strain ε.

Measurement techniques can be divided into three groups (non-destructive, semi destructive and destructive) depending on the extent of the destruction of the specimens during the measurement [60]. The last two methods are also known as mechanical methods [61], and include techniques as hole drilling, deep hole method, sectioning, and contour method. They are based on the measurement of the deformation produced by stress relaxing phenomena which occurs after removing a part of a material from the workpiece or after cutting to pieces the investigated sample.

The most popular non-destructive methods are Barkhausen noise method, ultrasonic method, and the diffraction methods, which include neutron diffraction (ND), high energy - synchrotron radiation and laboratory X-ray diffraction.

The Barkhausen noise method is based on a phenomenon which appears as jumps or discontinuous changes of the magnetization in a ferromagnetic sample. From the microscopical point of view, this noise is generated by the discontinuous movement of domain walls inside the sample. Its intensity is dependent on the materials microstructure and stress state. Surface residual stresses can be evaluated by this technique. Nevertheless, it is limited only to ferromagnetic materials. The principle of the ultrasonic method or refracted longitudinal wave technique is based on the acoustic-elasticity effect, i.e., the velocity of longitudinal and shear waves depends on the mechanical stress. More detailed information about the former two methods can be find in [60] and [61]. In the next chapter, the diffraction methods are discussed.

2.1.1 Residual stress measurement by diffraction methods

The basic aim of diffraction-based techniques of residual stress measurements is to determine the change of the interplanar distance d_{hkl} of a given crystallographic plane hkl in the sample.

The physical phenomenon, which stands behind these measurements is the diffraction of X-ray photons or thermal neutrons. Due to particle-wave duality neutrons can be treated also as waves. When a solid material is irradiated by X-ray photons or neutrons, the atoms composing the material interact with them and beside absorption, the atoms also scatter the radiation. Since the atoms in a crystalline material have regular spatial distribution, under special circumstances, the elastically scattered coherent waves can undergo constructive interference which in the end results in a diffraction peak of the radiation. These special conditions are given by the Bragg's equation (6) [62]:

$$2d_{hkl}\sin\theta_{hkl} = n\lambda \tag{6}$$

where λ is the wavelength of photons or thermal neutrons, n is an integer which is called as the order of the diffraction, d_{hkl} is interplanar distance or lattice spacing of a crystallographic planes with Miller indices *h, k, l* and θ_{hkl} is the Bragg angle between the incident beam and the crystallographic planes on which the diffraction occurs. It is worth to note that the wavelength λ must be comparable to the lattice spacing. In the case of monochromatic radiation, the incident and diffracted beams can be characterized by unique wave vectors $\vec{k}_i$ and $\vec{k}_f$, respectively. Since dealing with elastic scattering, the magnitudes of wave vectors are equal. The angle between the incident beam and the diffracted beam is $2\theta_{hkl}$. The difference $\vec{k}_i - \vec{k}_f$ defines the diffraction vector $\vec{q}$ which is perpendicular to the diffracting planes *hkl* and the magnitude of $\vec{q}$ equals to the reciprocal value of the interplanar distance of these *hkl* planes. The schematic representation of the diffraction is shown in Fig. 2.1.

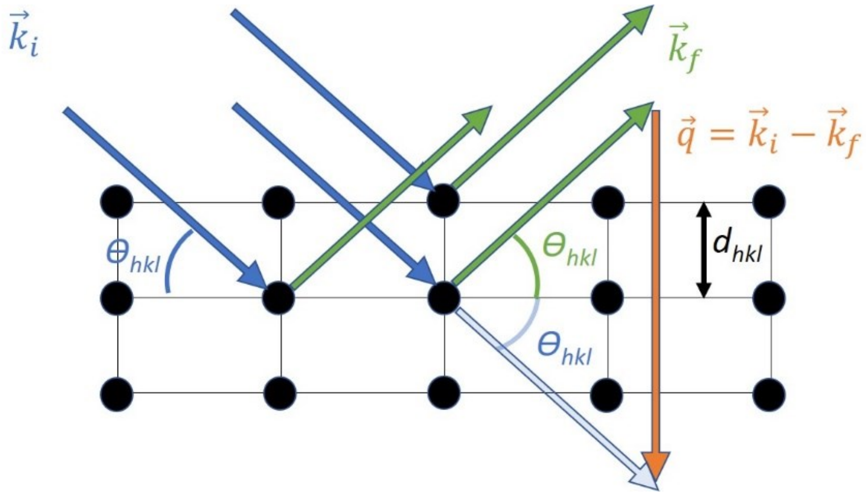

Fig. 2.1. Scheme of the vector representation of diffraction on a crystal lattice

In the presence of mechanical stress perpendicular to a *hkl* plane, the d_{hkl} is changed compared to stress free state d^0_{hkl}. From the Bragg's equation (6) comes that the Bragg angle θ_{hkl} is also deviated for a given constant wavelength. Then, by differentiating equation (6), the lattice strain ε_{hkl} can be determined as a function of shifted Bragg angle θ_{hkl}:

$$\varepsilon^{hkl} = \frac{d_{hkl} - d^0_{hkl}}{d^0_{hkl}} = \frac{\Delta d_{hkl}}{d^0_{hkl}} = -(\theta_{hkl} - \theta^0_{hkl}) \cot(\theta^0_{hkl}) \tag{7}$$

It can be seen, that beside measurement of the θ_{hkl} shifts, also the accurate stress free d^0_{hkl} or θ^0_{hkl} determination is needed for reliable lattice strain determination. This is a quite problematic task, because in polycrystalline material, an ideal stress-free state almost never exists due to the mutual interaction of the neighboring grains. According to the recommendation of VAMAS (The Versailles Project on Advanced Materials and Standards) [63], the determination of d^0_{hkl} in ND residual stress measurements can be done by the following methods:

- Measurement in the material at position/time with negligible stress
- Measurement on a representative powder sample
- Measurement on stress relaxed small coupon, cut from the examined work-piece
- Calculating d^0_{hkl} from force and moment equilibrium
- Calculating d^0_{hkl} with the assumption of zero stress perpendicular to a free surface.

The above discussed fundamental principle gives the core of both X-ray and ND measurements. The qualitative difference between X-ray diffraction and ND lies in the fact that X-ray photons interact with the electron cloud of atoms while neutrons interact with nuclei of atoms (the magnetic scattering of neutrons is not considered in this discussion). The quantitative difference can be seen on the “photon/neutron scattering power of a single atom” which is often called scattering amplitude. In the case of X-ray scattering, it is dependent on the scattering angle and increasing with increasing atomic number *Z* while in the case of coherent neutron scattering it is angular independent and varies from nucleus to nucleus or even between isotopes of the same element [64]. From the former statement comes that study of structures composed by lighter elements in the presence of heavier elements can be easier with ND. Moreover, the penetration depth of X-rays and neutrons is also not a negligible factor since there are large differences between soft and hard X-rays, and thermal neutrons from this point of view. This can be clearly seen if the attenuation lengths in Fe of the three types of radiation are compared: for laboratory X-rays, synchrotron hard X-rays and thermal neutron with energies 8.04 keV 80 keV and 25 meV, respectively, the attenuation lengths are 4 µm, 2.18 mm and 0.8 cm

[64]. Therefore, residual stress measurement provided by laboratory X-ray diffraction is limited only to subsurface. In contrast, ND and synchrotron X-ray diffraction gives information about residual stresses from a significantly larger sample volume.

2.1.2 Calculation of residual stresses from the measured strain

From continuum mechanics it is known, that generally, stress σ and strain ε are second order tensors, which can be expressed as:

$$\sigma_{ij} = \begin{pmatrix} \sigma_{11} & \sigma_{12} & \sigma_{13} \\ \sigma_{21} & \sigma_{22} & \sigma_{23} \\ \sigma_{31} & \sigma_{32} & \sigma_{33} \end{pmatrix} \text{and } \varepsilon_{ij} = \begin{pmatrix} \varepsilon_{11} & \varepsilon_{12} & \varepsilon_{13} \\ \varepsilon_{21} & \varepsilon_{22} & \varepsilon_{23} \\ \varepsilon_{31} & \varepsilon_{32} & \varepsilon_{33} \end{pmatrix} \tag{8}$$

where diagonal elements of stress tensor represent the stresses on planes normal to the direction of the axes of the coordinate system (normal stresses), the non-diagonal elements are shear stresses. In the case of ε_{ij} the diagonal elements are strains along the axes of the coordinate system and the off-diagonal elements are the shear strains between axes. They are symmetrical tensors, thus $\sigma_{ij} = \sigma_{ji}$ and $\varepsilon_{ij} = \varepsilon_{ji}$.

The fundamental relationship between stress σ and strain ε in an anisotropic material is given by the generalized Hook’s law (9):

$$\sigma = C \cdot \varepsilon \qquad \text{or} \qquad \varepsilon = S \cdot \sigma \tag{9}$$

where C and S (C_{ijkl} and S_{ijkl} in suffix notation) are elastic stiffness and elastic compliance tensors, respectively. They are fourth-rank tensors with 81 components, however only 36 are independent owing to symmetry reasons. In the case of single crystals, the number of independent components of C^{single} and S^{single} can be reduced due to symmetry groups.

In the most engineering calculations, the isotropic continuum mechanics approach is adopted which enables to express C as two independent components: the bulk Young’s modulus E and the bulk Poisson’s ratio ν. In this case, equation (9) can be written in the form:

$$\sigma_{ij} = \frac{E}{1+\nu}\varepsilon_{ij} + \frac{\nu E}{(1+\nu)(1-2\nu)}\delta_{ij}\varepsilon_{ij} \tag{10}$$

where δ_{ij} is the Kronecker delta.

In equation (10) the continuum elastic strains ε_{ij} can be replaced by the measured ε_{ij}^{hkl} with condition that E and ν are also replaced by the appropriate values, by the so-called *Diffraction Elastic Constants* (DEC) E^{hkl} and ν^{hkl}. The reason why the bulk isotropic values cannot be used is that the strain is measured on *hkl* planes of grains, which properties are obviously anisotropic. However, the single crystal values E^{hkl}_{single} and ν^{hkl}_{single} of specific *hkl* planes derived from elastic tensor components of single crystals (C^{single}_{ijkl}), also cannot be used due to the interaction between grains. The real values of DEC lie between bulk and single crystal elastic constants.

There are two ways to determine DECs. First approach is to measure them in situ during uniaxial deformation tests in elastic regime. The second approach is using theoretical models and calculate the DECs. Several models, such as Voigt, Reuss or Kröner were proposed.

The Voigt model is based on the assumption that all grains experience the same uniform strain. Then the DECs are calculated by averaging the elastic stiffness of all grains [65]. This can be considered as a relatively simple model, and basically *hkl* independent. In contrary, the Reuss model expects that all grains experience the same stress. The calculation is then done by averaging the contribution of all grains with *hkl* planes perpendicular to the applied uniaxial stress [66]. In the Kröner model (later complemented by Eshelby), the strains and stresses can vary from grain to grain, but it is assumed that the polycrystal is exposed to a specific homogeneous average stress or strain. Every grain with ellipsoidal shape is considered to be embedded in an infinite, elastically isotropic matrix. Furthermore, Kröner model assumes linear relationship between the average stress of the polycrystal and the strain of individual grains or vice versa, in the same manner as the general Hook's law. However, the single crystal elastic stiffness or compliance tensors in this case are modified by a perturbation part, which takes into account the grain interactions and grain shapes [67]. After this point, the DECs calculation follows the Reuss model's averaging step. This model gives the most realistic approximation of DECs, while Reuss and Voigt models gives upper and lower limit of these values, respectively. It is worth to mention that none of these models, in their original form, takes into the account the texture of polycrystals if it is present. This shortcoming can be overcome if the preferred orientation and shape of the grains is included at the averaging step [68].

2.1.3 Remarks on the stress/strain state of a solid body

The exact form of the stress and strain tensors in equation (8) depends on the defined coordinate system in the solid body. It can be shown that there is a special coordinate system, in which these tensors have only diagonal elements (11):

$$\sigma_{ij}^{p} = \begin{pmatrix} \sigma_{11}^{P} & 0 & 0 \\ 0 & \sigma_{22}^{P} & 0 \\ 0 & 0 & \sigma_{33}^{P} \end{pmatrix} \text{and } \varepsilon_{ij}^{p} = \begin{pmatrix} \varepsilon_{11}^{p} & 0 & 0 \\ 0 & \varepsilon_{22}^{p} & 0 \\ 0 & 0 & \varepsilon_{33}^{p} \end{pmatrix} \tag{11}$$

The axes of this special coordinate system are called *principal axes* with corresponding *principal stresses/strains*. It must be noted that sum of the diagonals is invariant, i.e., it holds in arbitrary coordinate system with nonzero off-diagonal elements of stress/strain tensors. A second note is, if the strain is not measured in principal directions but in some mutually perpendicular directions, the normal components of stress tensor σ_{ii} in the measurement directions still can be calculated by (10) since these components does not depend on shear strain components of the strain tensor.

When a solid body under load is in a static equilibrium, then the stress distribution inside the body is restricted by the following equation (12):

$$\sum_{j=1}^{3} \frac{\partial \sigma_{ij}}{\partial x_j} = 0 \text{ in suffix notation } \sigma_{ij,j} = 0 \tag{12}$$

Practically, these equations mean that if some gradient of a normal stress is measured, let’s say $\frac{\partial \sigma_{11}}{\partial x_1} \neq 0$, then $\frac{\partial \sigma_{12}}{\partial x_2} + \frac{\partial \sigma_{13}}{\partial x_3} \neq 0$ which means that gradient of shear stresses are also present. Thus, the stress tensor cannot be diagonal, the measurements were not performed in principal directions.

2.2 Neutron diffraction instrumentation

Residual stress measurements by ND can be accomplished by three principal types of neutron sources with neutron flux enough for strain measurements: nuclear reactor with continuous source, pulse reactors and spallation sources. The first case, continuous reactor source will be discussed in this chapter.

The neutron flux in uranium-fueled nuclear reactors is produced by the nuclear fission of ^{235}U isotopes. From a single nucleus fission, approximately 2.5 neutrons are generated beside gamma radiation and other fission fragments. At the core, the neutron flux can reach 10^{18} n.m^{-2}.s^{-1} with energy 1 MeV/neutron [64]. This kind of reactor (LVR-15) operates for example at Nuclear Physics Institute of the Czech Academy of Science (NPI) in Řež, Czech Republic

Neutrons with energies in MeV range are too fast to maintain the fission process and their wavelength is too short (hundreds of nano Angströms) for studies of crystalline materials. Therefore, they need to be moderated to lower energies.

During the moderation, the speed of neutrons is reduced by colliding with the atoms of the moderator medium. To increase the neutrons kinetic energy dissipation, the mass of the moderator atoms should be as close to neutrons mass as it is possible thanks to the properties of the elastic collision. Thus, the most commonly used moderator is "light water". In equilibrium with the moderator of temperature T, the neutrons velocity distribution follows the Maxwell-Boltzmann distribution. At 330 K, neutrons have energies approximately 28 meV with wavelength 1.7 Å, which is now suitable for diffraction experiments [64]. Moderated neutrons are transported out of the reactor shell by guiding tubes. The neutron beam is still polychromatic because of the spread of the peak of the Maxwell-Boltzmann distribution at T=330K. Monochromatic neutron beam is achieved by employment monochromators. There are two basic types of monochromators based on the physical principle which they use. The first one is the velocity selector where only neutrons with a certain velocity can pass through the selector and the others are absorbed. The second possibility is based on ND and Bragg's law (eq. 6). The polychromatic beam is diffracted on a large flat perfect single crystal where according to eq. 6: the fulfilled diffraction condition on some *hkl* plane selects a beam component with a certain wavelength λ which is diffracted by an angle (θ_B^M) with respect to single crystal surface. However, using flat perfect single crystals results in very low intensity of the monochromatized beam. Thus, so called *mosaic crystals* are often applied. Mosaicity means that the imperfect crystal is composed by small perfect crystal blocks rotated to each other by few tens of arcminutes. By this, the intensity can be increased however the wavelength of the diffracted beam is more spread which results in worse resolution of the wavelength. Another approach is using a bent perfect single crystal. By bending, an *effective* mosaicity is introduced into the perfect crystal [69]. This can be imagined as mosaic blocks with infinitesimal size were aligned perpendicular to the bent radius. Moreover, the bent perfect crystal serves as a beam focusing tool, in the similar manner as the focusing spherical mirrors in light optics [70]. The material used for monochromators are mostly Germanium, Silicon, or Highly Oriented Pyrolytic Graphite.

Neutron detection is based on its nuclear reaction with an absorbing nucleus. After neutron absorption, the nucleus is releasing charged particles with energies in the MeV range which can be then detected. Either a gas counter acting in the proportional mode or a scintillation detector of the produced photons can be used as the charged particles detector. ^{10}B, ^{3}He and ^{6}Li nuclei react most likely with thermal neutrons (and of course ^{235}U). The most commonly used gas in counter detectors is ^{3}He, although BF_3 is less sensitive to γ rays but its toxicity is a very limiting factor. The nuclear reaction of ^{3}He with a thermal neutron is the following [30, 64]:

$$n + {}^{3}He \rightarrow {}^{3}H + {}^{1}H + 0{,}77MeV$$

In scintillation detectors ^{6}Li-loaded glass containing a Ce activator or bound powders of ^{6}LiF mixed with ZnS doped with Ag are employed.

ND measurement in this study were carried out in NPI on horizontal channels HK4 and HK9. The layout of the whole reactor hall with horizontal channels is schematically depicted in Fig. 2.2.

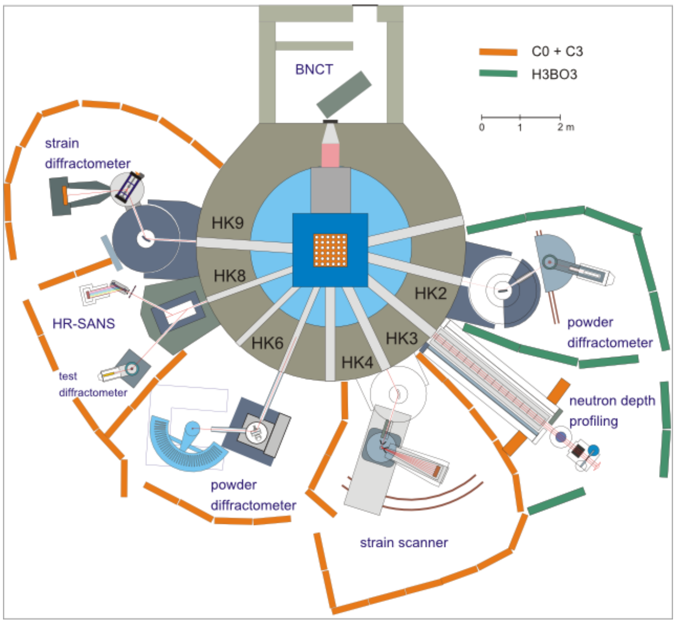

Fig. 2.2. LVR-15 reactor hall with horizontal channels layout at NPI [71]

The diffractometers at HK4 & HK9 are double axis diffractometers SPN-100 and TKNS-400, respectively, with bent Si perfect single crystal monochromators.

The take-off angle of monochromators can be varied, therefore different wavelengths can be set. SPN-100 diffractometer at HK4 can operate at wavelengths between 1 Å and 2.3 Å while TKSN-400 at HK9, between 1 Å and 3.7 Å. Both diffractometers are equipped with two-dimensional (2D) position sensitive detectors (PSD) filled with ^{3}He as neutron converter and with active area 23x23 cm^2. The complete description of the detector can be found in [72].

X-Y-Z translation stage is a standard equipment to manipulate with samples position at both diffractometers. At SPN-100, six-axis robotic arm is installed to have more flexibility of positioning of samples with complex shape. At TKSN-400, Eulerian cradle can be placed.

The unique feature of the TKSN-400 instrument is that deformation rig or furnace can be placed there, which enables to perform in situ ND experiments.

A uni-axial loading rig with maximum forces in tension/compression ±20 kN was used at the in-situ measurements during compression. The measurements could be performed only in axial setup, i.e., the diffraction vector parallel to loading axis, due to the limited space. The HK9 setup is schematically depicted in Fig. 2.3 *a* and the deformation rig can be seen in Fig. 2.3 *b*

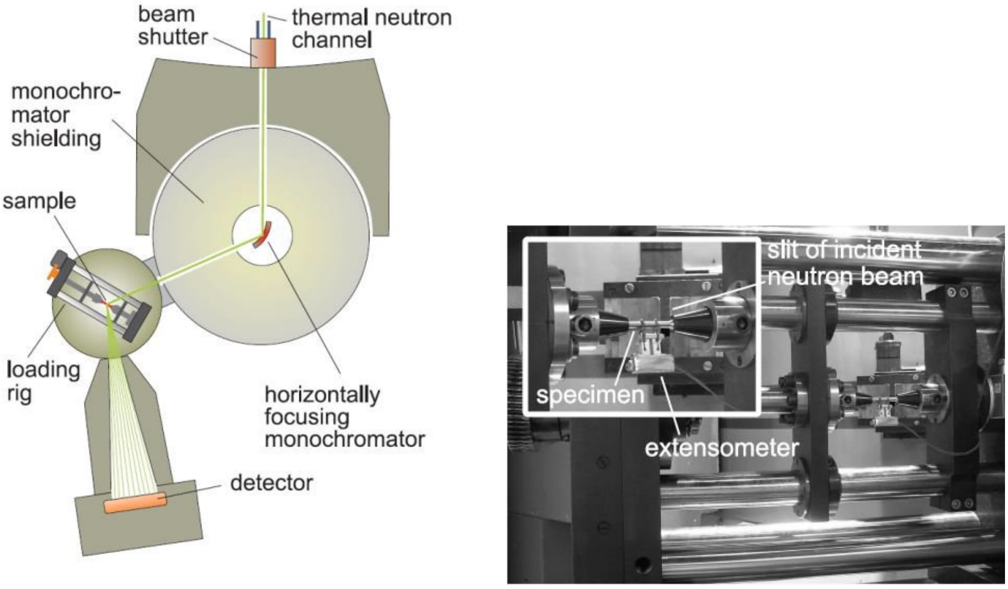

a **b**

Fig. 2.3 *a* HK9 strain diffractometer setup, *b* the deformation rig [71]

2.3 Laboratory X-ray diffraction: pole figure and dislocation density measurements

For the calculation of residual stresses from the measured strains is essential to determine also the DEC. As it was mentioned earlier (chap. 2.1.2), the texture of the material can be included in the calculation of the DEC. Moreover, if local texture measurements are performed, then the texture gradient (if present) can explain the formation or residual stress field, since it relates to deformation inhomogeneities in the sample during the plastic deformation process. Furthermore, plastic inhomogeneity in the sample can be shown by dislocation density distribution. Therefore, its measurement and determination give another approach to study inhomogeneities in microscopic scale in the sample.

The basic physical principles of X-ray diffraction were discussed in section 2.1.1. During pole figure measurement of a *hkl* plane, the incident and diffracted beam angle 2θ (given by eq. 6) and the angle between the sample surface and the incident beam, $\omega = \theta$, is set to constant. The varied parameters are the angle between the sample surface normal and the scattering plane ψ as well as the samples rotation φ around the surface normal. The configuration is schematically depicted on Fig 2.4. The measured intensity is then plotted in polar coordinates for each (ψ, φ) pair.

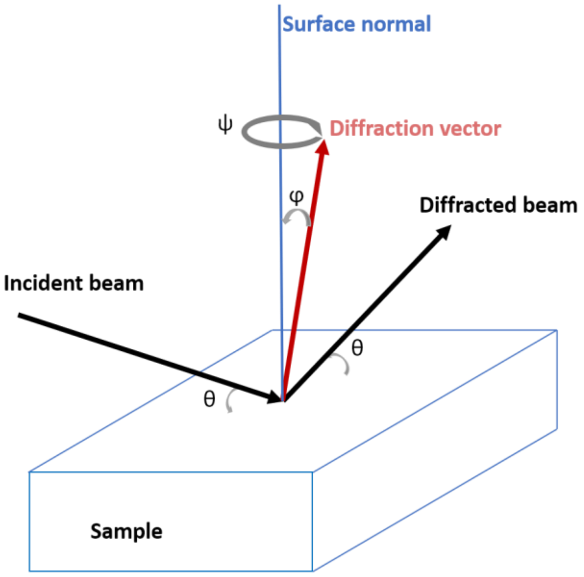

Fig. 2.4. Geometry of the pole figure measurement

Diffraction methods (neutron or X-ray) are capable to also determine the dislocation density ρ in the crystalline solid. For this purpose, the so-called *Momentum method* was used in the current study. In this technique, the 2nd and 4th order restricted moments of the measured intensity is analyzed based on their asymptotic behavior [73]. The mth order restricted moment of the intensity distribution $I(q)$ is defined as:

$$M_k(q') = \int_{-q'}^{q'} q^k I(q)dq / \int_{-\infty}^{\infty} I(q)dq \tag{7}$$

where $q = 2/\lambda\,[\sin(\theta) - \sin(\theta_0)]$, λ is the X-ray wavelength, θ and θ_0 are the diffraction and Bragg angle, respectively. Then, the asymptotic form of the 2nd order for large enough q can be written in functional form as:

$$M_2(q) = \frac{1}{\pi^2 \epsilon_F} q - \frac{L}{4\pi^2 K^2 \epsilon_F^2} + \frac{\Lambda\langle\rho\rangle \ln(q/q_0)}{2\pi^2} \tag{8}$$

ϵ_F is the average coherent domain size, K and L are the Scherrer constant and the so-called taper parameter (depending on the rate of decrease of the cross section area of the crystallites), respectively, $\langle\rho\rangle$ is the average dislocation density, and q_0 is a fitting parameter without physical meaning. Λ is a geometrical constant which includes the dislocations Burgers vector b, the X-ray diffraction vector g, the contrast factor C (for detailed explanation see [74]) and holds that $\Lambda = (\pi/2)b^2g^2C$.

The 4th order restricted moment $M_4(q)$ in asymptotic form is better to express as divided by q^2:

$$\frac{M_4(q)}{q^2} = \frac{1}{3\pi^2 \epsilon_F} q + \frac{\Lambda\langle\rho\rangle}{4\pi^2} + \frac{3\Lambda^2\langle\rho^2\rangle}{4\pi^2 q^2} ln^2(q/q_1) \tag{9}$$

where $\langle\rho^2\rangle$ is the average of the square of the dislocation density and q_1 is a fitting parameter without any physical meaning.

This method is relatively simple since it needs the measurement of only one Bragg diffraction peak. On the other hand, this measurement must be taken using high resolution equipment with negligible instrumental broadening and with small beam divergence.

2.4 Electron Microscopy: SEM, EBSD and TEM

Microstructural observation is the basic part of the characterization of the studied materials. It can provide valuable information about the grain structure and shape, local micro-texture, structure of secondary phases, etc. It can also help to determine the deformation mechanisms responsible for plastic deformation. Thus, to characterize the microstructure and determine any inhomogeneities in the microstructure, electron microscopy investigations were performed on the samples.

2.4.1 Scanning Electron Microscopy (SEM)

The main part of the microstructural observations was carried out by SEM. As a quick reminder, the basic principles of SEM will be discussed in a few words. The image in the SEM is formed by scanning the surface spot by spot of the sample by accelerated focused electron beam. These electrons interact with the electron cloud of the atoms composing the surface layer of the sample and generates various types of signals which are then detected, processed, and combined from each scanning point to form an image.

The three most important signals generated by the beam-sample interaction are the emissions of the following types:

- Secondary electrons (SE) - they are the result of the inelastic interaction of the beam with the weakly bounded electrons of the outer shell of atoms. SE are produced in the very thin layer of the sample, few tenth of nm, thus they carry information about the topography of the examined surface. Tilted surfaces with respect to the incident beam tend to emit more SE thus steep ledges are detected with higher intensity of SE.
- Back-scattered electrons (BSE) – This kind of emission is basically composed by the backscattered primary beam electrons. The backscattering process is usually accompanied by a very little energy loss of primary electrons therefore, generally the BSE signal can be detected from few tens of microns beneath the sample surface, however, it depends on the material and the accelerating voltage of the primary beam. The intensity of BSE is increasing with increasing atomic number owing to the higher probability of backscattering from larger atoms. This is called *Z-contrast* and enables to distinguish regions with different composition. The local orientation of crystallites also influences the intensity since the lattice can serve as "channels" for primary electrons. This is called *channeling contrast*.
- X-ray photons – high energy primary electrons can also cause vacancies in the inner electron shells of the atoms which is then occupied by electrons

from outer shells. During this process, X-ray photon emission occurs. The energy of X-ray photons is characteristic for every element, thus by measuring the energy spectra, analysis of the local chemical composition of the sample can be done. X-ray photon emission volume is larger than for BSE. Each characteristic volume for different signals is schematically depicted in Fig. 2.5.

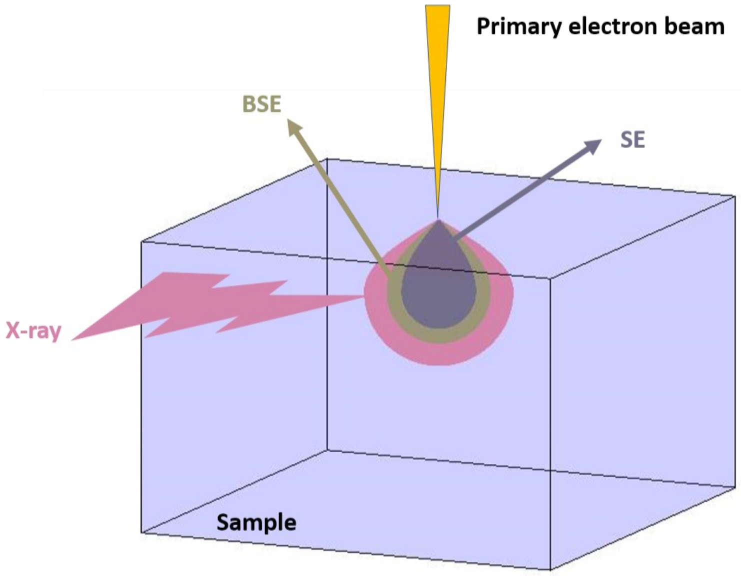

Fig. 2.5. Characteristic volumes of the emissions generated by electron beam

2.4.2 Electron back-scatter diffraction (EBSD)

The inelastically backscattered electrons of the primary beam can undergo diffraction on the local crystal lattice which results in the formation of the so-called Kikuchi patterns (Kikuchi bands) on the detector. These patterns are dependent on the orientation of the lattice thus their analysis provides valuable information of the local crystal orientation in each scanning point. Consequently, grain orientation maps can be constructed which makes the EBSD technique a highly effective tool for determination of the texture, grain-size distribution, grain boundaries, etc. of the scanned area.

SEM measurements were performed by SEM FEI Quanta^{TM} FX200 electron microscope at accelerating voltage of 15 kV. EBSD measurements were conducted with step sizes 50 nm. The working distance was 13 mm in every case. To increase the interaction volume and the contrast of the backscatter electron diffraction pattern, samples were tilted by 70° from the horizontal position towards the EBSD detector. This configuration can be seen in Fig. 2.6.

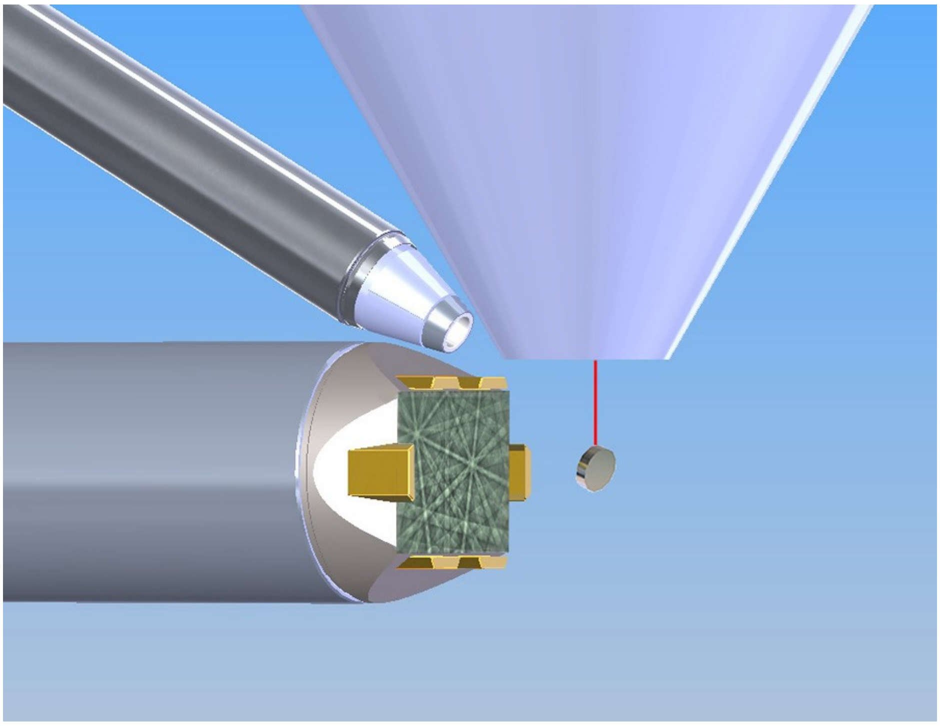

Fig. 2.6 EBSD measurement setup [75]

2.4.3 Transmission electron microscopy (TEM)

In TEM, high energy (hundreds of keV) electron beam is led through the thin foil sample and their interaction forms the TEM image. The beam is controlled by electromagnetic lenses that are placed at different positions along the beam path. TEM has two basic operation modes: imaging mode or bright field mode and diffraction mode or dark field mode (Fig. 2.7.).

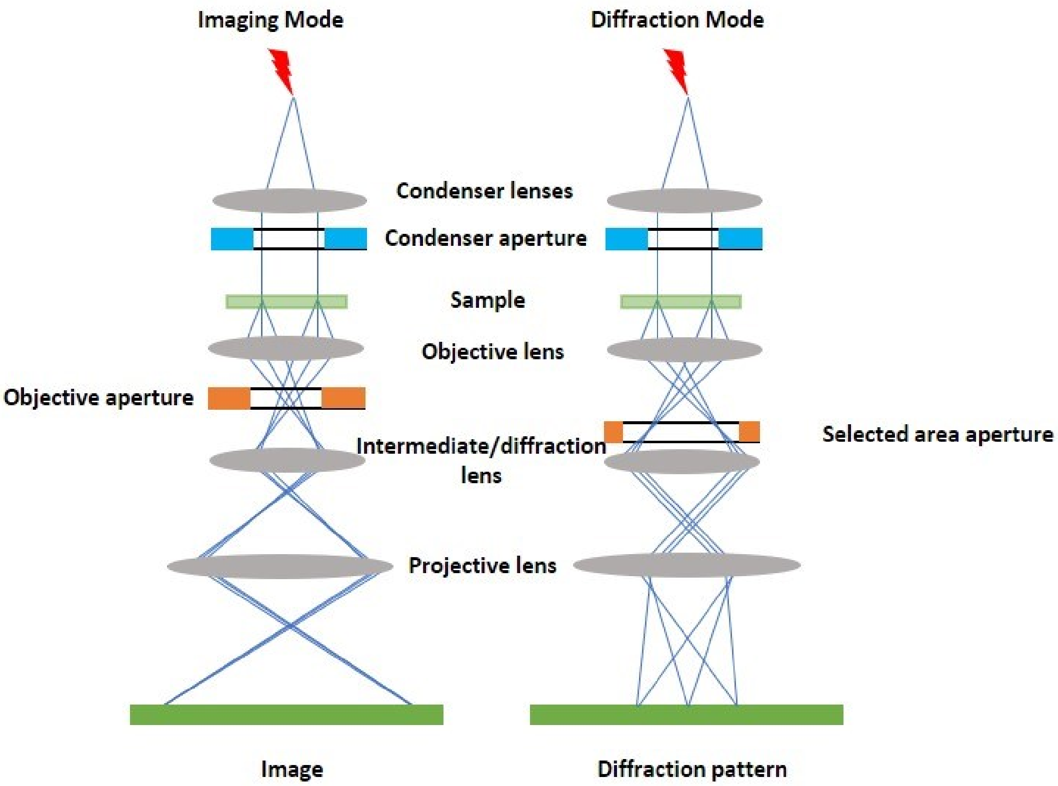

Fig.2.7 Scheme of TEM

TEM can operate also in scanning mode (STEM), where the convergent electron beam scans the defined area and the resulting signals are detected spot by spot. The image is then reconstructed from scanning points in the same manner as in standard SEM. This mode is used by the Automated Crystal Orientation Mapping in TEM (ACOM-TEM) [76] method which is a technique to map grain orientations and phases in the sample. In ACOM-TEM, electron diffraction patterns are collected by a camera spot by spot and these measured patterns are compared to the precalculated patterns of a given phase, structure, and orientation [77]. Then the best match is assigned to the measured point. By this procedure, crystal orientation map of the scanned area can be created, very similar to inverse pole figure map from EBSD measurements. This method is especially useful tool in the case when the grainsize of the material reaches tens or hundreds of nm. At this grain structure, the interaction volume of the electron beam of the conventional EBSD can be same as the grainsize, or even larger magnitude. This causes a mixture of Kikuchi bands from neighboring grains and thus it disables their unique identification.

2.5. Material conditions and experimental parameters

2.5.1 Ti grade 2 prepared by CONFORM-ECAP

Ti grade 2 samples were prepared in COMTES FHT, as. by C-ECAP technique described in chapter 1.4.1. 2 m long cylindrical rods having diameter of 10 mm were subjected up to three passes of C-ECAP on route A. The die angle at the abutment was 90°. The operation temperature was set to 220°C. However, the simulations showed that the actual temperature of the feedstock can reach 600°C at the shear zone [13,56]. After that the C-ECAP processing part of samples were further subjected to rotary swaging (chapter 1.4.2), during which the rods diameter was reduced from 10 mm to 4,5 mm.

Based on the geometry of the C-ECAP process, we defined a sample reference system (see Fig. 2.8). This designation is used throughout the text.

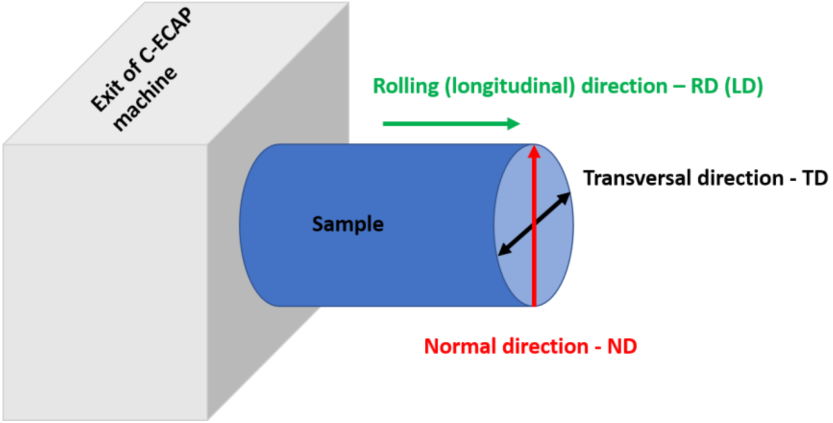

Fig. 2.8. Scheme of the sample reference system of C-ECAP treated samples

2.5.2 Ti grade 2 prepared by CONFORM-ECAP and Rotary Swaging

C-ECAP treated Ti grade 2 samples were further processed by rotary swaging at room temperature, which resulted in diameter reduction from 10 mm to 4.6 mm. The process was briefly described in chap. 1.4.2.

2.5.3 Neutron diffraction experiments

The ND residual strain scan was performed with two instruments, TKSN-400, and SPN-100.

The neutron wavelength at TSKN-400 instrument was 2.4 Å and the 2D PSD detectors were situated at $2\theta_D = 65°$. At SPN-100 the same parameters were 2.13 Å and $2\theta_D = 55°$, respectively These detector set-ups allowed to detect (0002) and $(10\bar{1}1)$ diffraction peaks. The instrument gauge volume (IGV) was set by Cd slits placed in front of and behind the sample. The IGV limits the detection of diffracted neutrons to a particular volume. Thus, scanning of various part of the samples is possible. At TKSN-400, the slit dimensions were 2 mm in width and 3 mm in height, while at SPN-100, square slits of 3 mm side lengths were used.

The cross-section of the specimen was scanned in the middle part of the C-ECAP rod[*] (Fig. 2.9). At each measurement points, three scans were done, in *axial*, *hoop* and *radial*, which refer to the mutual orientation of the diffraction vector $\vec{q}$ (thin arrows in Fig. 2.9) and the main axes of the sample.

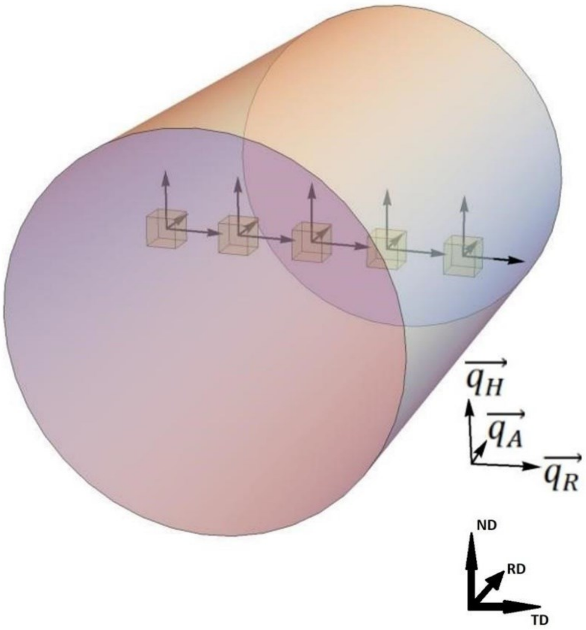

Fig. 2.9 Scheme of the line scan at HK4 with sample reference frame and the directions of diffraction vectors [54]

---

[*] We assumed that the in the longitudinal direction the gradients in the microstructure are negligible

In the case of TKSN-400, the scheme of residual strain measurement points in each direction, and the corresponding IGVs are shown in Fig. 2.10. The scanning procedure was the follows: first, a scan in transversal direction (TD) took place (5 measurements points, step-size 2 mm). In the next step, the sample was rotated by 45° and the same procedure was repeated. For the scanning of the whole sample volume, 4 rotations (0° = TD, 45°, 90°,135°) were necessary (cf. Fig. 2.10). The alignment of samples was carefully checked by laser pointers in the first place. After that, short (3 minutes data acquisition) ND scans were done near the edges of samples in order to eliminate a possible neutron beam misalignment.

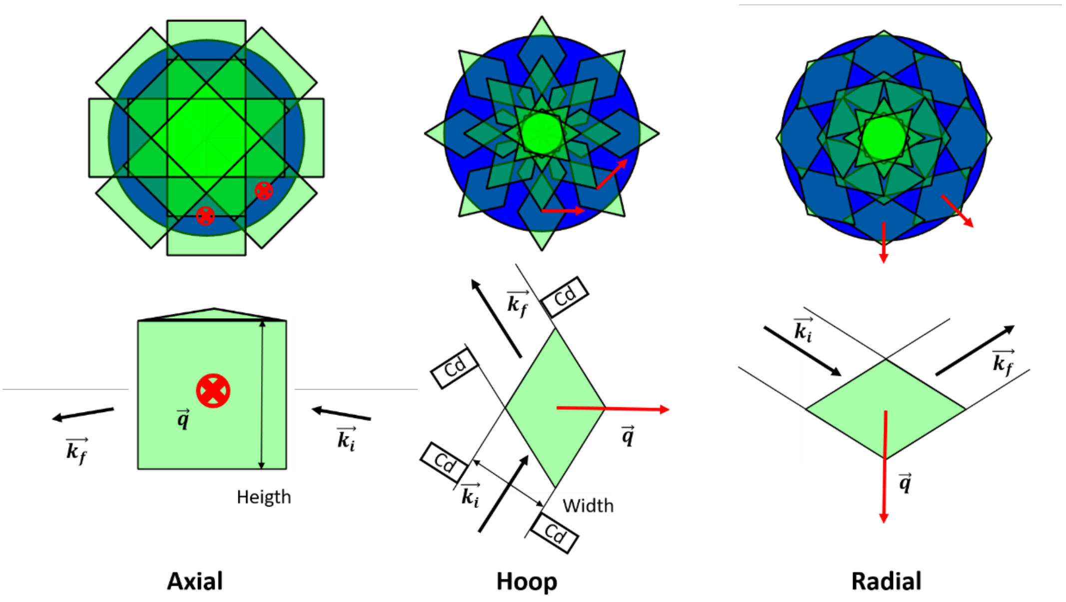

Fig. 2.10 Scheme of IGV's and their positions during the neutron diffraction scans at HK9

The scan at SPN-100 was performed only one in transversal direction, with a step-size of 1 mm.

The data acquisition time for one scan was 1h at TKSN-400 and 40 min at SPN-100, respectively. During the data processing, the data from 2D detector were converted to 1D Intensity - 2θ angle plots. The intensity profiles of the diffraction peaks were fitted by a Gaussian function.

In-situ ND experiments were carried on during compression of RS samples. An uniaxial loading rig with a 20 kN load cell was used for compression tests. The measurements could be performed only in axial setup, i.e., the diffraction vector parallel to the loading axis, owing to the limited space. The experimental setup is schematically depicted in Fig. 2.3 *a* and the deformation rig can be seen in Fig. 2.3 *b.*

1 mm wide slits were used without vertical limitation. The deformation rate was 10^{-3} s^{-1} - at every sample. The deformation was measured with extensometer placed on the sample. The deformation was stopped, and the ND measurements were done at 0.2, 0.5, 1, 1.5, 2, 2.5, 3, 5, 8, 12, 16, 20, 25 % applied strains (or until fracture). The data acquisition time in each measurement point was 1 h. The initial state was scanned for 2 h.

2.5.4 X-ray measurements

X-ray texture measurements were done on PANalytical XPert MRD diffractometer using CuKα radiation with polycapillar optics in the primary beam was employed for acquiring the (0002), $(10\bar{1}0)$, $(10\bar{1}1)$, $(10\bar{1}3)$ and $(11\bar{2}2)$ pole figures. (ψ, φ) pairs were measured by 5° step in ranges $\psi \in (0°, 75°)$ and $\varphi \in (0°, 360°)$. Measurement results were further processed by MTEX 5.3 free and open-source software toolbox for MATLAB in order to determine the orientation distribution function (ODF) and subsequently complete the pole figure to the whole $\psi \in (0°, 90°)$ range.

In the X-ray dislocation density measurements, a rotating-anode Cu double-crystal diffractometer with 1,5405 Å wavelength was used. The diffraction from $(10\bar{1}1)$ planes with $2\theta_0 = 40{,}170°$ was detected by 1D DECTRIS 1K detector with pixel size of 0,05 mm. The measured profiles were analyzed then by *m_v08.11.2014* software.

2.5.5 SEM & EBSD measurements and sample preparation

For microstructure investigation by SEM and EBSD technique, the samples were first grinded on SiC papers from P500 to P4000. This was followed by electrochemical polishing in LectroPol-5 with voltage of 45 V for 70 s, in the solution of 300 mL CH3OH + 175 mL 2-butanol + 30 mL HClO4 at −20 °C.

Different parts of the same sample were investigated by SEM or EBSD. C-ECAP-ed Ti grade 2 cylindrical samples were investigated in four different areas within the same specimen. Their arrangement can be seen in Fig. 2.11. They are at upper, lower and a side-long periphery, and in the center. Each surface was perpendicular to TD.

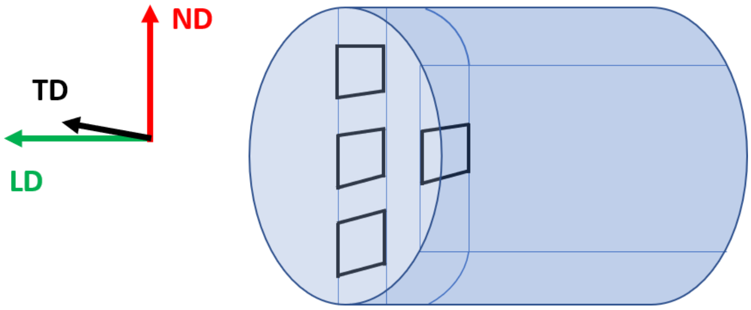

Fig. 2.11. – Scheme of areas of interest investigated by SEM and EBSD for Ti Grade 2 samples

EBSD measurements were analyzed by TSL OIM software and by M-TEX toolbox (version 5.5) of MATLAB (version R2020.a) software package. Only points with confidence index (CI) higher than 0.1 were accounted for the analysis Half quadric filter denoising procedure was used for de-noising in the IPF maps [78].

2.5.6 Microhardness measurements

Microhardness measurements were conducted on the polished surfaces in cross section on a Q10 microhardness device. The indentation force was 50 N and the indentation time 10 s. The step size between indents was 0.6 mm. Measurements were done in the circular cross section of samples. The investigation covered circular surface with radius 3.6 mm, i.e., the very near edges of samples were not examined.

2.5.7 TEM and sample preparation

A JEOL 2200 FS TEM microscope with accelerating voltage of 200 kV was used in this study for ACOM TEM investigation of the RS samples. Thin foil samples with a diameter of 3 mm were prepared in two steps. First, they were mechanically grinded down to 150 µm thickness, then electrochemically thinned in a

Tenupol 5 device using a solution of 300 mL CH3OH + 175 mL 2-butanol + 30 mL HClO4 at −20 °C and a voltage of 40 V until a hole appeared.

3. Aims of the thesis

The main goal of the present thesis is to investigate SPD Ti by ex-situ and in-situ neutron diffraction and by several complementary methods in order to elucidate the residual stress state of the bulk and its microstructural background. Residual stresses can influence the lifetime of the work-piece, thus their study can play a key role in planning of further material processing steps.

The dominant deformation mechanism during straining of the material determines the deformation behavior of the bulk. The in-situ neutron diffraction technique enables to investigate the materials during deformation tests, which provides valuable information about the internal stresses and deformation mechanisms. Therefore, by application this method, the study of the deformation mechanism of the materials after the final processing step is also the part of the thesis's goal.

Partial goals of the present work can be summarized in the following points separated by studied materials:

- Commercial Ti grade 2 processed by CONFORM-ECAP method
    - To investigate the residual stress state and its spatial distribution in the bulk samples with respect to the different levels of processing
    - To characterize the gradient of the microstructure and texture of samples after corresponding passes of the CONFORM-ECAP
- Commercial Ti grade 2 prepared by CONFORM-ECAP and Rotary Swaging
    - To characterize the microstructure of the processed material
    - To investigate the evolution of the internal stresses and deformation mechanisms in compression

4 Experimental results and discussion

4.1 Initial state

The microstructure of the initial state, this is before the C-ECAP processing, was investigated by EBSD (Fig 4.1). Two areas were examined perpendicular to the axial direction of the sample: near to the periphery and in the center.

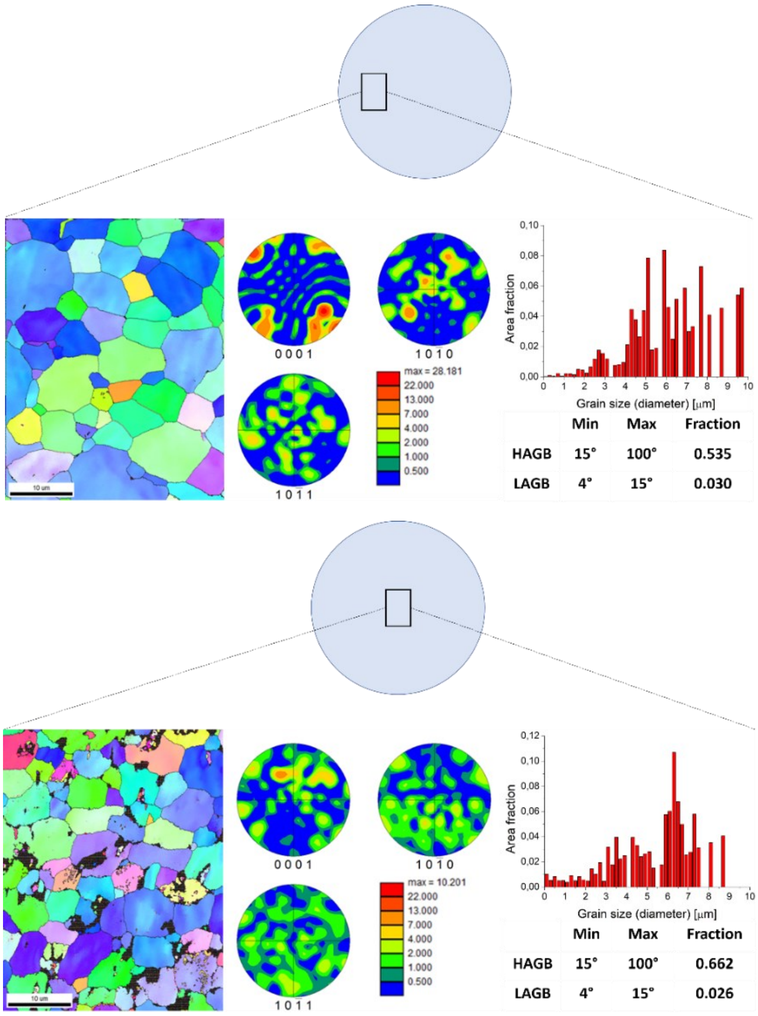

Fig.4.1. Microstructure of initial state of Ti grade 2 sample

The microstructure mainly consists of equiaxed grains with high angle grain boundaries (HAGB). The mean grainsize is around 5-6 µm at both areas. The only difference between the center and periphery is in the micro-texture. At the periphery, fiber texture is present, where (0001) basal planes are aligned with the axial direction. At the center, there is no preferred orientation of grains, the micro-texture is rather random.

The distribution of the $(10\bar{1}1)$ peak position shifts with respect to the $2\theta_{10\bar{1}1}$ value measured in the center of the sample is shown in Fig 4.2. The error of the measurement was approx. 1%.

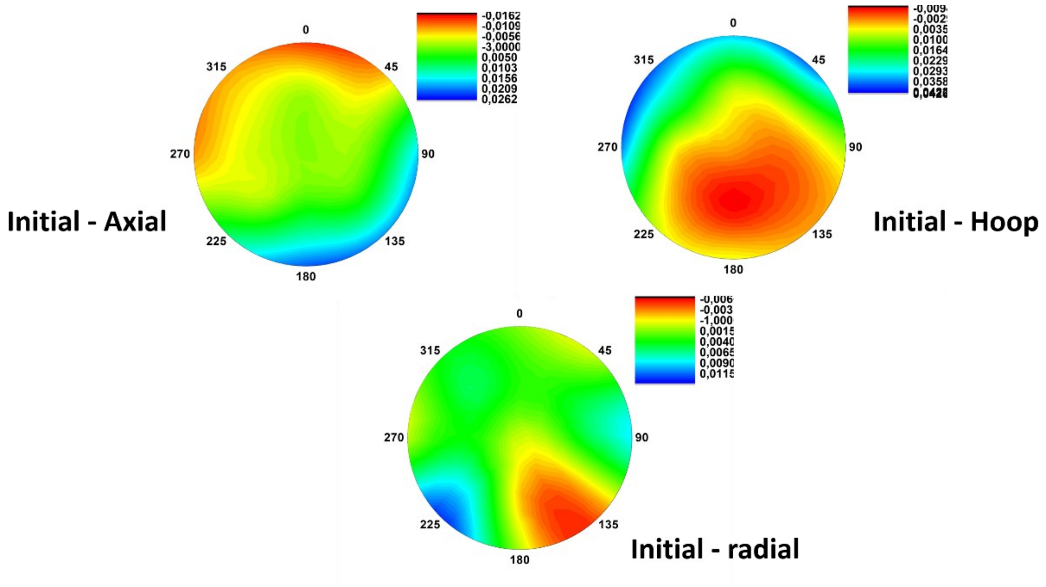

Fig. 4.2 The distribution of the $(10\bar{1}1)$ peak position shifts $\Delta\theta$ with respect to the $2\theta_{10\bar{1}1}$ value measured in the center of the sample for axial, radial and hoop direction in three mutually perpendicular directions of the diffraction vector

It is worth noting that these peak shifts are partially include artifacts, given by the shape of IGV. As it is obvious from Fig. 2.10, during the measurement at the edges in axial and hoop directions a relatively large portion the IGV is larger than the corresponding sample volume (see also Fig.4.3). This results in anomalous peak shifts, which are not related to the stress states in the sample. Therefore, we defined the so-called Sample Gauge Volume (SGV) – see red bordered are in Fig. 4.3 - in order to correct this issue. It can be assumed that the center of gravity of the diffraction peak is directly related to the center of gravity of SGV's [64]. As it can be seen in Fig.4.3 such a correction leads to shifting of diffraction peak positions to higher or lower 2θ angles, depending on the ratio of SGV/IGV and their mutual position.

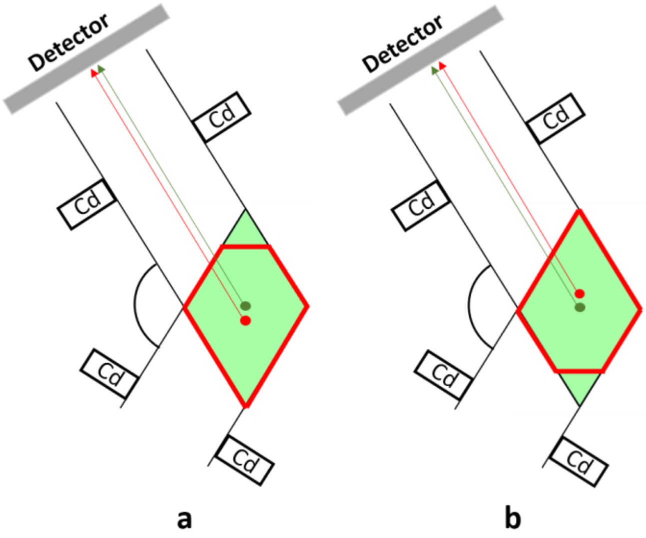

Fig. 4.3. Schematic representation of peak shift due to the partially filled gauge volume

There are several ways for the calculation of the correct 2θ positions. One approach simulates the paths of neutrons using Monte-Carlo algorithm [79]. Another way is to analytically calculate the peak shifts. [80]. The latter approach is assuming sample symmetry originating in its deformation history. Since in our samples there is an axial symmetry caused by extrusion, we can assume that the correct peak positions can be calculated as the average 2θ values of the opposite measurement points at the periphery (R=4mm, 0°-180°, 45°-225°, etc.). The corrected $(10\bar{1}1)$ peak position shifts distributions for the three directions are shown in Fig. 4.4. It is obvious that in axial and radial directions the peak shifts are small, whereas in Hoop-direction significant gradients are present. Since the peak shifts are linearly related to the lattice strains (chap. 2.1.2. eq. 7) it may be expected that the largest residual strain gradient is present in the hoop direction.

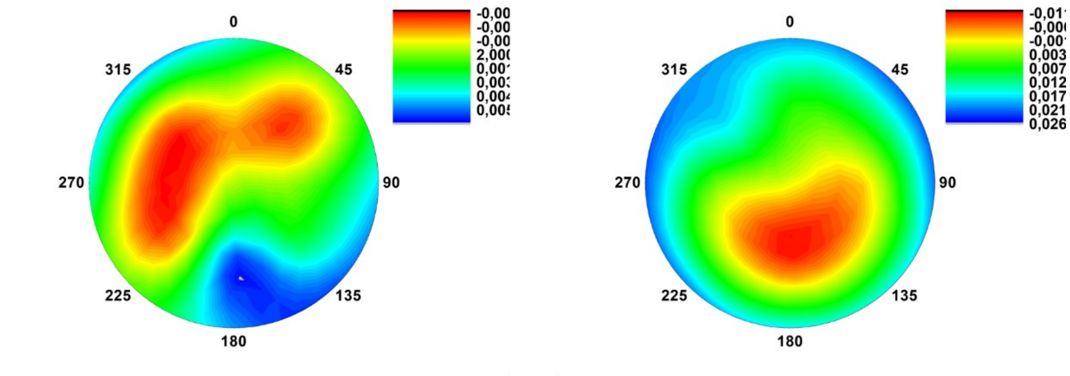

Initial-axial corrected **Initial-hoop corrected**

Fig.4.4 The Corrected distribution of the $(10\bar{1}1)$ peak position shifts $\Delta\Theta$ with respect to the $2\theta_{10\bar{1}1}$ value measured in the center of the sample for axial and Hoop direction for initial Ti grade 2 sample.

4.2 Ti grade 2 CONFORM-ECAP treated

In the next chapter the following sample notation will be used: C1 - one C-ECAP pass, C2 - two passes, and C3 - three passes.

4.2.1 Microstructure

C1 microstructure

The inverse pole figure (IPF) maps for C1 sample in different areas are presented in Fig. 4.5. The microstructure is bimodal. It contains large, elongated grains as well as small, equiaxed grains. The latter has formed by dynamic recrystallization during the extrusion process. However, the large grains are also severe deformed – see the low angle grain boundaries (LAGB), represented by yellow line in the insert of Fig. 4.5.

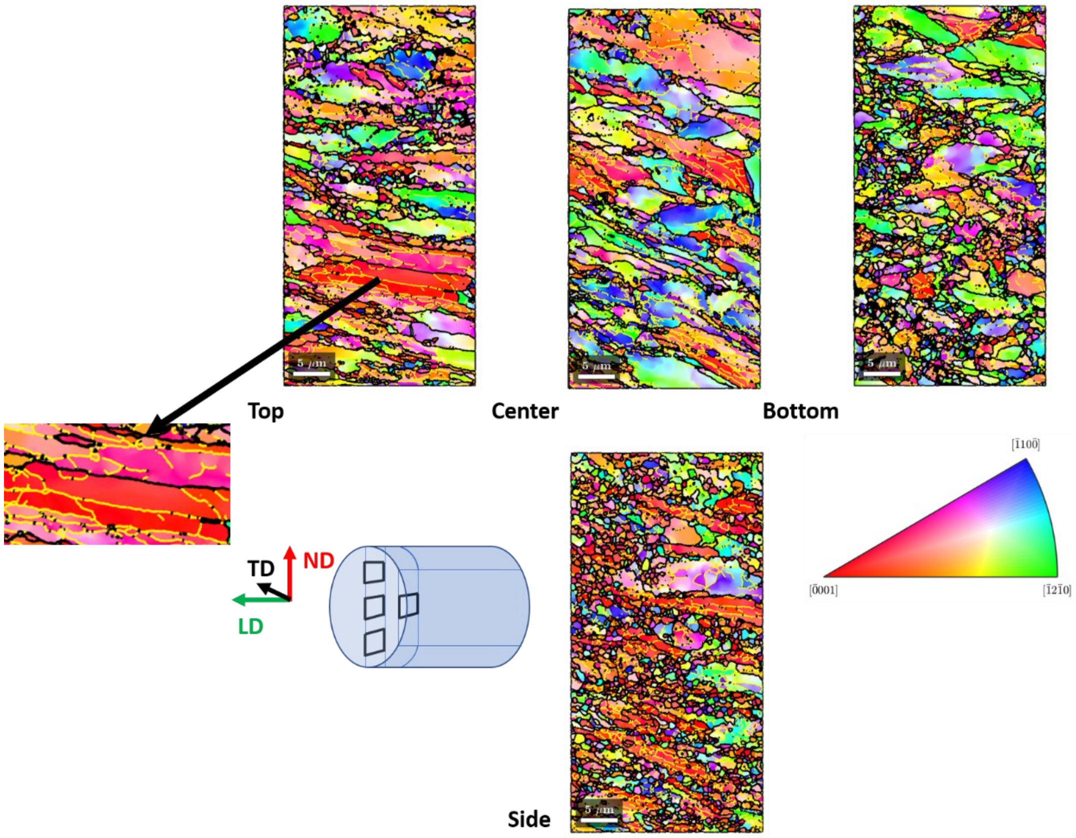

Fig. 4.5 IPF map on four different surfaces (indicated bottom left), perpendicular to TD, in the C1 sample, with IPF color key orientation triangle

It is noteworthy that the fraction of fine grains is higher at the bottom and side part than that at the center and top part of the sample. Fig. The average grain sizes (diameter) are between 1 and 2 μm. Owing to the bimodal distributions of the microstructure, we also calculated the areas of the grains. Their distribution is shown in Fig. 4.6.

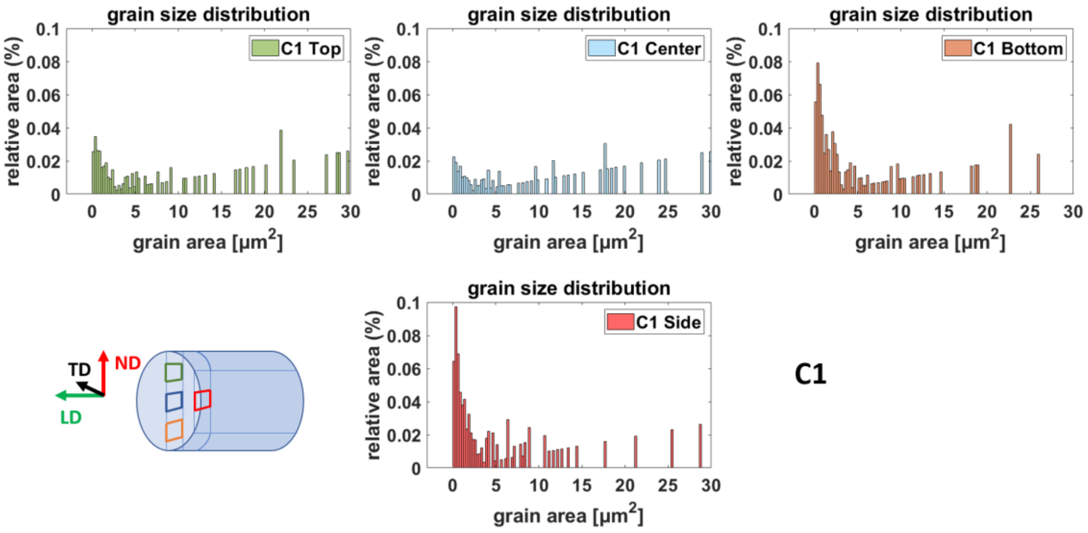

Fig. 4.6 Grain size (area) distribution in the four investigated areas of the C1 sample

Since the fraction of the elongated grains is relatively large, it is worth to characterize them in more detail. In the first step we approached the shape of all grains by ellipses, based on the fitting procedure described in Ref. [81].

In Fig. 4.7 the aspect ratios of the fitted ellipses (ratio of the major and minor axes) in the particular areas are presented.

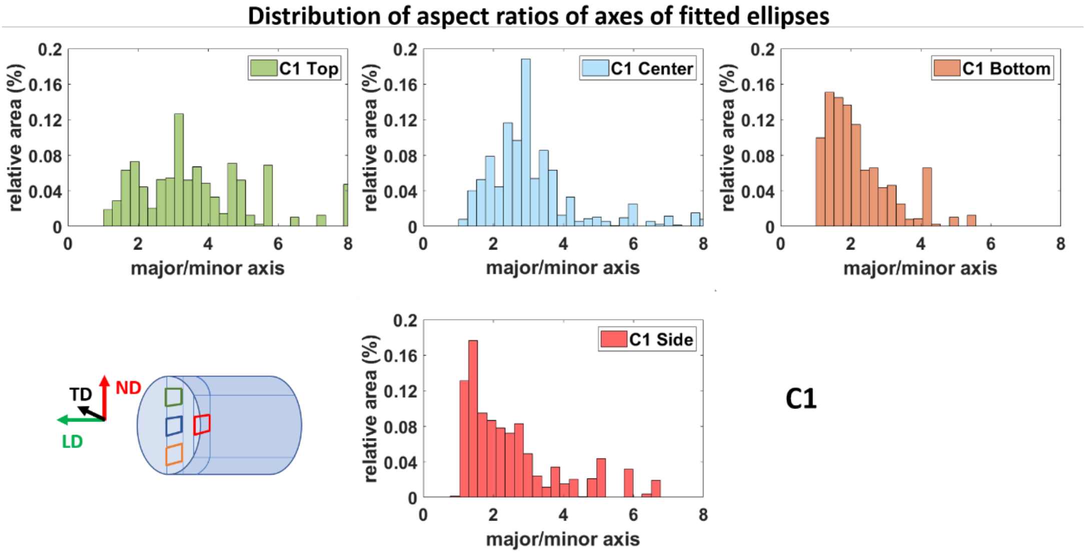

Fig.4.7. Distribution of aspect ratios of longer and shorter axes of grains in the four investigated areas of the C1 sample

From top to bottom, the aspect ratios are getting lower, which means that grains are becoming more and more equiaxed. At the side part, the almost equiaxed grains gives the largest fraction.

Another interesting geometric aspect, connected to elongated grains, can be noticed in Fig. 4.8., where the distribution of angle orientation of major axes with respect to longitudinal direction is shown. The major axes tend rotate towards the same direction. This can be associated with material flow during the ECAP process [82]. This analysis contains only grains with area larger than 4 μm^2 and angles are measured counterclockwise from horizontal direction.

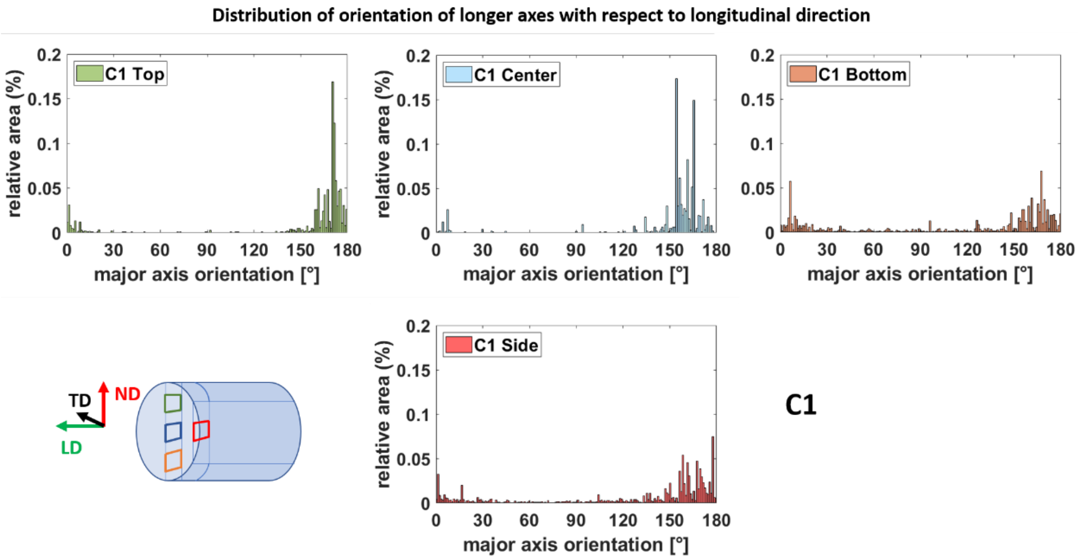

Fig. 4.8 Orientation of major axis of elliptic grains in the four investigated areas of the C1 sample

It can be seen that in upper part of the sample, elongated grains tend to be oriented in longitudinal direction, while in the other parts, a larger fraction is tilted towards to normal direction.

The microstructure after the first pass is heterogeneous. In the bottom part the fraction of the fine grains is higher than that on the top, which indicates that neither the strain nor the temperature is evenly distributed during the C-ECAP process. This assumption has been proved by finite element simulation of Mertová et. al [56]. They have found that there is a significant temperature and deformation gradient in the sample during the C-ECAP process ([56], figure 2). The has shown that the bottom part of the sample undergoes higher deformation at higher temperature. Consequently, at the bottom the dynamic recrystallization is significantly enhanced.

C2 microstructure

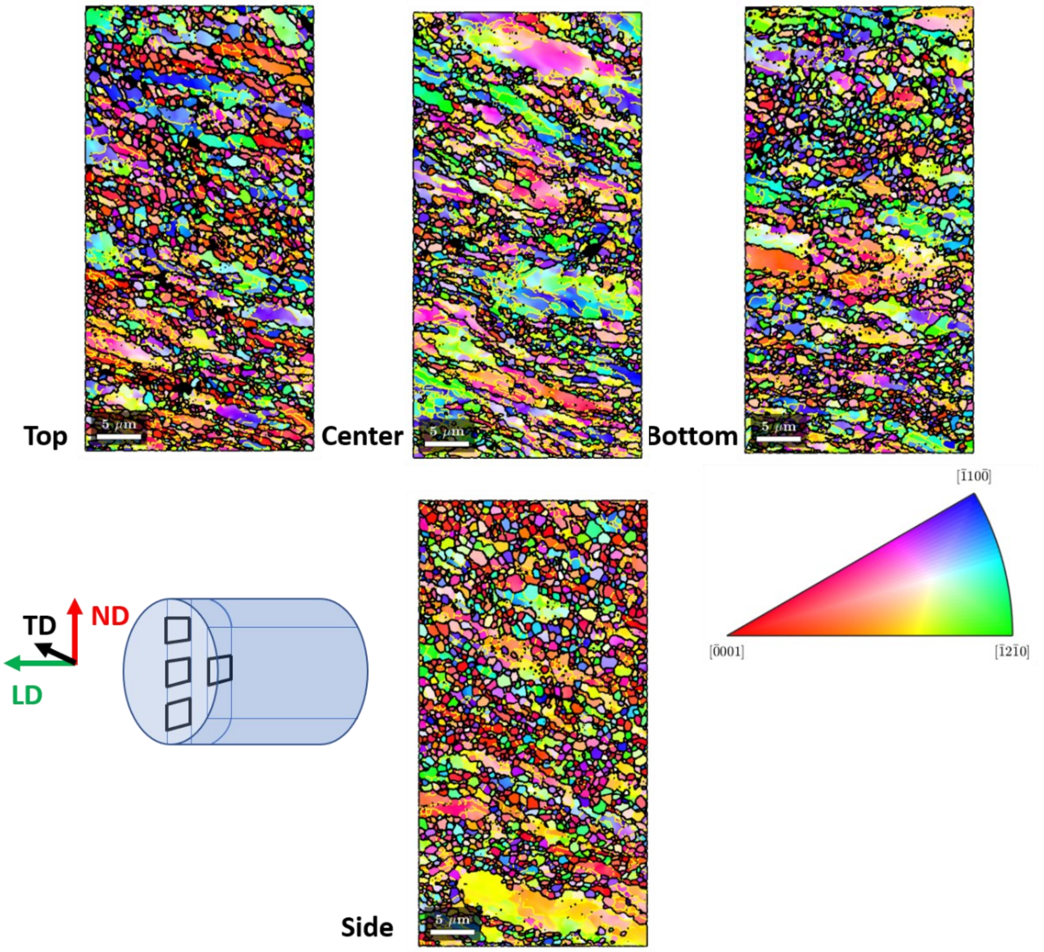

Fig.4.9 IPF map on four different surfaces (indicated bottom left), perpendicular to TD, in the C2 sample, with IPF color key orientation triangle

The microstructure of C2 sample is presented in Fig.4.9. It can be seen that the large grains are still present. However, their fraction is smaller than after first pass. Concurrently, the overall fraction of fine grains increased in every area, (Fig.4.10). The center position has the smallest fraction of fine grains with 0,15 %. However, this value is still four times higher than that for the C1 sample. It The gradient in fine grain fraction is also significantly reduced. The highest difference between fine grain fractions in different areas is 0,06 % in C2, whereas it is 0.12% in C1 sample.

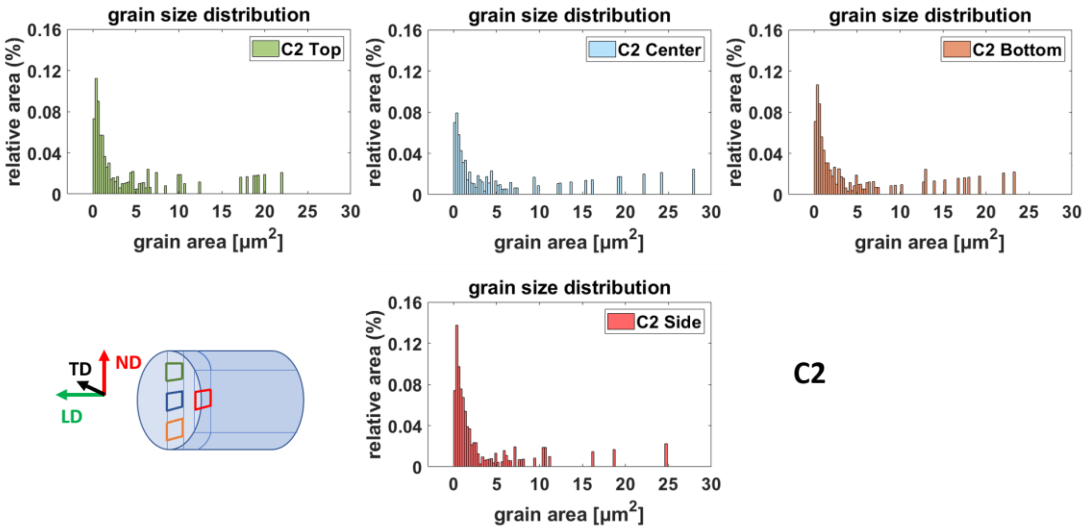

Fig.4.10 Grain area distribution in the four investigated areas, in the C2 sample

This change can be ascribed to the application of route A (chap. 1.4.1). During the second pass the sample's bottom part became its upper and vice versa. Consequently, the small grains will be distributed more evenly throughout the microstructure.

It is worth to mention that from the point of view of homogeneity of upper and lower part, the shortcomings of the previous orientation are not fully overcome by changing the sample orientation. This can be seen in Fig. 4.11. where the distribution of aspect ratios of longer and shorter axes of fitted ellipses to grains are depicted, with respect to the position. In down part of the sample, higher fraction of ratios near to 3 remained from the previous C-ECAP pass, beside the increased fraction with ratios between 1 and 2. On the other hand, the positive effect of sample orientation change can be noticed also in center position, where the fraction of higher ration than 2 is decreased almost by factor 2 with respect to previous C-ECAP pass. In the side part apparently, there is no changes change.

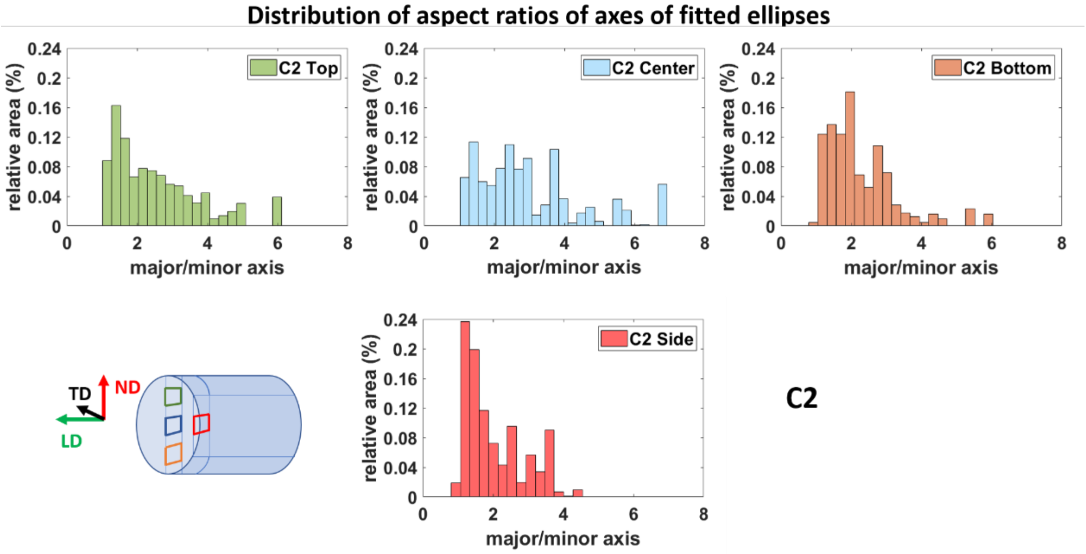

Fig.4.11 Distribution of the aspect ratios of grains in the four investigated areas of the C2 sample

The distribution of orientation of the major axes of larger grains, indicates that in upper and center part of the sample, the grains are further rotated towards the normal direction-to 150° (Fig.4.12). However, in the bottom and side part the maximum of the distribution is around 160°.

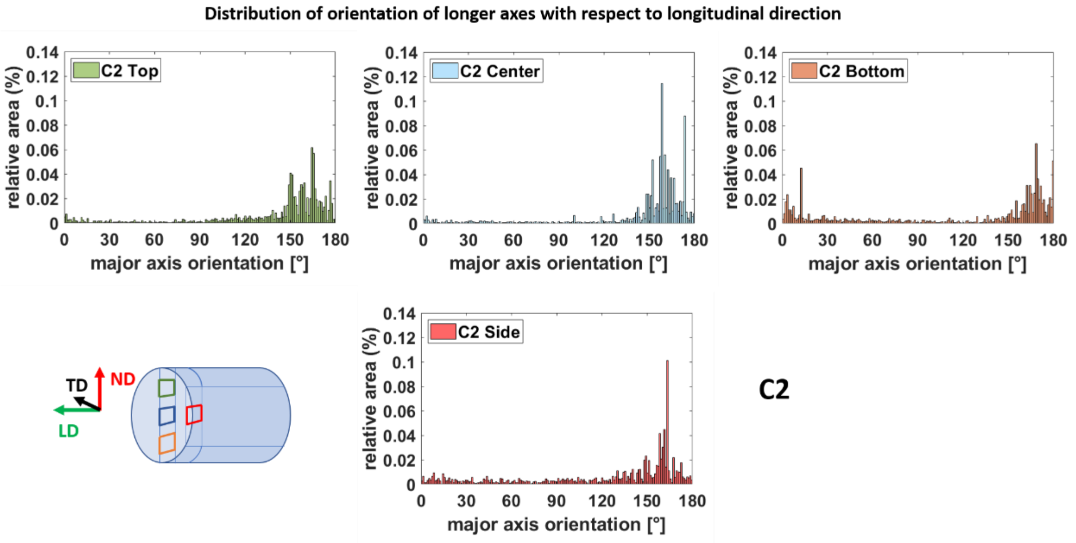

Fig.4.12 Orientation distribution of longer axes of larger grains with respect to LD, in the four investigated areas of the C2 sample

In overall, the second pass brings more homogeneity into microstructure by removing some of the gradients present after the first pass. The grain structure is becoming more uniform, with higher fraction of equiaxed fine grains.

C3 microstructure

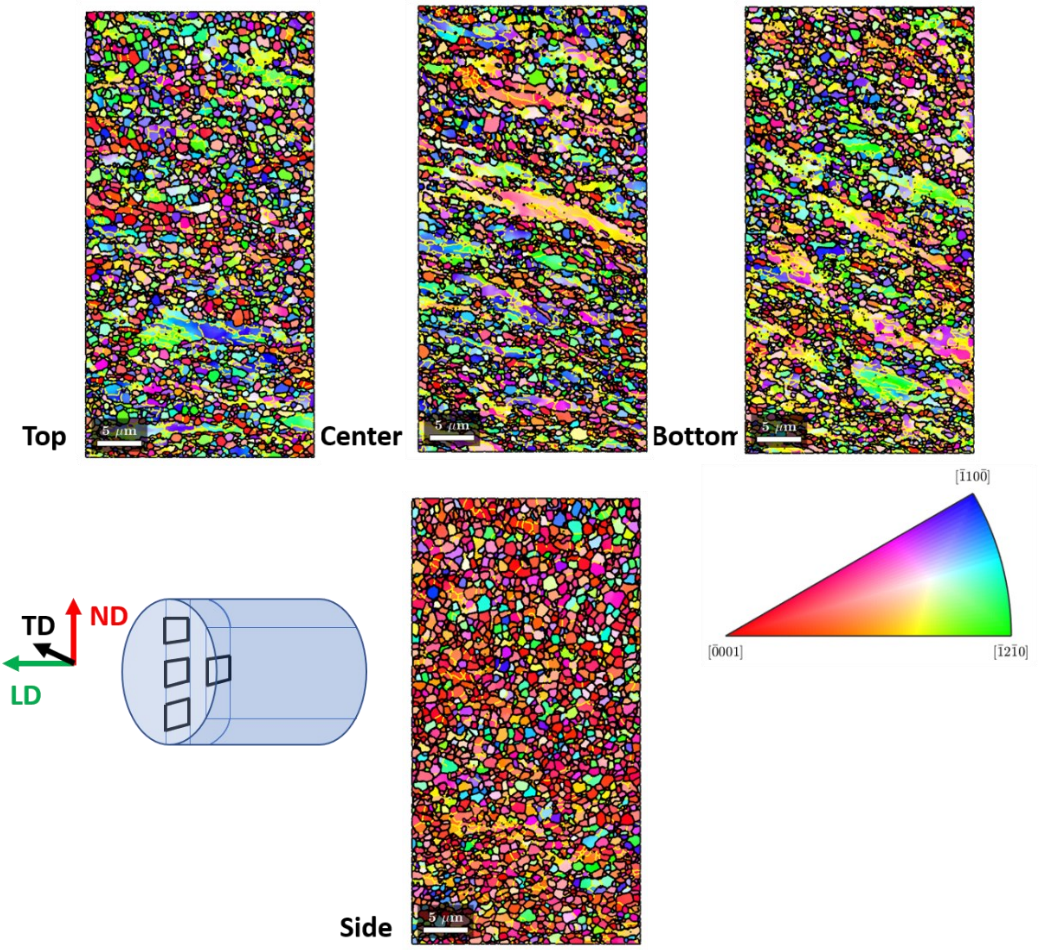

Fig.4.13 IPF map in four different areas (indicated bottom left), perpendicular to TD, in the C3 sample, with IPF color key orientation triangle

The microstructure of Ti grade 2 sample after the third pass is shown in Fig.4.13. It can be seen on the first sight that the grain structure became more homogeneous. Especially at the side part, with larger, elongated grains are not present. Significant area reduction of large grains takes place in the top part as well. This is quantitatively depicted in Fig.4.14. Grains larger than 10 µm^2 have practically disappeared from the grain size distribution in the two above mentioned regions.

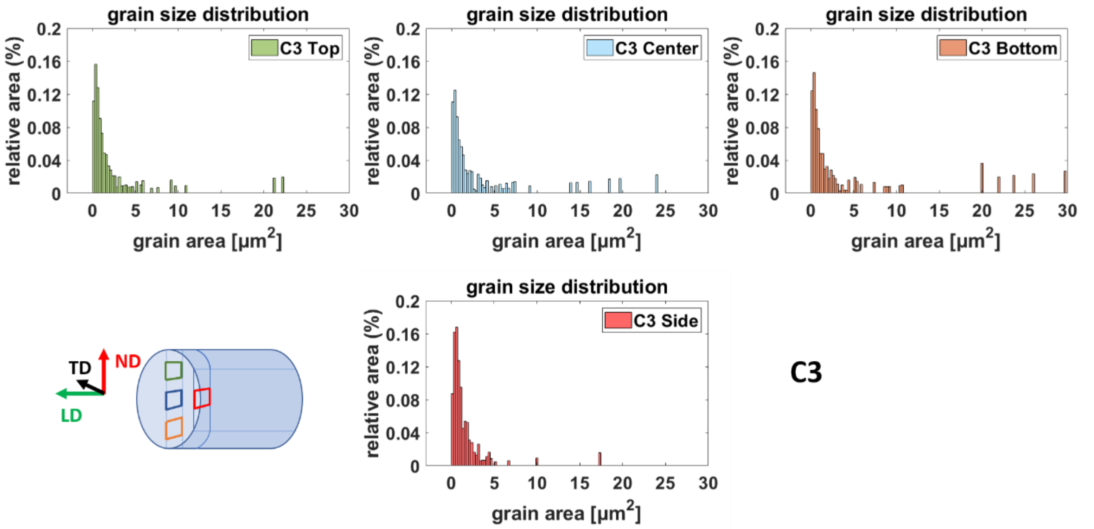

Fig.4.14 Grain size (area) distribution in the four investigated areas, in the C3 sample

The fine grain fraction is above 0,20 % everywhere, while in C2 sample, only the side part exceeds this threshold. It can be noticed that the lowest fraction of fine grains is still located in the center of the sample. An interesting point can be observed in the for the side area. The maximum of the grain area distribution is shifted towards the highest values, which indicates a moderate grain growth.

The homogenization process can be noticed also in the Fig.4.15, where the distribution of the aspect ratios is plotted. In all examined areas the maximum of distribution is near to value 1.

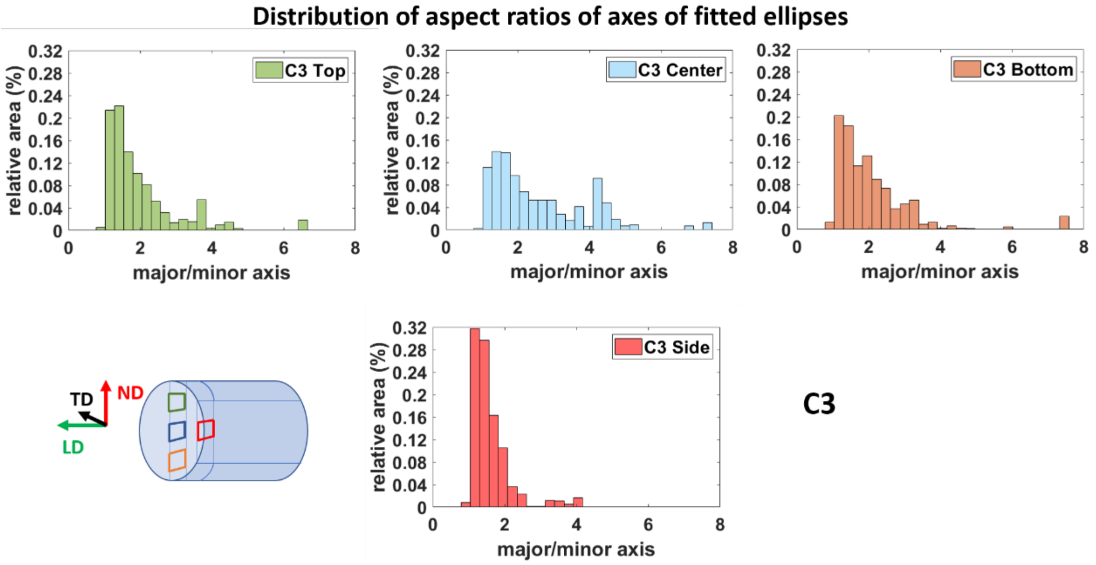

Fig.4.15 Distribution of aspect ratios of longer and shorter axes of grains in the four investigated areas of the C3 sample

The repetitive application of C-ECAP method showed the positive effect on the grain refinement., Similar conclusions were drawn by many authors [83, 84, 85, 86]. However, the majority of investigations was and is focused only to the center area of the processed billets and the overall degree of homogeneity remained unanswered. This problem was investigated in aluminum alloys by Xu et. al [87] processed by conventional ECAP and by Procházka et al. [88] on C-ECAP. Xu's investigation showed that the highest scatter in the microhardness is present after the first ECAP pass, and the lowest hardness values are at the bottom area. Procházka's group studied two areas: bottom part and central part. They showed that in bottom part, the grain size is smaller compared to central part. Furthermore, the fraction of elongated grains was higher at the central part after one C-ECAP pass. Our findings on Ti grade 2 correspond with his results.

Based on the EBSD investigation result, several conclusions can be drawn:

- Large gradient in grain size distribution is present after the first C-ECAP pass, where the finer grains are at side part while significant number of coarse grains is present in center region.
- After the second C-ECAP pass, the gradient between the peripheral regions is reduced but in the center region, coarse grains are still present.
- After the third C-ECAP pass the microstructure homogenization continued. Furthermore, a slight grain growth occurred at side regions

4.2.2 Crystallographic texture

Local textures are presented by the means of Pole Figures (PF) of (0002), $(10\bar{1}0)$ and $(10\bar{1}1)$ crystallographic planes. The spherical projections are equal area projections. The angle φ - altitude is measured from the center of PF, and ψ - azimuth is measured from "east" direction (chap. 2.3) counterclockwise. PF from EBSD measurements were rotated by 90° clockwise around ND to match their orientation to PF from X – ray measurements.

The projection of the sample reference frame from TD and LD view on the PFs, supplemented with the theoretical shear plane (SP) and its normal (SPN) is shown in Fig. 4.16. Since the inner angle in the C-ECAP setup was 90°, the SP and SPN is theoretically inclined by 45° from ND (LD).

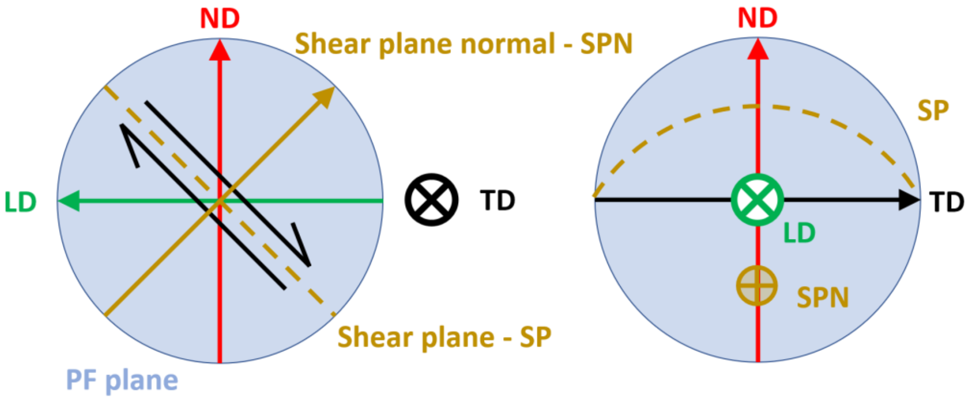

Fig. 4.16 Projection of ECAP treated sample reference frame on pole figure together with shear geometry. LD-longitudinal direction, ND-normal direction, TD-transverse direction, SP-shear plane, SPN-shear plane normal

C1 local EBSD & X-ray texture

The local EBSD-textures of the investigated positions in C1 sample are depicted in Fig. 4.17. From Fig. 4.18 a. it is obvious that the basal poles tend to align between the theoretical SPN and the ND. From the spread of basal poles maxima in Fig. 4.17 b. it can be concluded that, at top and side positions, more pronounced rotation of basal planes around an axis occurs. The direction of this axis is near to the location of the maxima of prismatic PF.

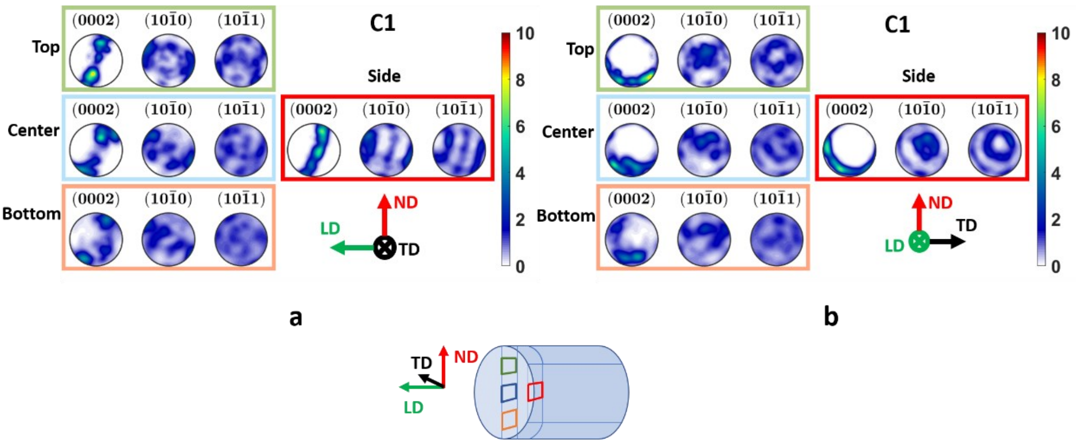

Fig. 4.17 Local EBSD-texture distribution by means of PF, measured by EBSD in C1 sample in *a*-TD and *b*-LD view

Local X-ray-textures in the mean of PF are depicted in Fig. 4. 18. The measured positions in the sample are depicted in the left bottom corner. In contrary to EBSD experiments, both side parts were examined in this case.

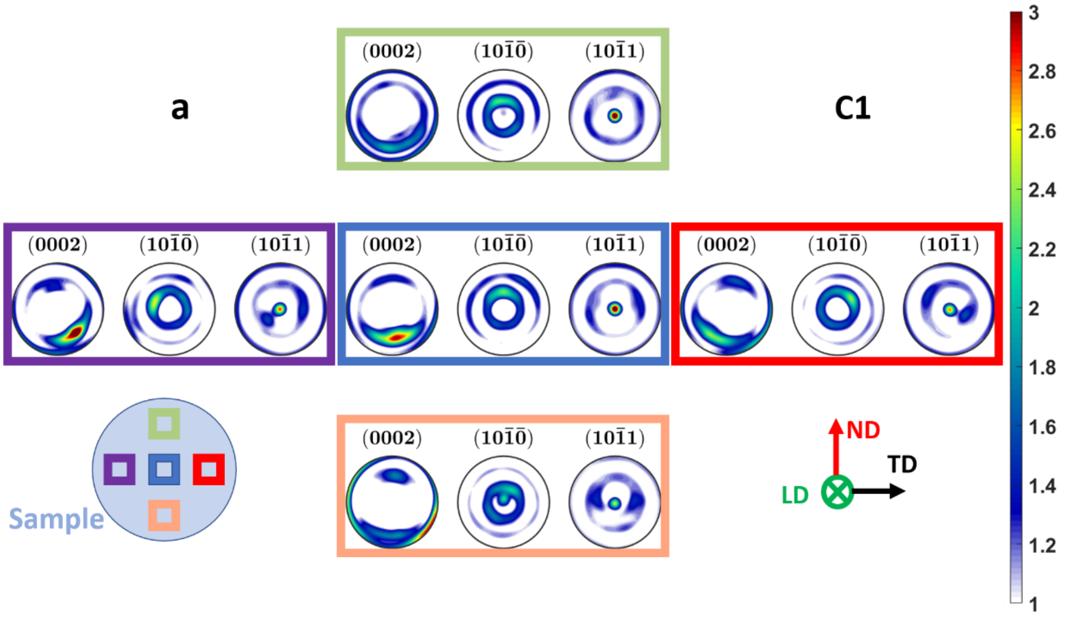

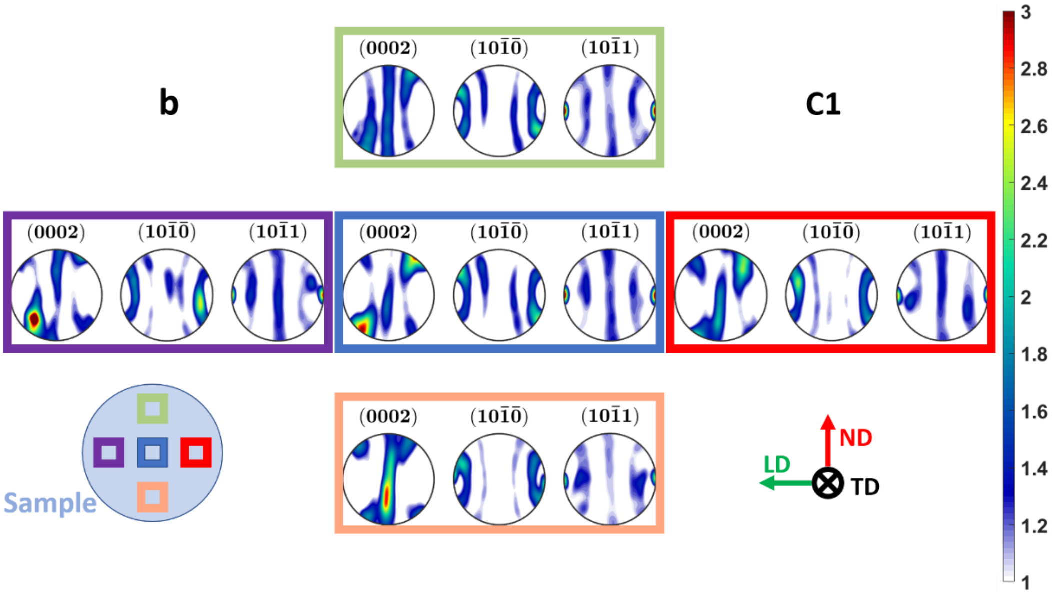

Fig. 4.18 Local X-ray texture distribution by means of PF diffraction of C1 sample in *a*-LD and *b*-TD view

If the PF resulted from the two experiments are compared, it is seen that results of both texture measurements are in good agreement. The same main features can be seen in X-ray PFs as in the case of EBSD PF, i.e., the main maxima of both type of PF are in coincidence within few degrees. Although, few differences can be spotted. The intensity distributions of X-ray textures are more continuous thanks to the larger investigated area. Moreover, a local maximum can be recognized between the LD and the ND pole in each X-ray basal PF (Fig. 4.18. a) except the top position. This component appears at the edge of the PF from TD view (Fig. 4.18 b.), between LD and ND, at the opposite side of the main maxima. But their overall intensity is lower than the main maxima and it is slightly above the random distribution.

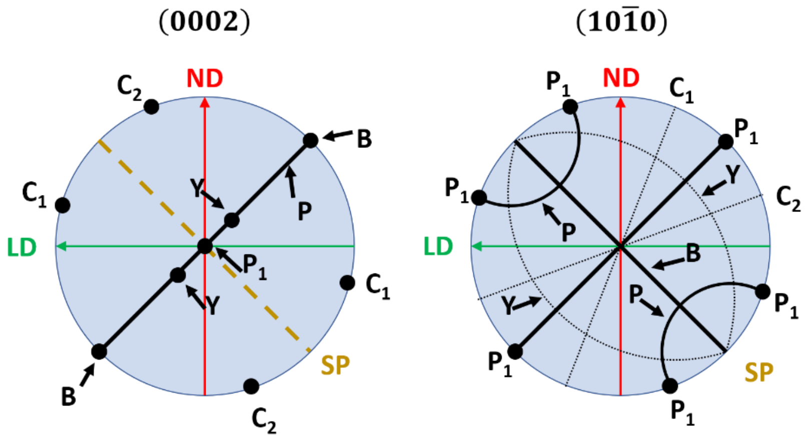
(0002) $(10\bar{1}0)$

Fig. 4.19 Schematic representation of shear texture components represented in (0002) and $(10\bar{1}0)$ PF's

These textures can be described in terms of fibers and orientations. Toth et. al. [89] identified the ideal fibers and orientations, together with their positions in PFs (Fig. 4.19) of hcp structure subjected to simple shear deformation. Although, they calculated with ideal c/a ratio, which is the most suitable for Mg, their findings can be applied in the description of ECAP textures of Ti also [90, 91].

In the reported literature dealing with ECAP-ed or C-ECAP-ed Ti textures, in the experimental PF, the clearly visible B fiber $\{11\bar{2}0\}\langle 1\bar{1}00\rangle$ and the P fiber $\{hkil\}\langle 1\bar{1}00\rangle$ appear in a slightly shifted position with respect to ideal fiber and orientation positions of the ideal hcp structure. These fibers can be partially identified in our case also. The earlier mentioned additional local maxima of basal PF, near to ND pole of the X-ray textures may be identified as C_2 fiber $(11\bar{2}0)[1102]$.

The PF maxima show similar features and positions with the reported ones [90, 91]. The most similar PF to the reported PF in the literature can be find in the center position, obviously, since the authors carried out their measurements in the center of the samples. The texture inhomogeneities in the sample can be explained by a potentially curved shear plane and by the inhomogeneous shear deformation through the sample cross section, as it was shown in [92]. Besides the strain field, this influences the texture formation in particular positions in the sample also. The shear process during C-ECAP is mirror symmetric along the ND direction in ideal case. Thus, mirror symmetry can be expected in texture formation also, with some deviation from it. This is clearly seen if both side part of X-ray PFs are compared in LD view (Fig. 4.18. a.). It seems that main texture components at side positions (indicated in purple and red frame) are rotated by few degrees around ND (each with opposite direction). The top, center and bottom parts exhibit very similar maxima positions in PF's. Only a minor rotation around LD can be spotted.

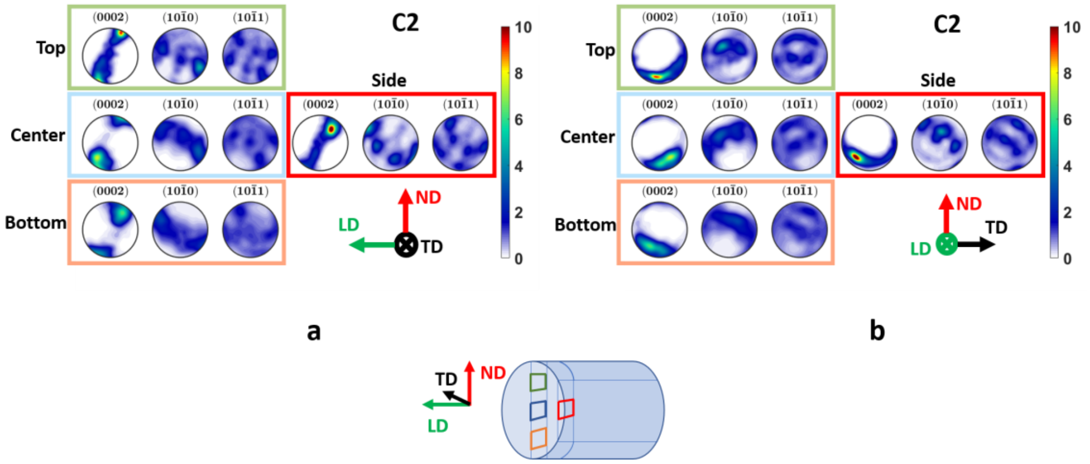

Fig. 4.20 Local EBSD texture distribution by means of PF in C2 sample in *a*-TD and *b*-LD view

In fig. 4.20, local EBSD-textures of the C2 sample are presented. If it is compared to the previous pass, it is seen, that the shear textures are getting more continuous with clearly defined global maxima. The intensities around the maxima are spread. The X-ray textures of the C2 sample have similar attributes. Also, it is seen that B fiber dominates the texture mainly at center and bottom parts (lack of the sign of P fiber in the surroundings of the center of the basal PF). The symmetric orientations of texture components between the two side parts are more pronounced, as it is seen in Fig. 4.21 b. (compared to Fig. 4.18 b) at side parts. Thanks to route A, the axial symmetry with respect to ND axis is kept since the rotation of the sample before reinserting to the C-ECAP should not change this symmetry.

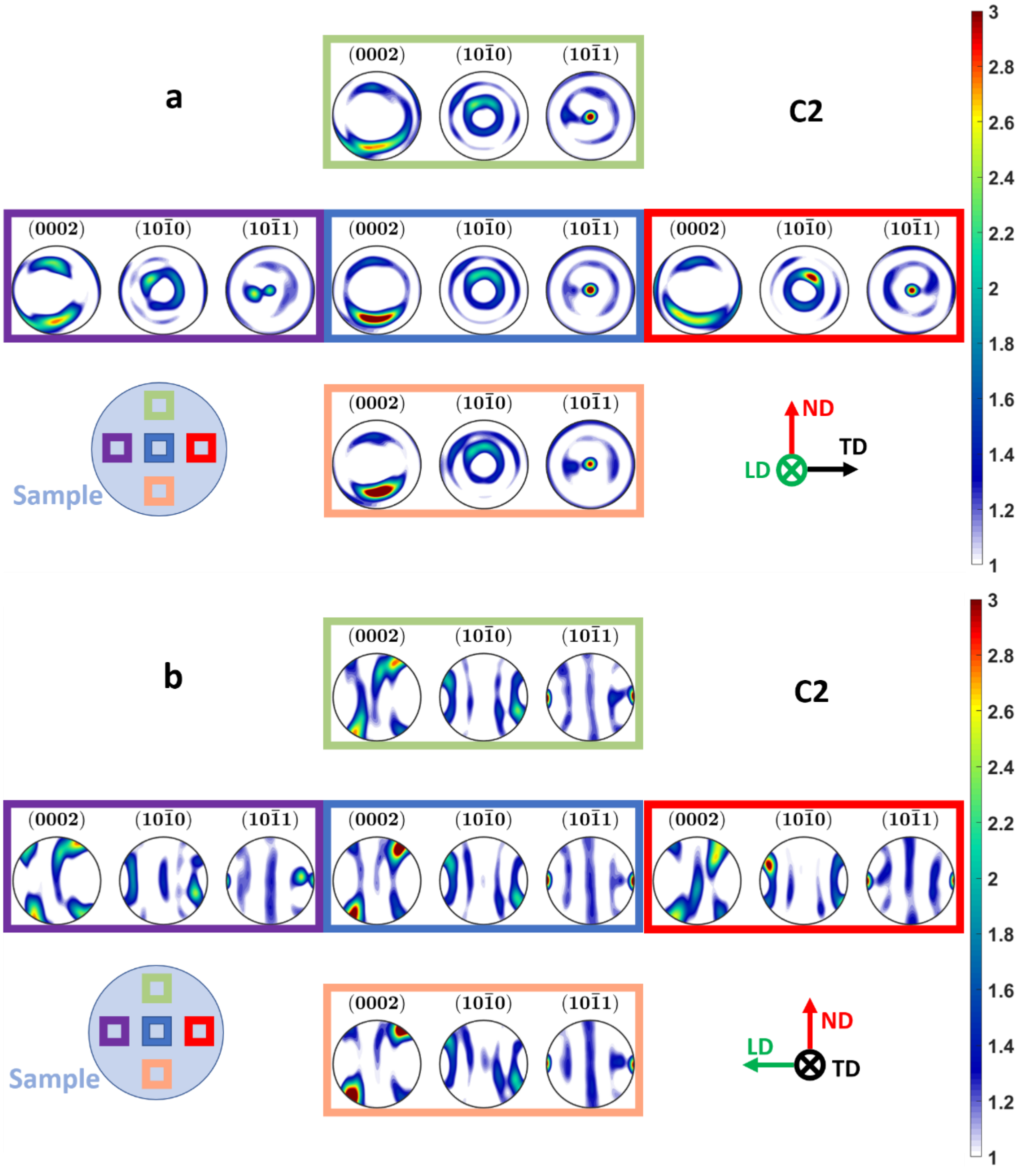

Fig. 4.21. Local X-ray texture distribution by means of PF, measured by X-ray diffraction of C2 sample in *a*-LD and *b*-TD view

The texture properties of the second pass can be explained by the more pronounced grain refinement process. As in the previous section, the C1 sample contains more non-refined grains than the C2 sample, this is more grains contribute to the observed texture, which became more continuous. Furthermore, the reorientation of finer grains with respect to the shear direction in the local shear plane is easier. Thus, the noticed rotation of texture components at side parts is more significant even more in this case.

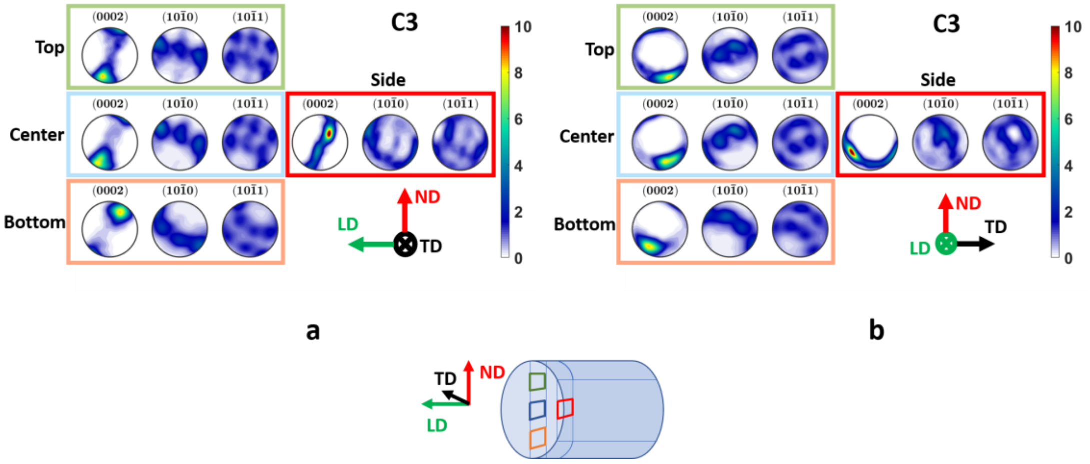

Fig. 4.22. Local EBSD-texture distribution by means of PF in C3 sample in *a*-TD and *b*-LD view

The measured textures from EBSD and X-ray diffraction experiments on C3 sample are presented in Fig. 4.22 and 4.23. Compared to previous passes, the texture became even more continuous in general. Shear textures with more spread character are still present; however, a texture component has been appeared clearly in X-ray textures at top and side parts (Fig. 4.23. a.), where the basal planes are near to parallel orientation to LD. This texture change can be a result of a slight grain growth [93], as it was presented in the previous chapter or a result of the formation of a strong P_1 orientation. As it was shown above, the curved shear plane plays important role in the reorientation of texture components at side positions.

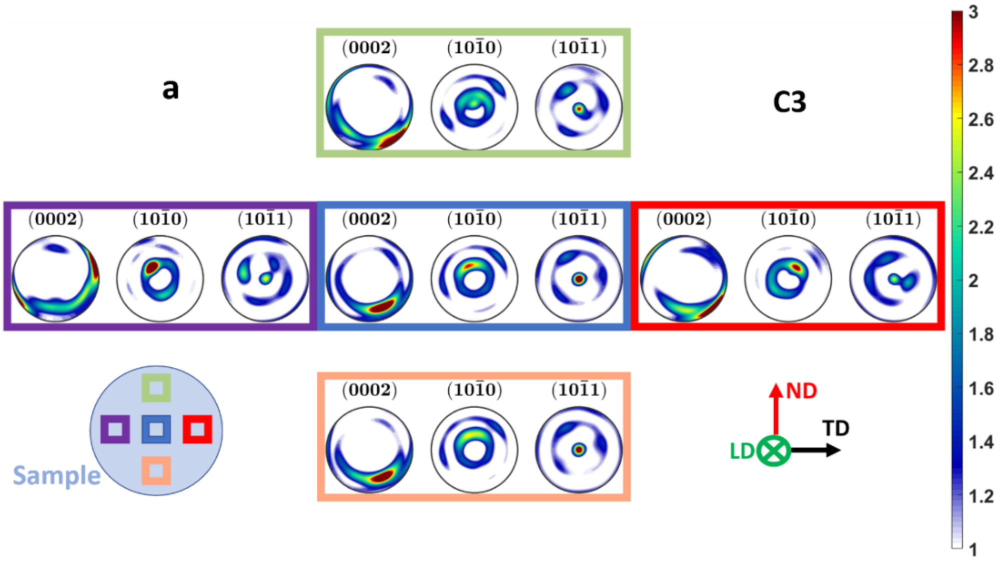

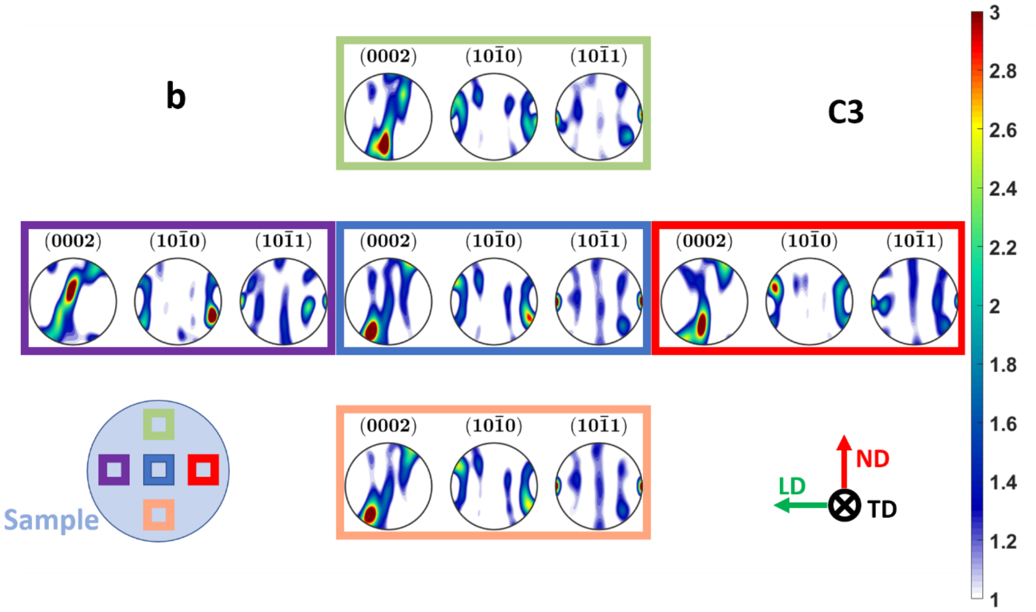

Fig. 4.23. Local X-ray texture distribution by means of PF in C3 sample in *a*-LD and *b*-TD view

4.2.3 Dislocation density by X-ray diffraction

Dislocation densities at particular positions were determined by x-ray diffraction method described in chapter 2.3. The investigated positions were the same as in the case of texture measurements. The second order restricted moment of the $(10\bar{1}1)$ diffraction peak intensities were analyzed by fitting eq. 8 on the $I(q)$ vs. ln $(\frac{q}{q_0})$ data. In this form, eq. 8 is linear with slope $\Lambda\langle\rho\rangle$. By determining Λ, the average dislocation density can be calculated. As we already know, this parameter depends on the diffraction vector $\vec{q}$, dislocation's Burgers $\vec{b}$ vector and on the so-called dislocation contrast factor C. Since there is no restriction on the possible dislocations, the average value of C of all possible dislocations in hcp structure was used. The dislocation densities of all three C-ECAP samples are summarized in Fig. 4.24.

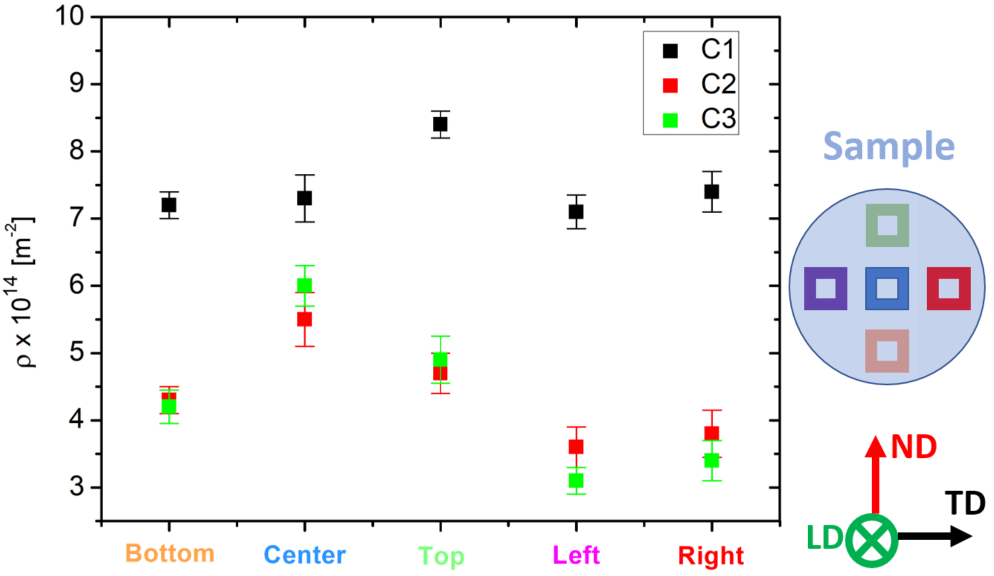

Fig. 4.24 Dislocation density distributions in C1, C2 and C3 samples

The values of dislocation densities are in order of $\sim 10^{14}\ [m^{-2}]$, which is roughly in accordance with values found by Gunderov et.al. [94]. The slight difference can be accounted for different processing conditions, like higher temperature than in their case, which enables the faster rise of the recovery processes.

As it is seen on Fig. 4.24. a slight gradient of dislocation density towards the edges of the sample can be observed in C1 specimen. The maximum is at top position while the edges, i.e top, bottom and side parts show almost the same dislocation density. The C2 and C3 samples exhibits almost identical distribution of dislocation densities. The generation and annihilation of dislocations are equilibrium. It is worth to note again, that simulations showed [56] temperature and strain gradients during C-ECAP process. The top position exhibits higher strains and lower temperatures than everywhere else. This is, the highest dislocation density can be expected in top positions. This can be observed at C1 sample on Fig. 4.24. However, after subsequent passes, central part exhibits the maximum dislocation density, and the top position has only the second highest value. This can be explained by the poor thermal conductivity of Ti. During the second and third pass, the edges of the cylindrical sample are heat treated while they reach the abutment, where the ECAP process happens. The bar shortly after this exits the whole machine and it is not exposed to further heat anymore. Thus, the sample after first pass exhibits dislocation density distribution corresponding to the strain distribution. As Ti has reduced heat conduction, the time, until the abutment is reached, is not enough to homogenize the temperature in the whole cross section.

This unwanted heat treatment may be responsible for reduced dislocation density in C2 and C3 samples, for slight grain growth and for additional texture component in C3 sample.

4.2.4 Microhardness measurement results

Microhardness measurements were conducted in the manner presented in chap. 2.5.6. Contour plots of measured values in the cross-section of samples are shown in Fig. 4.25. These HV values can be understood as the *relative* local yielding property of specimen since the indentation is a local plastic deformation process.

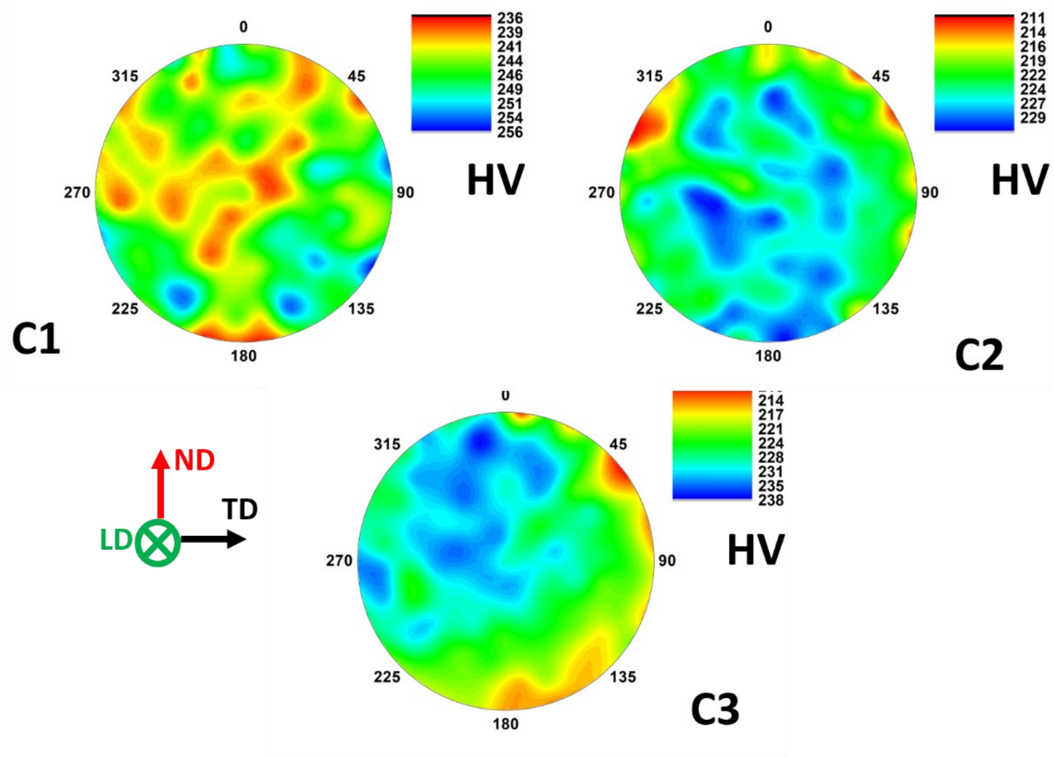

Fig. 4.25 Measured microhardness map of C1, C2 and C3 samples cross-section

In general, the C1 sample seems the hardest in general since its HV values are between 236 and 258, while C2 and C3 samples have values between 210 and 238. These values are in good agreement with HV values of conventional ECAP processed Ti in other work [95]. If we take a closer look, some harder and softer regions can be identified within samples. In C1 specimen, the near the edge region, between 90° and 180° is the hardest, it is followed by region near at the edge, between 225°and 270° and finally the region near 0° of the sample. In such a way, a "Y" shaped, softer region outlines in the surface. A vertical symmetry of the HV distribution can be found here also.

The C2 sample is the hardest around the central region towards 180°. Softer parts can be found in the upper semicircle of the cross section. The vertical symmetry is less pronounced in this case.

Higher HV values can be seen in the upper semicircle, mainly at left side, towards the center of C3 sample. Equivalently, the bottom part of the semicircle of the cross section is the softer region.

The variation of HV values can have several reasons based on the local microstructure properties and stress state [96, 97]. One of this reason is the grain size variation within the sample according to the citated literature. However, drastic changes in grain size were not observed, as it was seen in chapter about microstructure. Therefore, the distribution of residual stress acting only parallel to the surface affects mainly the microhardness distributions.

4.2.5 Neutron diffraction residual strain/stress scan

In the first part, ND scan results in the whole cross-section of the samples will be presented. In the second part, line scan results are given. In the first case 2 mm steps and 45° rotations were applied in the whole cross section of samples, while in the second case, 1 mm in line steps in TD direction of samples were used. Details of these experiments can be found in chapter 2.5.3.

For calculation of residual stresses from a the measured 2θ Bragg diffraction angles/interplanar distances, it is needed to estimate the diffraction elastic constants C_{ijkl} (chapter 2.1.2) and the stress-free d_{hkl}^{0} or θ_{hkl}^{0} for determination of strains. The

latter is dependent on C_{ijkl} since the stress-free reference was not available in our case. Therefore, the self-equilibrating property of residual stresses was used for estimation of the stress-free d^0_{hkl} of the $(10\bar{1}1)$ diffracting planes. It is assumed, that these planes represent well the macro-residual stress state of these samples.
As it was explained before, there are several approaches to calculate C_{ijkl}. In this work, the modified Eshelby self-consistent method for polycrystalline materials was used [98]. The elastic tensor C_{ijkl} can be expressed as:

$$C_{ijkl} = \sum_{r=1}^{N} c_r C_{ijkl}{}^{r} \left[I + \bar{S}_r(C_{ijkl}, f)\bar{L}_r^{-1}\{C_{ijkl}{}^{r} - C_{ijkl}\}\right]^{-1} \qquad \text{(a)}$$

Where r is the number of grains, c_r and $C_{ijkl}{}^{r}$ is the volume fraction and elastic tensor of r-th grain, I is a fourth order identity tensor and $\bar{S}_r(C_{ijkl}, f)$ is the Eshelby tensor as function of C_{ijkl} and orientation f of the r-th grain. The c_r is basically the *orientation distribution function* (ODF) evaluated at some orientation f in Euler space corresponding to the orientation of the r-th grain. The ODF was calculated from X-ray texture measurements. The Eshelby tensor depends also on Hill's polarization tensor, and their analytical form can be found in [98] and [99]. 10000 individual grain orientations with their volume fractions c_r was used based on the calculated ODF. The calculation of C_{ijkl} was done by an iterative approach in a MATLAB program written by the author of this work, the ODF estimation from texture measurements was made by MTEX software package in MATLAB. C_{ijkl} was calculated for each texture measurement positions for all C-ECAP processed samples.

The results of the strain scan in the C1 sample cross section perpendicular to cylinders axis are shown in Fig. 4.28. The maximum error is 29 με for all strains in this chapter. The distributions show that in axial direction, mainly strains with compressive character are developed while in hoop direction, tensile strains are dominant. In radial direction, tensile character of strains slightly exceeds except regions near bottom and near the side edges. The highest values of compressive and tensile strains in axial and hoop directions, - 320 and 220 με respectively, are concentrated mainly between the top and central position.

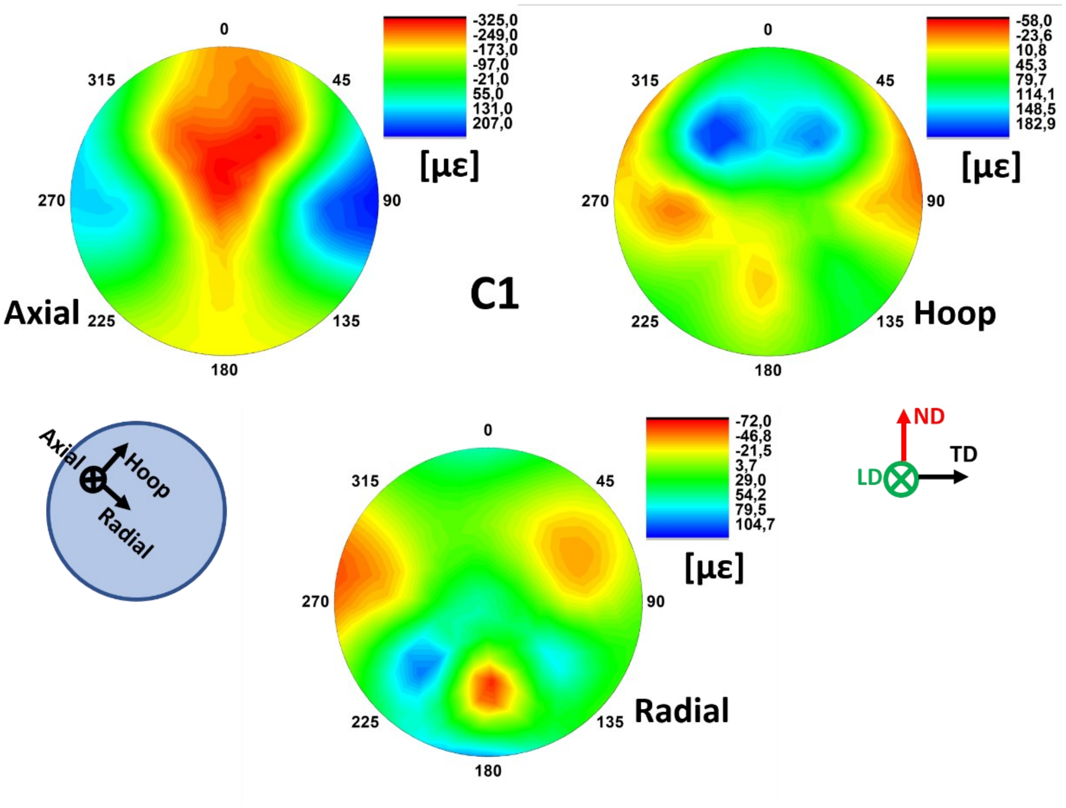

Fig. 4.26. The measured residual strain distribution in C1 sample cross-section

In axial direction a local maximum of compression strain is present, while in hoop direction, in the same position as in axial direction, two peaks of tensile strain evolved. An interesting distribution of residual strains is present in the radial direction. The upper part of the sample has nearly homogeneous distribution of strains, but the bottom part contains the maxima of local compression and tensile strains.

If we recall again the simulation results [56], surrounding of top part exhibits the largest deformation. Furthermore, the symmetry around vertical central line, i.e., around ND, is obvious. This is the result of the symmetrical behavior of ECAP process. These strain distributions and symmetry attributes are in agreement with previous results of texture and dislocation density.

The calculated residual stress distribution is presented in Fig. 4.27. the maximum error in stresses is about 9 MPa for all stress calculations in this chapter. The residual stress differences in the sample are 90 MPa, 34 MPa and 40 MPa for axial, hoop and radial directions, respectively. It is obvious, that the vertical symmetry is still present with some deviations. In axial direction, in central horizontal line compressive residual stress is developed. The area with largest compressive stress is between top and center positions. Two maxima of tensile stresses are present, in opposite position near 90° and 270°. The difference between magnitude of these local maxima is about 12 MPa. It is obvious from figure, that near these positions, tensile stresses are present also in hoop and radial directions, but with a more equal magnitude, 12-14 MPa. In hoop direction, stress gradients are concentrated mainly in the bottom part of cross section because above the central horizontal line, the sample has relatively homogeneous stress state. In the radial direction, near the top position, another local tensile maximum is developed. It can be concluded that it has also a vertical symmetry in the residual stress distribution in C1 sample.

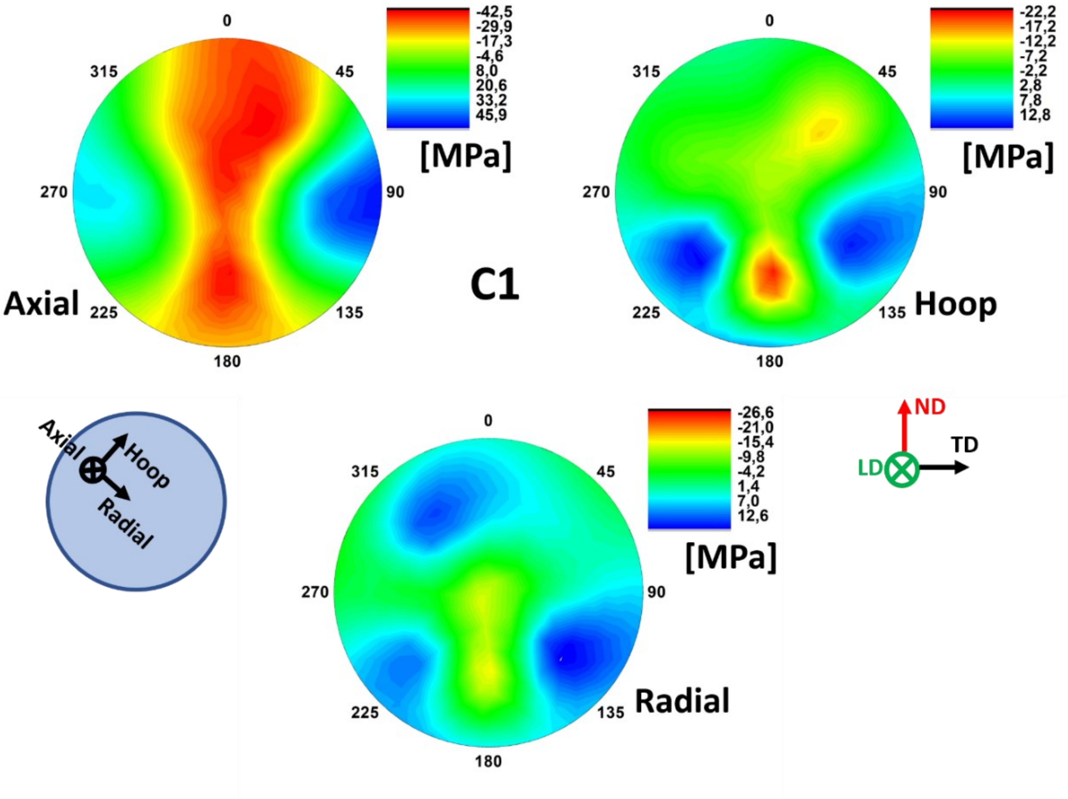

Fig. 4.27. Calculated axial, hoop (tangential) and radial residual stress distributions of C1 sample cross-section

There are only few articles which deals with residual stress/strain measurement with neutron diffraction technique in ECAP processed materials.

The numerical analysis of ECAP process is mainly focused on the behavior of plastic deformation during the treatment [100, 101]. Residual stresses were analyzed by finite element method (FEM) in various technical workpieces [102, 103]. The combination of ND technique with FEM to study conventional ECAP induced residual stresses in high purity copper can be found in [104]. It is worth to mention, it seems that authors of the latter citated work ignored the self-equilibrating property of residual stresses in their simulation. Nevertheless, similar trends of residual stress distributions can be spotted between our work and their work, even though Cu is an FCC structured material with different deformation characteristics than our HCP structured Ti. The axial stress distribution in Fig. 9. of [104] shows similar behavior to the present results, except the vertical central part.

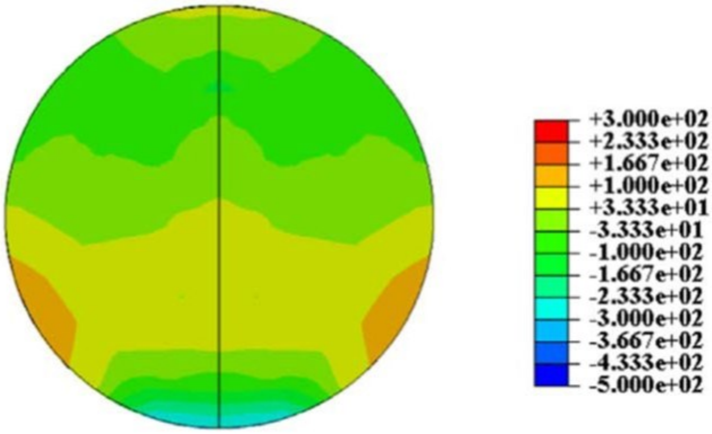

Fig. 9 from [104]

In their unloaded state, compressive stresses dominate the region near to the top and bottom part in axial direction. In regions near 90° - 135° and 225° - 270° at edges in our case and in their equivalent region, tensile stresses are developed. The texture plays an important role in the deformation properties of hcp materials, especially the orientation with respect to *c* direction, while in fcc metals texture is less important due to the equivalency of slip systems. Therefore, the differences in the development of residual stress distribution between the Cu and Ti results, respectively, are comprehensive.

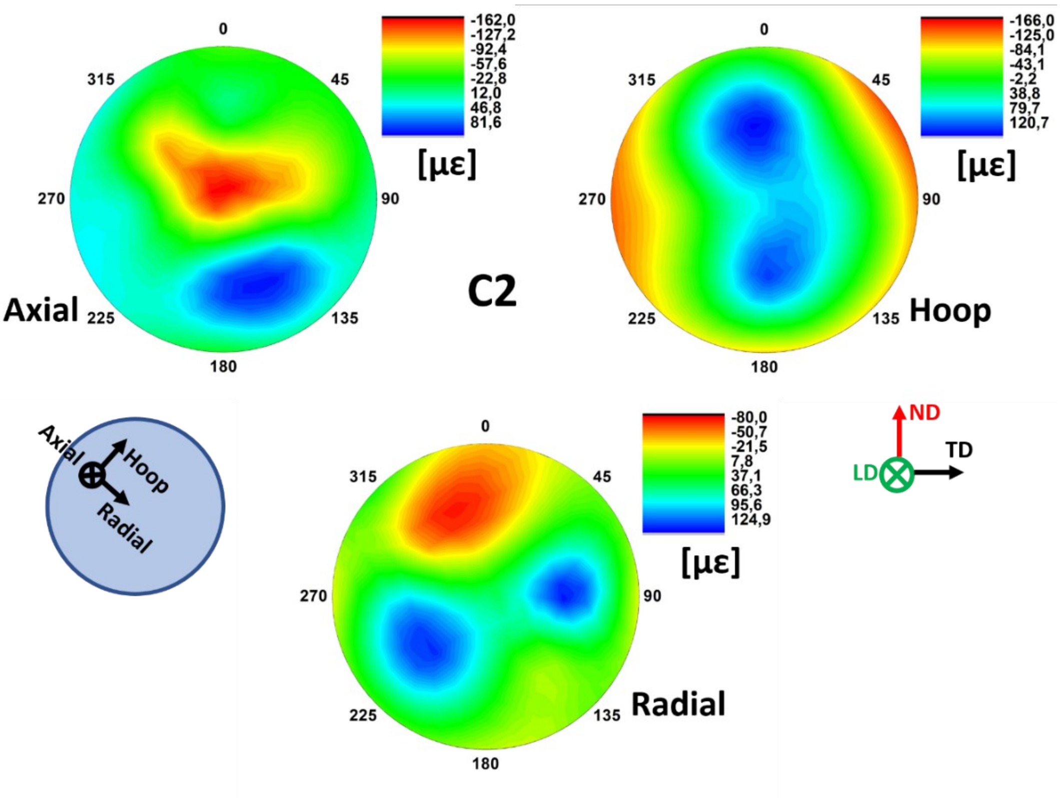

Fig. 4.28. The measured residual strain distribution in C2 sample cross-section

Residual strain distribution of C2 sample can be seen in Fig. 4.28. Compression strains still dominate in axial direction. In contrast to previous pass, mainly tensile strains developed in the radial direction. In hoop direction, tensile and compression strains are equally present. Furthermore, it can be noticed, that the axial strain difference between the maximum of compression and tensile strains is reduced by at least 300 με, but on the other hand, it is increased in hoop direction in contrast to C1 sample. Considering the local extreme values of strain distributions, in axial direction a tensile strain maximum is near to the bottom, and a compression strain maximum is at the center. In hoop direction, tensile strain is concentrated in the central vertical part, where two maxima are formed. These maxima are placed at opposite position to each other. In the radial direction, top region has a wide compression strain character. Furthermore, two localized tensile strain maxima can be found between the center and the side edges.

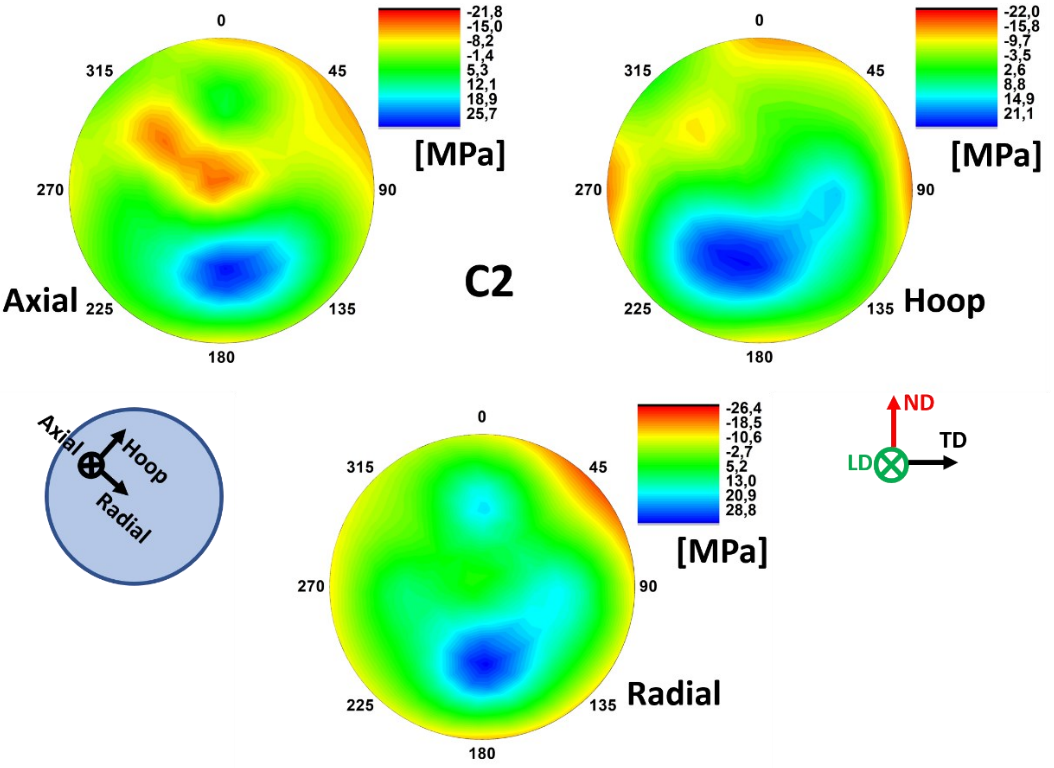

Fig.4. 29. Calculated axial, hoop (tangential) and radial residual stress distributions of C2 sample cross-section

The residual stress distributions of C2 sample are shown in Fig. 4.29. Compared to the previous sample, a noticeable different stress distribution is developed in every direction. Tensile stress maxima are mainly concentrated in the bottom semicircle of the cross section of the sample in every direction. The upper semicircle has mainly compression stresses in axial direction and exhibits slightly compression stress character in hoop direction. In radial direction, a local tensile maximum is developed between center and top positions. Nevertheless, the overall distribution became more homogeneous if it is compared to the C1 sample. The largest difference between C1 and C2 sample is in axial direction where the stress difference is reduced from 90 MPa to 47 MPa. It seems, that vertical symmetry of stress distribution is kept after the second pass although with some deviations near the edges.

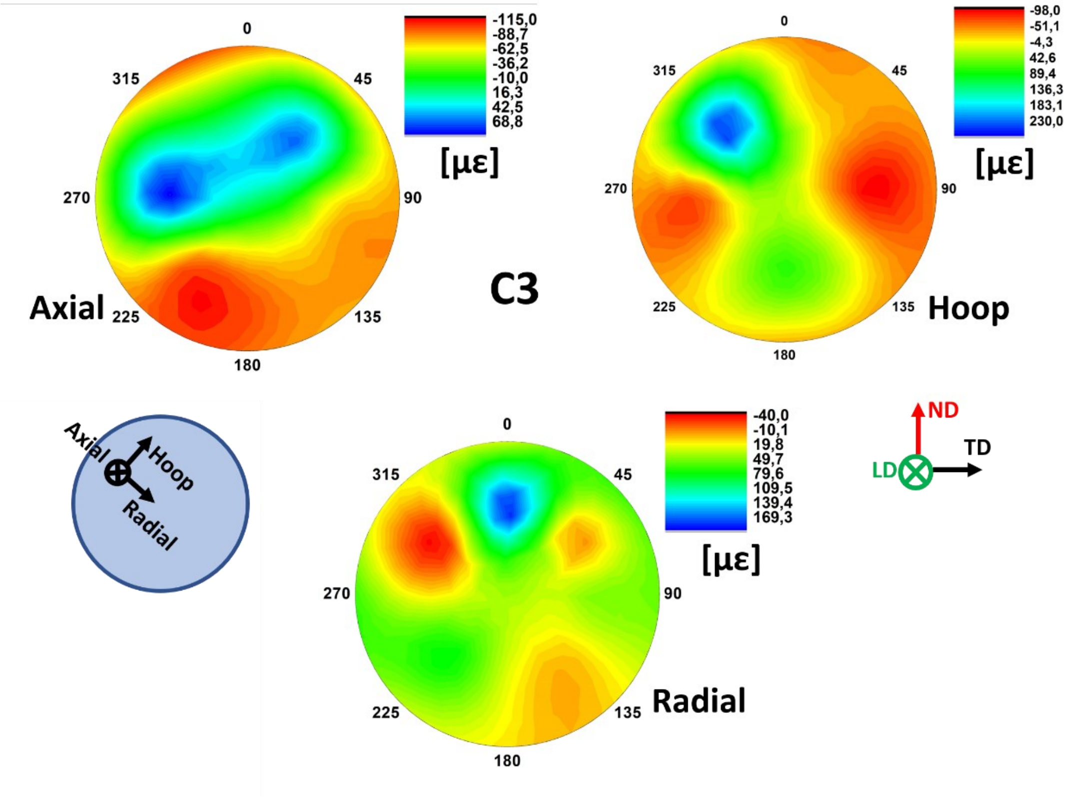

Fig. 4.30. The measured residual strain distribution in C3 sample cross-section

In Fig. 4.30. the residual strain distributions of the C3 sample are presented. Compression strains are dominant in axial direction and at side parts of hoop direction. Radial direction exhibits mainly tensile strains. Two local maxima of tensile strains are present in upper semicircle in axial direction. In hoop direction also two tensile maxima are present but one in top part and another in bottom part. The residual strain distribution with mainly tensile character in radial direction has tensile maximum right below top and two maxima of compression strain near the upper side parts. A misalignment can be seen in axial direction, which interrupts the symmetry around vertical axis. Nevertheless, if we allow some deviation and misalignment, symmetry is present in every direction. It is worth to note that strain gradients are increasing in hoop direction by every C-ECAP pass while they are decreasing in axial direction.

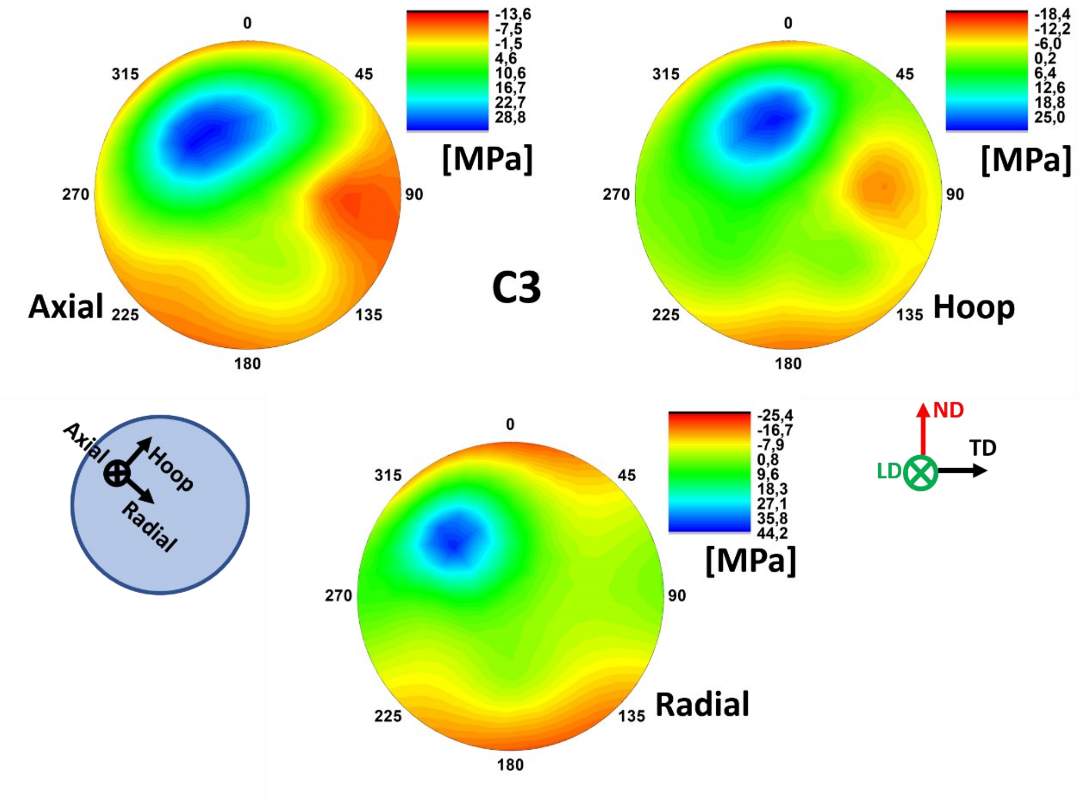

Fig. 4.31. Calculated axial, hoop (tangential) and radial residual stress distributions of C3 sample cross-section

The residual stress distribution of C3 sample is shown in Fig. 4.31. All three distributions shears similar features, namely a tensile stress maximum near top positions and extended compression region below it. The stress distributions became more homogeneous with respect to previous passes.

It was mentioned above, the residual stresses can affect the HV distribution. Radial and hoop stresses should be considered in our case, since microhardness measurements were done in the circular cross-section of our samples and the shape of the indentation is mainly dependent on the stresses acting parallel to the surface. Of course, cutting the sample in a plane interrupts the actual stress state of the bulk, however, it can be expected that similar distributions of radial and hoop residual stresses are acting in the measured surface as in the bulk. If some regions exhibit larger tensile stresses in the sum of hoop and radial stresses, then they should have higher average hardness values also, since the indentation process locally compresses the material mainly in direction parallel to the surface. In the same manner, a higher compression stress results in larger HV values. Strictly speaking, if somewhere is gradient of stresses, inevitably microhardness gradients appear also (beside other parameters kept constant). In Fig. 4.32, hoop + radial distributions are compared to microhardness results (Fig.4. 25).

In Fig. 4.32. in microhardness part, regions with coherently different HV values are separated by dark blue lines, i.e. where gradients are present. In C1 sample, three regions show higher tensile stress values: top region between 315° and 0°, and near the edges at 225° and 135°. Therefore, the region without these higher tensile is "Y" shaped. Basically, the same region with lower HV values can be spotted in microhardness map of the C1 sample. Maximum tensile stress values are located between the center and side part the C2 sample. The microhardness map shows similar behavior; however, it seems that higher HV values occupy a bit larger region. In the C3 sample, the correlation between tensile stress regions and higher HV values also correlates. The top part of the sample suffers from tensile stresses as well as from increased microhardness. It is worth to note that microhardness maps were done with 0.6 mm steps, while ND scan steps with 2 mm. That is why microhardness maps look "noisier" compared to stress distribution maps. However, even with this step difference, stress maps correlate well with HV maps if we consider the averages.

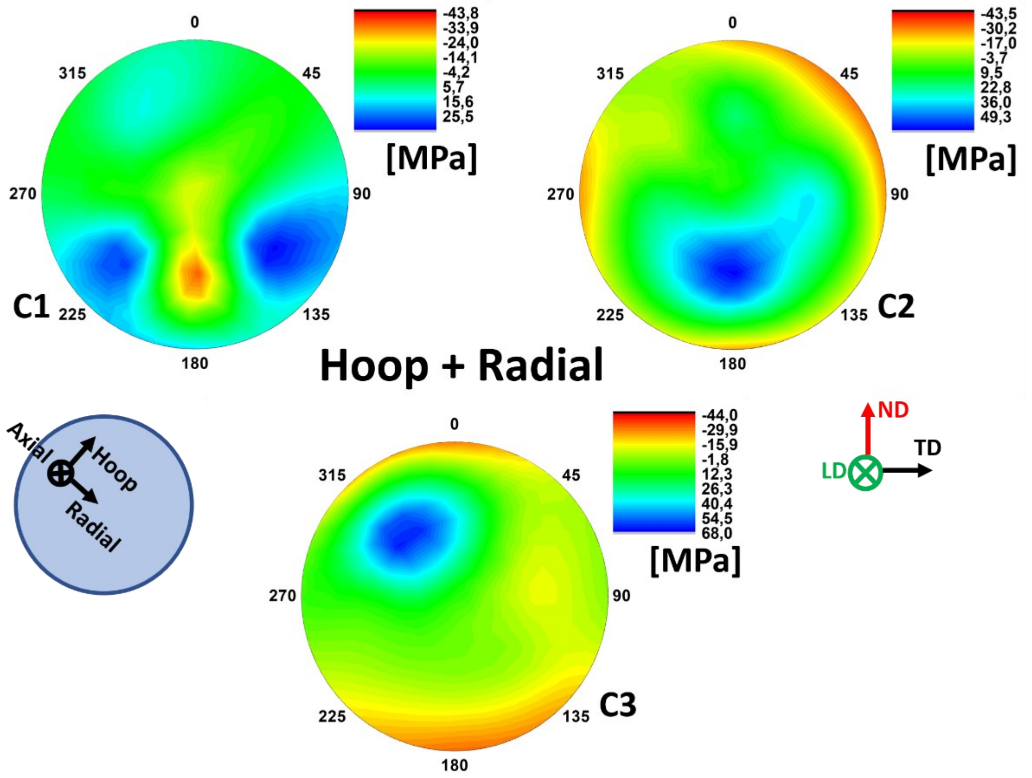

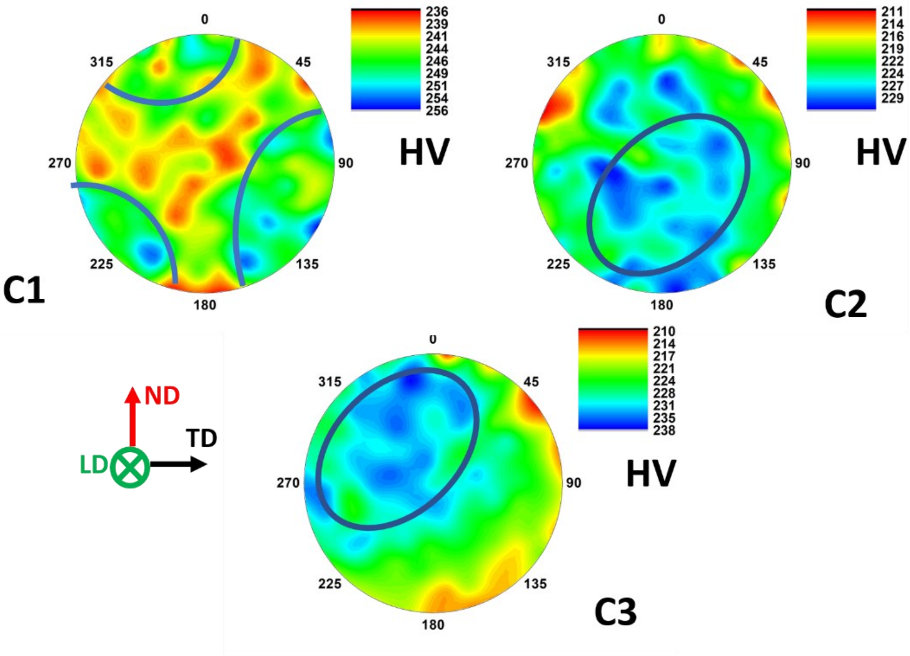

Fig. 4.32 Comparison of the sum of hoop and radial stresses with microhardness results. The regions with higher average HV values are bounded by dark blue lines

Von Mises yield criterion relates the yielding of the material in the presence of multiaxial loading. Mathematically σ_{VM} can be expressed as:

$$\sigma_{VM} = \sqrt{\frac{(\sigma_{axial}-\sigma_{hoop})^2+(\sigma_{hoop}-\sigma_{radial})^2+(\sigma_{axial}-\sigma_{radial})^2}{2}} \qquad \text{(b)}$$

where σ_i, $i \in (axial, hoop, radial)$, are stresses in their corresponding directions in our sample reference system. This concept enables us to determine the overall residual stress state of samples by a single parameter for each measurement point. Von Mises stresses also shows the regions where material is closer to the yielding stress, i.e., it is a precursor for non-homogeneous plastic deformation [105].

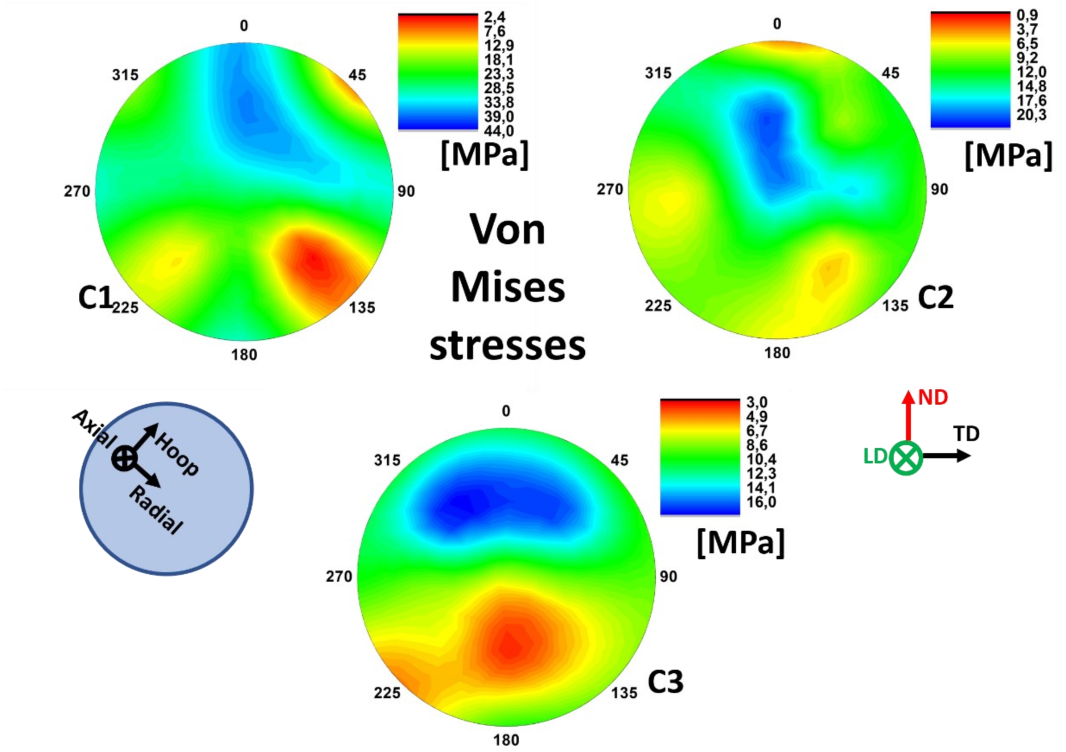

Fig. 4.33 Calculated Von Mises stresses in samples cross-section

The Von Mises (VM) stress distribution of all samples is depicted in Fig. 4.33. In all samples, the top region exhibits the highest VM stresses. In C1 sample, minima can be spotted in two locations, between the center and the edge at 135° and 225°. In C2 sample, minima are located in almost at the same position as in C1. The C3 sample exhibits an extensive minimum at the bottom semicircle of the cross section. C1 sample shows the largest VM stress maximum (40 MPa) and the C3 sample the lowest maximum (16MPa).

Again, we can recall the simulation in [56], the top part of samples exhibits the highest deformation. Therefore, it is straightforward that the overall residual stress has the largest magnitude in these regions although some of their components have different character than others. It can be seen, that with increasing C-ECAP passes the overall residual stresses became more and more homogeneous, i.e., with less local extremes with lower magnitude. Also, the average VM stresses are decreasing with increased number of passes. The average VM stresses are 24.7, 12.7 and 9.5 MPa for C1, C2 and C3 samples, respectively.

These variations in residual stresses can be explained by microstructure and process condition changes as we saw in previous chapters. Gradients related to microstructure are responsible for the rise of residual stresses mainly in materials with noncubic crystal symmetry for the following reasons. For example, neighbor regions with different textures attempt to strain differently each other when they are subjected to temperature changes due to the anisotropic thermal expansion coefficients of Ti [11]. In our case, this happens when the workpiece reaches the main deformation zone in the C-ECAP die where temperature gradient in time and space is present. Further, the material response for straining is different for different microstructures, which includes grain size (through Hall-Petch relation), texture (through elastic modulus tensor) and dislocation density (through Taylor formula) variations. As we saw earlier all these dispose spatial gradients in our samples which are gradually reduced with increasing number of C-ECAP passes. On the other hand, the imposed strain by C-ECAP process alone has gradient in the sample which is present in every passes. Thus, residual stresses can be expected after the fully homogeneous microstructure, although, their magnitude is decreased. The same overall behavior can be noticed in the VM stress distribution evolution as the function of the number of C-ECAP processes, as it was noted before.

Comparison of measurements on instruments HK9 and HK4

ND measurements on HK4 on SPN-100 instruments were done according to the description in chap. 2.5.3. The ND scan was performed only along a line in the TD direction, and the stress balance condition could not be applied in the whole cross section. Thus, the initial state ND data measured in axial direction were taken as the stress-free reference. Consequently, the residual strain values are related to this initial state, this is the effect of C-ECAP processing with respect to the initial state can be rele on samples relative to the untreated material.

The results of the experiments at horizontal channel HK4 on SPN-100 instrument are presented in Fig. 4.34. It is obvious that the C-ECAP treatment resulted in overall compression strain in each sample and each direction with respect to to initial state. Furthermore, it can be seen that the residual strain is gradually reduced in axial direction with increasing number of passes at the center of the samples, while the opposite tendency can be seen at the edges. In hoop direction, the second pass resulted in very similar strain distribution as in previous pass, only an additional compressive strain appeared. In radial direction, the strain distribution is quite homogeneous after the first and second pass. A relatively larger difference can be spotted only at the periphery. After the first and second pass, all strain distributions show a relatively similar character with some deviations. However, after the third pass, this symmetry is broken. The reason can be a misalignment during C-ECAP treatment and during the ND scan as well.

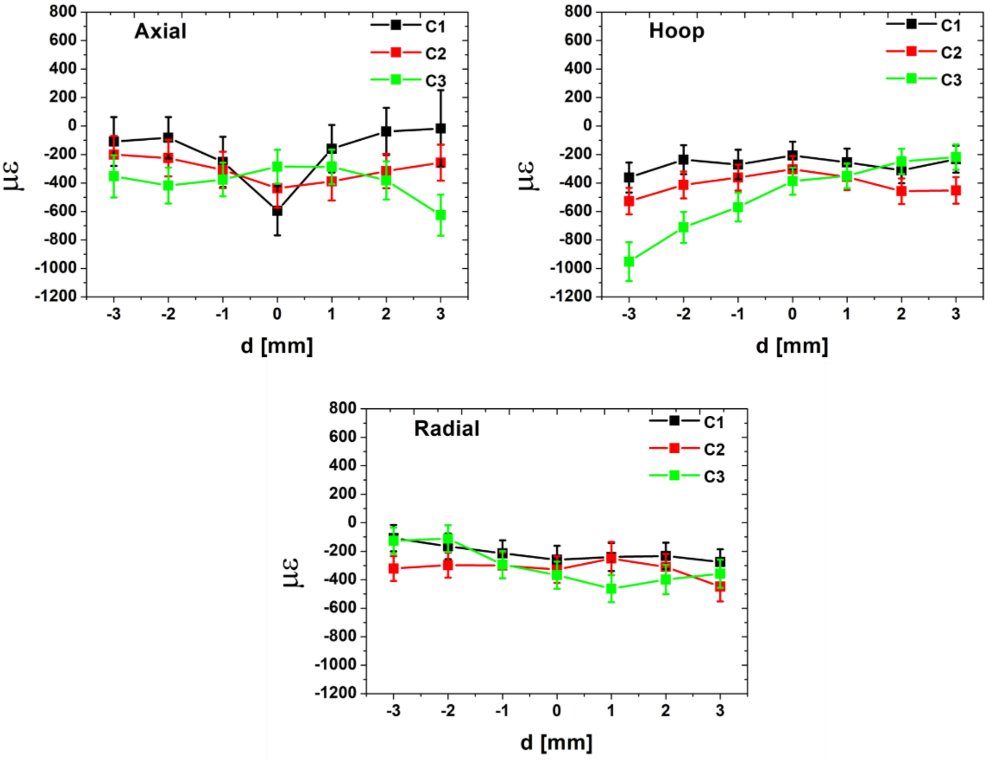

Fig. 4.34 Residual strains in axial, hoop and radial direction with respect to the axial direction of the initial state, for C1, C2 and C3 samples, measured at HK4 [54].

In the previous section, the full cross section ND scans measured at HK9 on TKSN-400 instrument were presented. As it was shown there, some deviation from the symmetric distribution of residual strains is present at every samples. In order to compare the results in TD of the two instruments (Fig. 4.35) and check the possible misalignment in measurements at HK4, results at HK9 were recalculated relative to the axial direction of initial state. More precisely, following the same approach as at HK4, the average of the measured Bragg diffraction angles or interplanar distances in axial direction of initial state, measured at HK9, was taken as stress free reference for calculation of residual strains.

It is obvious that the results of both instruments are in good agreement for C1 and C2 samples. Even the results of C3 sample in axial direction matches in both instruments. Only hoop and radial directions show larger differences between the two instruments. This can be explained by misalignment of C3 sample during these measurements. The axial direction measurements are done on samples in horizontal position with respect to cylindrical axis, while in radial and hoop direction measurements, the samples are in vertical position. This means, samples must be reoriented from horizontal to vertical position by the instrument operator and thus, misalignment is likely the reason of the mismatched results. Most probably, the line scan in these cases did not pass the sample center, therefore measurement points at the sample edges suffer from spurious strains due to the partially filled instrument gauge volume.

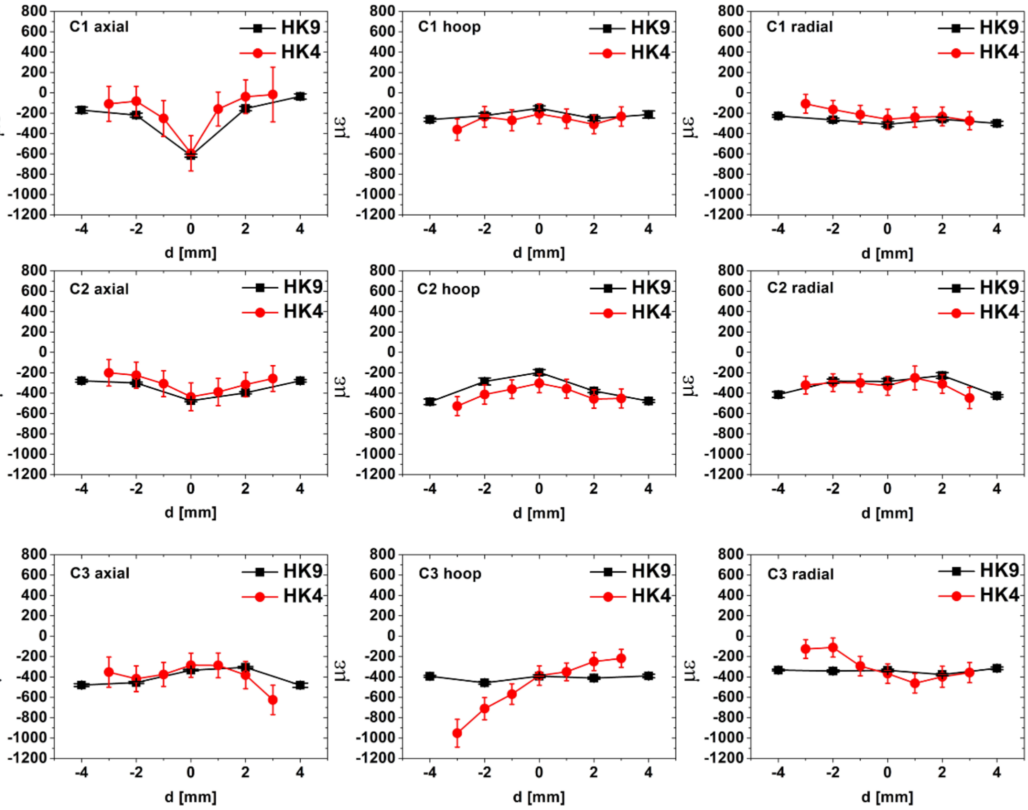

Fig. 4. 35 Comparison of results of experiments conducted on HK4 and HK9

4.3 Ti grade 2 CONFORM-ECAP and rotary swaging treated

As it was shown in chapters before, after the third C-ECAP treatment the grain refinement, various mechanical properties and the generation of crystal defects by means of dislocation density became saturated. Therefore, the C-ECAP processed Ti grade 2 was further treated by rotary swaging method at room temperature (cold working process) in order to produce a nanocrystalline microstructure. However, this has a cost in diameter reduction of cylindrical samples from around 10 mm to 4.6 mm which, according to eq. 3 in chapter 1.4.2., means approximately $\varepsilon = 1.55$ deformation.

4.3.1 Microstructure

Microstructure of the three samples were studied by transmission electron microscopy, especially in the ACOM TEM mode described in chapter 2.4.3. The microstructure can be seen in Fig. 4.36. where crystal orientation maps, similar to inverse pole figure maps, are presented for each sample.

As it can be seen, the microstructures consist of heavily distorted grains with large amount of low angle grain boundaries (red lines) in all three states. This is a result of the exposition to the large deformation. During the process low angle grain boundaries are formed. It can be noticed also that with increasing C-ECAP pass with combination of rotary swaging, the microstructure is becoming more homogeneous. The RS process was applied on series of specimens with decreasing grain size resulted from subsequent C-ECAP treatment.

In the C1+RS sample, the grains have grain size around 1 μm similarly to the 1x C-ECAP sample. However, several nanocrystalline grains with sizes around 100 nm can be spotted. The number of refined grains is increased in C2+RS and C3+RS samples. The C3+RS sample shows higher fraction of LAGBs.

Two types of dislocations can be distinguished: statistically stored and geometrically necessary dislocations (GND) [106, 107]. The latter type can cause significant local lattice curvature which can be identified in high resolution electron microscopy (SEM or TEM) [108]. Therefore, the analysis of orientation maps can provide valuable information about the GND content. The exact procedure behind the analysis can be find in [108]. This analysis was performed in our samples too and the results can be seen below.

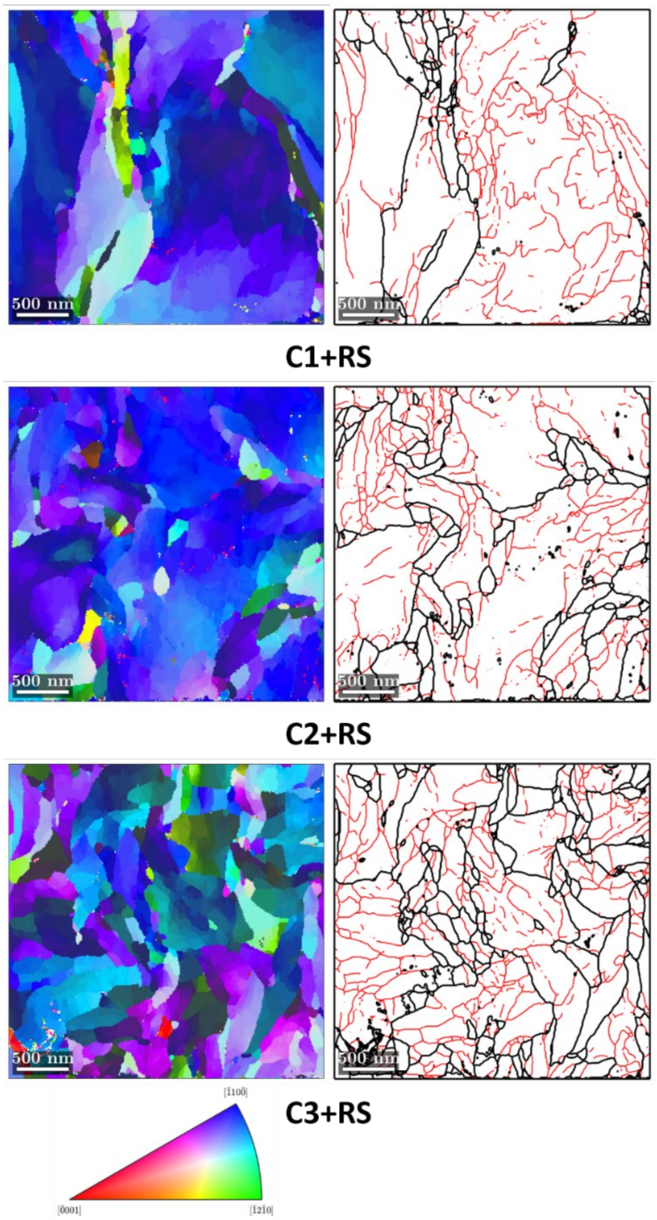

Fig.4. 36. Crystal orientation and grain boundary maps (HAGB-black lines, LAGB-red lines)

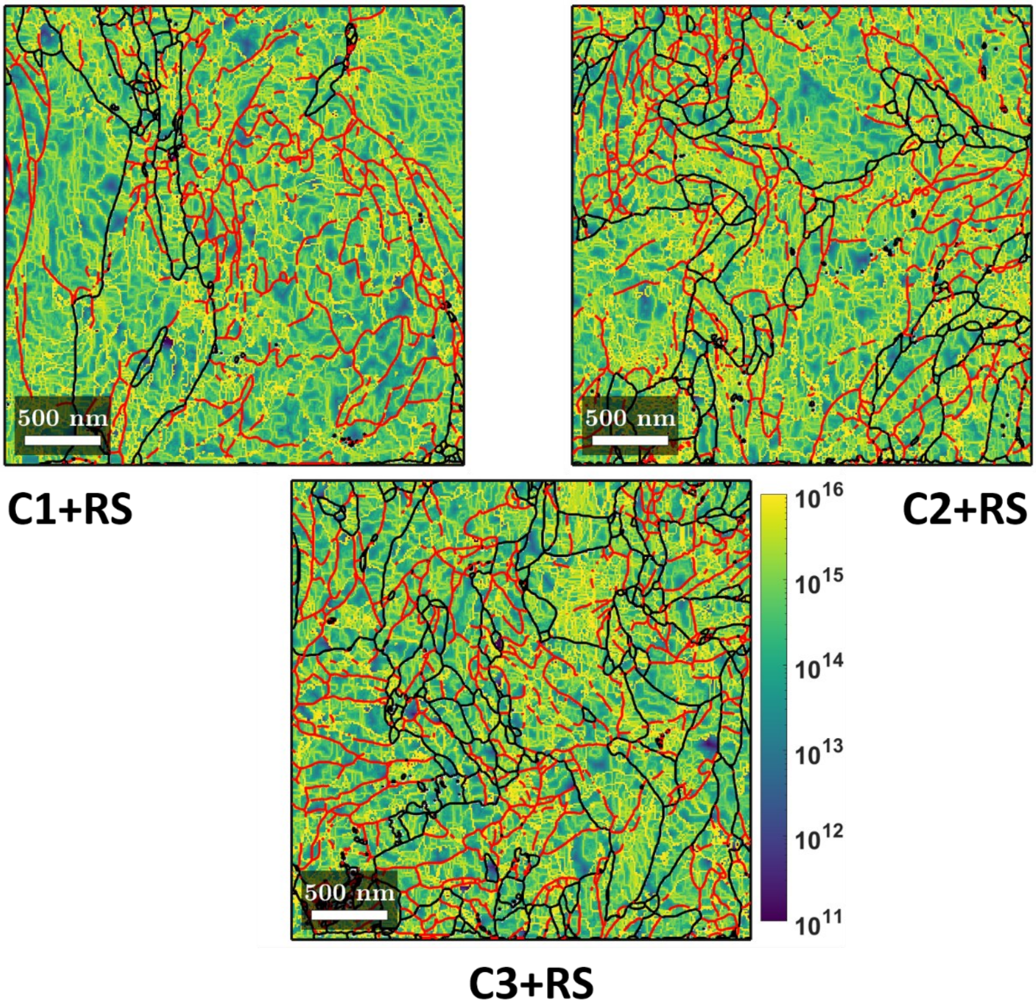

Fig. 4.37 GND density [m^{-2}] maps with HAGB (black lines) and LAGB (red lines)

In Fig. 4. 37., the distributions of GND are presented for each C-ECAP and RS processed samples. It is seen, that GND density configuration is not homogeneous, but they tend to form dense networks within grains. Regions with the highest densities are places where potential further LAGB's can form (yellow lines). The sizes of sub-grains are between few tens to few hundreds of nm. At the first sight, there is no difference between samples from the GND point of view. The estimated mean GND densities are 5.6, 5.6 and 6.5 x 10^{15} m^{-2} for C1+RS, C2+RS and for C3+RS samples, respectively. These values seem a bit overestimated, however, the already highly deformed C-ECAP processed material was treated with even higher deformation process at room temperature, so there was a less possibility for recovery processes to happen. The role of GNDs increases with the increasing deformation and with the increasing non-homogeneity of deformation [109]. The ratio of statistically stored dislocations to GNDs is estimated to 2:1 in small to medium strains, however it can be even higher at larger strains. In our case, $\varepsilon = 1.55$ is quite large and the geometry of samples requires non-homogeneous deformation. Therefore, the mean GND values may be realistic considering these facts.

4.3.2 Textures

Crystal orientation maps allowed us to estimate the micro-texture of the samples too. The evaluated PFs are basal (0002), prismatic $(10\bar{1}0)$ and 1st order pyramidal $(10\bar{1}1)$. The results are shown in Fig. 4. 38.

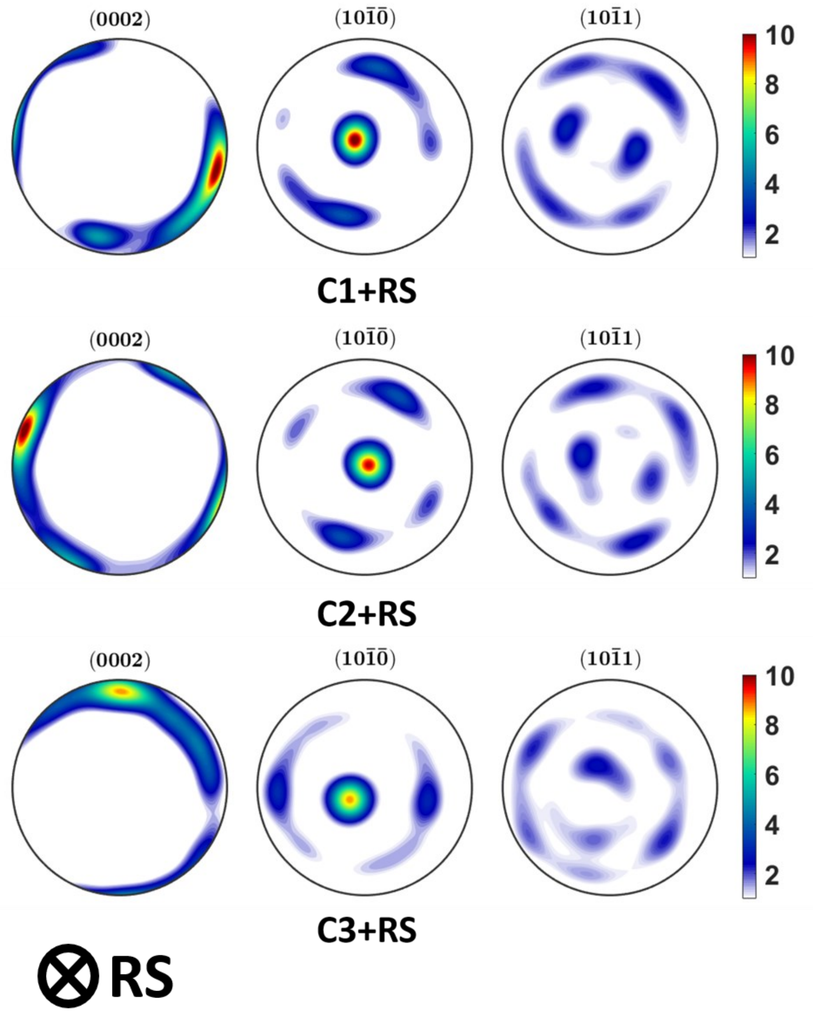

Fig. 4.38 Texture of C1+RS, C2+RS and C3+RS samples by means of PF with the processing direction indicated in the left bottom corner

As it can be noticed, strong $\langle 10\bar{1}0\rangle \parallel \overrightarrow{RS}$ fiber texture evolved during the process, in accordance with [13] and other works in [110, 111]. This type of texture is typical for pure Ti [112, 113] and also for Mg alloys [114, 115] after hydrostatic extrusion.

The C1+RS and C2+RS samples have almost identical texture while the C3+RS sample shows a slightly weaker preferred orientation. This could be deducted also from crystal orientation maps in Fig. 4.36. This can be the consequence of previous C-ECAP treatment, as it was discussed in the geometrical aspects of the grain structure.

4.3.3 In-situ neutron diffraction study during compression

Since RS processed samples can be considered as final product it is necessary to study their mechanical performance. The in-situ ND measurement method enables us to track mechanical properties in uniaxial loading. The parameters of the in-situ ND measurements can be found in chap. 2.5.3. Due to the strong texture, only the $(10\bar{1}0)$ diffracting planes were available with ND in axial direction. During the data acquisition, the deformation was stopped for an hour, as it was stated before.

The results of deformation tests in compression are seen in Fig. 4. 39. The deformation curves look similar on the first sight, especially in the elastic zone, where they are almost identical. This is evidenced by the fact, that the compression yield stress of all the samples is 660 ± 6 MPa. Furthermore, samples exhibit a reduced work hardening (tangent to the non-relaxed parts of the curves), which is a characteristic for UFG materials [116, 117, 118]. Nevertheless, the relatively large difference appeared above 3 % of the deformation, where the work hardening rate varies. To see the difference, work hardening rates can be plotted against the deformation.

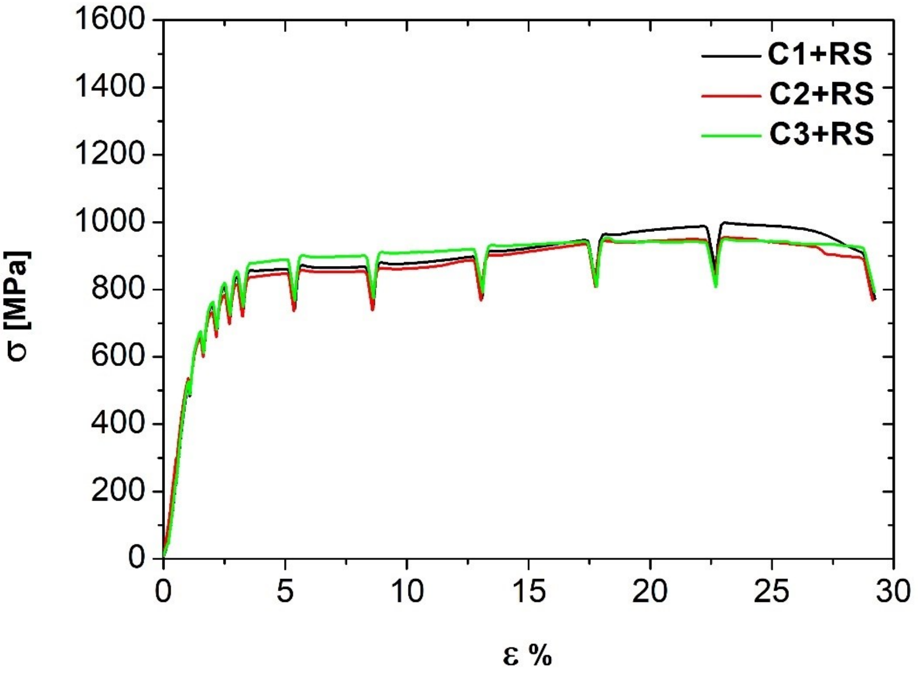

Fig. 4.39. True-stress true-strain deformation curves during in-situ measurements

If we take a closer look on the plastic zone above 3 % deformation, together with the average work hardening rates of each segment, the difference is conspicuous (Fig. 4. 40). It is seen that the C1+RS and the C2+RS samples work hardening rates varies significantly more than the C3+RS sample. This can indicate some differences in the deformation modes active during the plastic deformation of the material. Furthermore, it can be connected to the grain structure each of the samples. Similar characteristic of plastic deformation zone of the C1+RS and C2+RS samples was found in coarse grained pure Ti [119] in this straining stage, however, on a much larger scale of stress differences. The C3+RS samples plastic deformation shows identical behavior with the nanocrystalline pure Ti with grainsize of 120 nm found by a previous work [120].

The plastic deformation of the samples can be separated into three clearly distinct stages, according to the variation of work hardening rates (Fig. 4.40): before 5%, between 5 % and 15 %; and after 15 %, denoted as stage I, II and III. It is seen that C3+RS sample is quite flat in the II and III stages, compared to another samples and the boundary between these stages is not so pronounced.

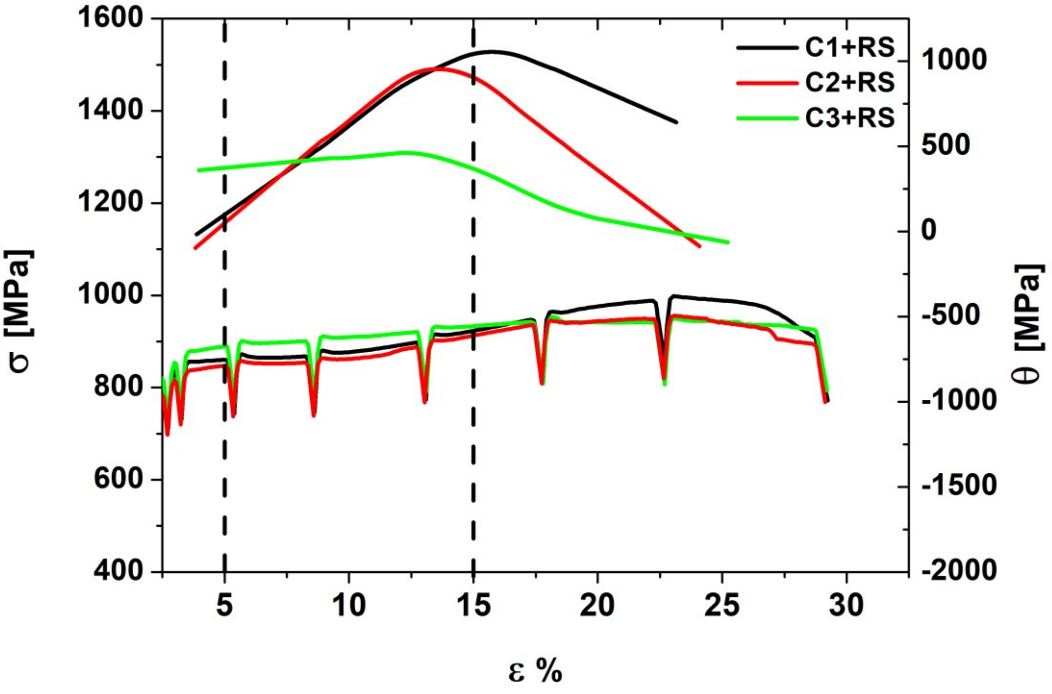

Fig. 4. 40 True-stress true-strain deformation curves during in-situ measurements and the corresponding work hardening rates in plastic region from 2.5 % of deformation, dashed lines indicate the boundaries of deformation stages

In order of further understanding of the roles of these stages, it is worth to mention some facts. The lowest critical resolved shear stress of the available slip systems of HCP Ti at room temperature has the prismatic slip system $(10\bar{1}0)\langle 11\bar{2}0\rangle$, followed by pyramidal $(10\bar{1}1)\langle 11\bar{2}0\rangle$ or basal $(0002)\langle 11\bar{2}0\rangle$ slip systems (there is no unanimous consensus which has lower CRSS between these two [121]) and by pyramidal slip systems $(10\bar{1}1)\langle 11\bar{2}3\rangle$ or $(11\bar{2}2)\langle 11\bar{2}3\rangle$ with the largest CRSS. The macroscopic stress needed for activation of a particular slip system is calculated by dividing its CRSS with Schmid factor of a particular slip system in the current crystal and loading direction configuration. Due to the texture of our samples, in our geometry, basal planes are parallel to the loading direction, therefore their Schmid factor is zero and they cannot be activated. According to $(10\bar{1}1)$ PFs in Fig. 4. 38. prismatic planes are perpendicular to the loading direction, which would also indicate zero Schmid factor, however from the hexagonal symmetry and from the geometry of the hcp lattice it comes, that in sum, two times more prismatic planes are tilted by 60° from the loading direction and the slip direction of $\langle\vec{a}\rangle$ dislocations is tilted by 30° from loading direction in these planes. These together indicate 0.43 Schmid factor, which is almost ideal. Pyramidal slip system $(10\bar{1}1)\langle11\bar{2}0\rangle$ has identical Schmid factor as prismatic. These slip systems can be easily activated in contrast to $\langle\vec{c}+\vec{a}\rangle$ dislocation which have much higher CRSS than before mentioned slip systems with $\langle\vec{a}\rangle$ dislocations. However, still there is a need of a deformation mode, which enables deformation in $\vec{c}$ direction with less CRSS than pyramidal $\langle\vec{c}+\vec{a}\rangle$ dislocations to ensure the Von Mises criterion of homogeneous deformation of polycrystalline materials. Here comes the role of deformation twinning which was discussed in detail in chap. 1.3.2.

The above-mentioned stages present during plastic deformation of samples are connected to twinning mechanism too, as it was shown in [119]. The onset of stage II is correlated with the start of the deformation twinning followed by simultaneous twin nucleation and growth. The increasing work hardening rate in this stage can be explained by the fact that twin boundaries serve as obstacles for $\langle\vec{a}\rangle$ dislocations in systems which are non-coplanar with the twins.

Due to the texture of our samples, the $\vec{c}$ direction was perpendicular to the loading direction. Since the material is compressed and the volume should be conserved, the direction perpendicular to loading axis should exhibit extension, i.e., tensile strain is present in crystallographic $\vec{c}$ direction. Therefore, tensile twinning is expected as an additional deformation mode beside $\langle\vec{a}\rangle$ dislocations. The most common tensile twinning mode in pure Ti is $\{10\bar{1}2\}\pm\langle10\bar{1}\bar{1}\rangle$. Just a reminder, this type of twin reorientates the twinned part in such a way that the basal plane is almost parallel to a prismatic plane, i.e., the twins $\vec{c}$ axis is perpendicular to the parent lattices $\vec{c}$ axis. The whole process is schematically represented in Fig. 4.42.

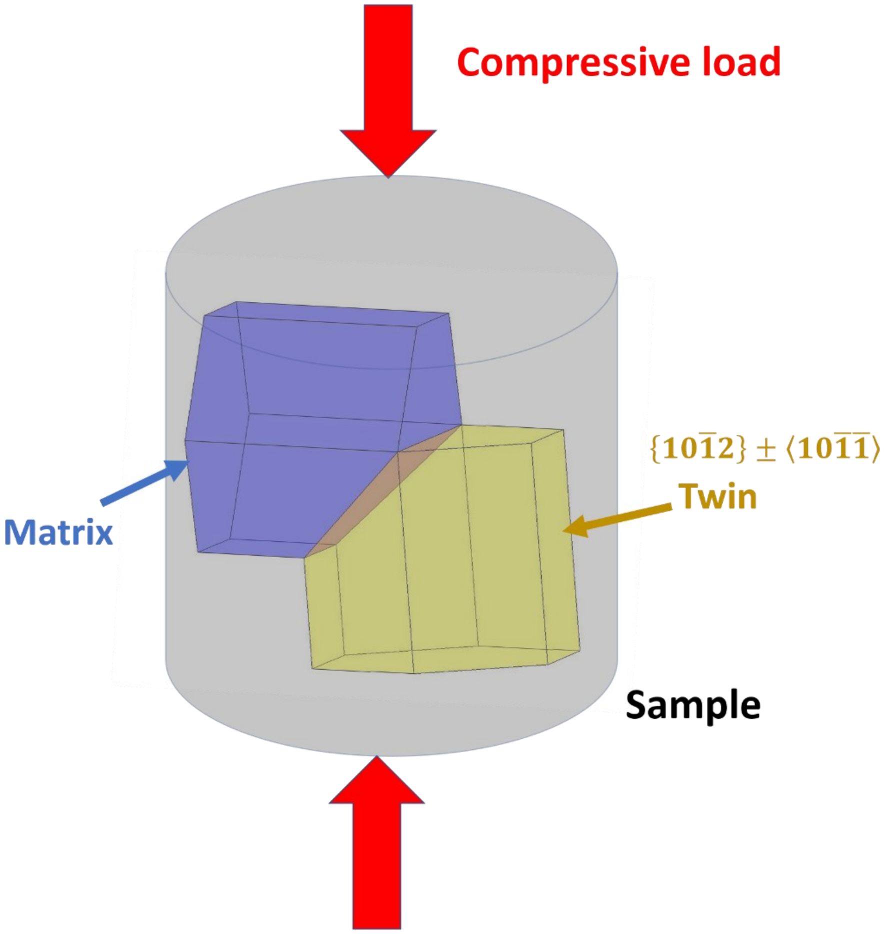

Fig. 4. 41 Twinning mechanism during compressive load with respect of the texture of the samples

In our detector configuration $(2\theta_D = 30°)$ and used neutron wavelength $\lambda = 1.2$ Å, theoretically, three diffraction peaks could be observed in 2D PSD, from crystallographic planes $(10\bar{1}0)$, (0002) and $(10\bar{1}1)$ in ascending order of 2θ Bragg diffraction angles. Therefore, the evolution of these peaks could be followed during the deformation.

In Fig. 4.42, the relative intensities of $(10\bar{1}0)$, (0002) and $(10\bar{1}1)$ diffraction peaks are presented for each sample against the true strain. The most probable boundaries of the deformation stages mentioned above are marked with dashed lines. It is seen that the intensity of $(10\bar{1}0)$ peak is rapidly decreasing from the beginning of the plastic deformation until around 16-17% of total true deformation in each sample with almost the same rate. The minimum is around 0.3 for C1+RS and C2+RS samples but 0.4 for C3+RS specimen.

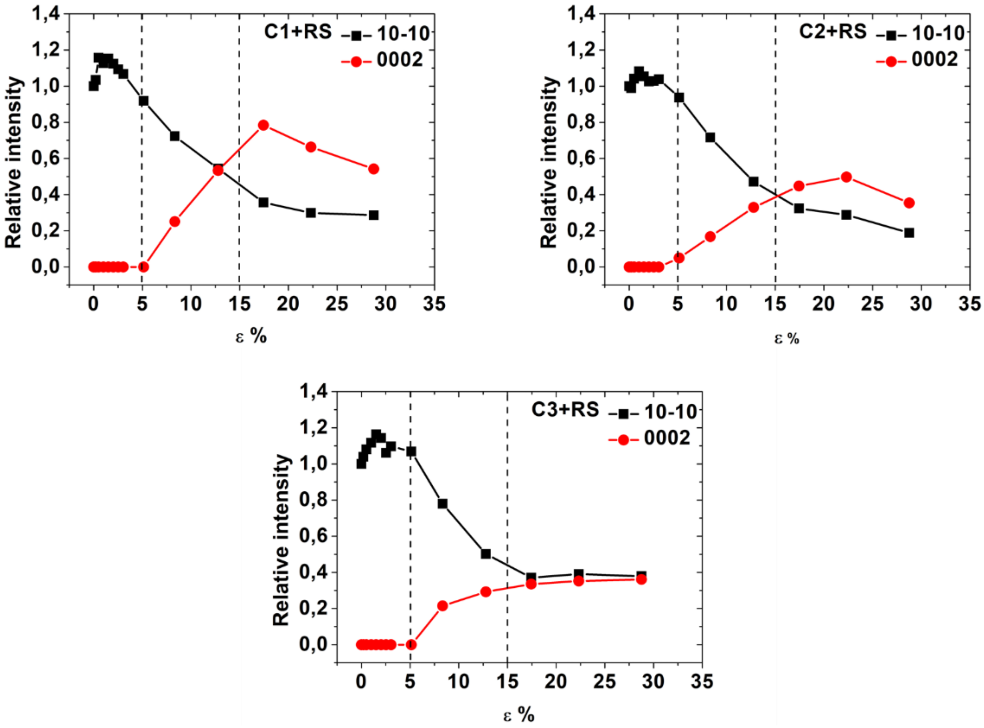

Fig. 4. 42 Relative intensity evolutions with deformation of $(10\bar{1}0)$ and (0002) diffraction peaks, dashed lines indicate the boundaries of deformation stages

On the other hand, the intensity of diffraction peak from basal (0002) planes is increasing from about 5-6 % of total true deformation, however, their evolution is different for different samples. The rise of the intensity of (0002) peaks is around 5% of deformation in each sample and the saturation is achieved near 17%, 18-20% and 8-11% of the deformation for C1+RS, C2+RS and C3+RS samples, respectively. It is interesting to notice, that relative intensities are gradually decreased and flattened.

The rise of (0002) peak is an evidence of the onset of twinning mechanism, especially of the $\{10\bar{1}2\} \pm \langle 10\bar{1}\bar{1}\rangle$ twinning system. The relative intensities can be associated with the relative volume fraction of twins since the intensity of diffracted neutrons is directly proportional to the diffracting volume. Therefore, the (0002) intensities in our C1+RS sample can be compared to twin volume fractions in literature as in Fig. 8 in [119]. The two graphs show very similar characteristics.

As it was discussed few paragraphs above, the twinning is responsible for increased work hardening rate. However, in our case, the grainsize also affects the twinning volume fractions and therefore the overall mechanical response during the plastic deformation for the following reasons. As it was shown in the microstructure analysis of these samples, the grainsize is decreasing gradually, or better said, the fraction of large grains is decreasing gradually from C1+RS to C3+RS sample, where the latter shows quite homogeneous grain structure already. In larger grains the twinning is more probably than in smaller grains, therefore, the decreasing fraction of larger grains indicates the decreasing twinning activity and volume fraction, that can be seen from C1+RS to C3+RS samples. When the twinning is saturated, the material starts to behave as purely nanocrystalline material with reduced work hardening. This is due to the dynamic recovery processes where the creation and annihilation of dislocations is in equilibrium. This is dependent on density of crystal defects within a grain. And why is that only after saturated twinning activity? Simply because when twinning is saturated, there is only left refined grains (twinned or parent grain) with large densities of dislocations where the above-mentioned equilibrium may occur. Before the saturation, there is no equilibrium, and the movement of newly generated dislocations is hindered by twin boundaries which results in increased work hardening.

If we look on lattice strain (LS) evolution of $(10\bar{1}0)$ planes (Fig. 4.43), it is seen that there is no significant difference between samples in the elastic region. On the other hand, few differences can be spotted in the plastic regime. In C1+RS, C2+RS and C3+RS samples, the compression LS is gradually decreasing until 12.5, 17.5% and 5% of deformation, respectively. The LS evolution of C1+RS and C2+RS samples are very similar until 12.5 % of deformation. From 17.5 % of deformation, the LS evolution of C2+RS and C3+RS samples show similar behavior. As a consequence, the deformation behavior on microscopic scale of the C2+RS sample can be described as the combination of C1+RS and C3+RS samples. This can be related to twin growth for the following reasons. Twinning in general reduces the average grain size. In C1+RS sample, the average grain size is probably still quite large after the twin growth saturation. However, in C2+RS sample, the saturation of twin growth probably resulted in microstructure which is more similar to C3 sample. Therefore, the deformation behavior of C2+RS sample resembles more C3+RS sample after the twin growth saturation.

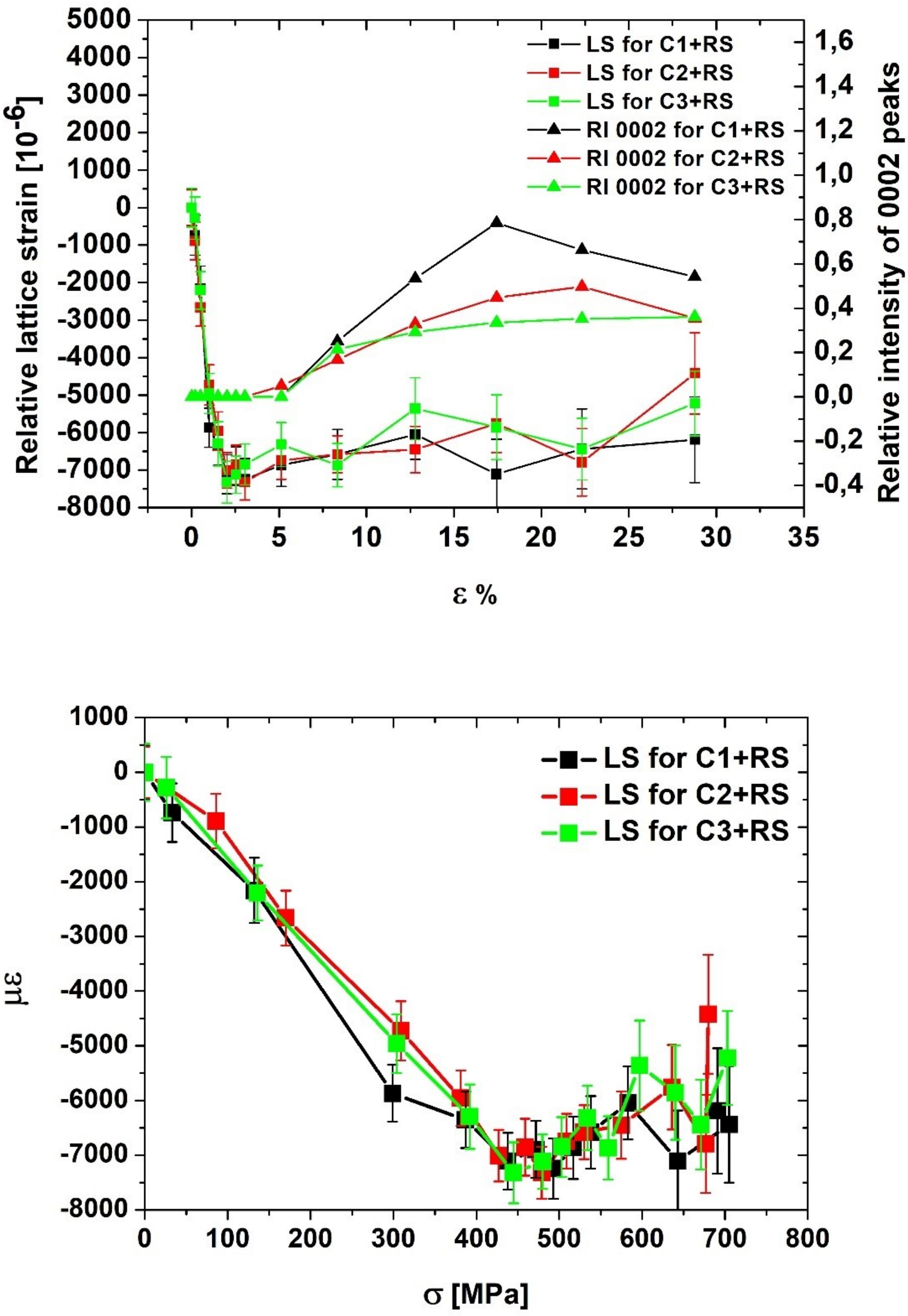

Fig. 4.43 LS and relative intensity evolution during the deformation.

Conclusions

In this thesis, the evolution of the residual stress field of the UFG structured commercially pure Titanium grade 2 prepared by multiple pass of CONFORM ECAP was studied by neutron diffraction technique. In order to elucidate the local microstructure, texture, dislocation density and yielding behavior responsible for the residual stress distribution in the material, detailed EBSD, X-ray and mechanical experiments were conducted. The microstructure of the subsequent rotary swaging treated nanocrystalline material was investigated by ACOM TEM method and the deformation mechanism during compression was studied by in-situ neutron diffraction. Based on the experimental results, the following conclusions can be drawn:

1. **Microstructural gradients within the samples after C-ECAP processing**
    a. Grain size and texture gradients are present after the first pass of C-ECAP. Higher fraction of finer grains can be found at side and bottom parts. The larger grains have elongated shapes, whereas the fine grains have rather equiaxed morphology. Accordingly, the rotation of texture components is more pronounced at the side parts. This effect can be ascribed to the inhomogeneous strain and temperature distribution during the C-ECAP treatment. With increasing number of passes the gradients reduce.
    b. The total dislocation density is the highest after the first pass. Locally, the highest dislocation density was measured at the top position after the first pass and at the center of the samples after 2nd and 3rd pass, respectively. The lowest densities are at the side parts in all cases.
    c. Harder and softer regions can be found also in microhardness maps. After the first pass, a “Y” shaped softer region is present in the cross section of the sample. After the second pass, the central and bottom regions exhibit higher HV values in contrast to sample after the third pass where top regions are harder.
    d. The residual stress distribution exhibits a vertical symmetry. The largest residual stress is concentrated in the top part of samples, as it was

expected from simulations. The residual stress in samples is reduced gradually by increased number of passes. The stress gradients are the consequence of grain structure, texture and dislocation density gradients.

2. **Microstructure and deformation behavior of the C-ECAP and rotary swaged material**

   a. The additional rotary swaging treatment resulted in further grain refinement – a nanocrystalline structure is achieved. The same trend in the fraction of larger grains can be noticed as at samples treated only C-ECAP method, i.e., larger grains gradually disappear from the grain structure.

   b. Strong fiber texture with $\langle 10\bar{1}0\rangle \parallel \overrightarrow{RS}$ is formed after RS treatment. However, in 3x C-ECAP + RS specimen, it is a slightly weaker than in 1x and 2x C-ECAP + RS samples.

   c. The deformation twinning was identified as the major deformation mechanism. Its activity decreases gradually for 2x and 3x C-ECAP + RS samples, as a consequence of grain size reduction.

Bibliography

[1] ELIAS, C. N., LIMA, H. C. J., VALIEV, R. Z., MEYERS, M. A. (2008). Biomedical applications of titanium and its alloys. *The Journal of The Minerals, Metals & Materials Society*, 60 (3), 46–49.

[2] LOTKOV, A. I., BATURIN, A. A., GRISHKOV, V. N., KOPYLOV, V. I. (2007). Possible role of crystal structure defects in grain structure nanofragmentation under severe cold plastic deformation of metals and alloys. *Physical Mesomechanics*, 10 (3-4), 179–189.

[3] SABIROV, I., PEREZ-PRADO, M. T., MURASHKIN, M., MOLINA-ALDAREGUIA, J. M., BOBRUK, E. V., YUNUSOVA, N. F., VALIEV, R. Z. (2010). Application of equal channel angular pressing with parallel channels for grain refinement in aluminium alloys and its effect on deformation behavior. *International Journal of Material Forming,* 3 (1), 411–414.

[4] XU, C., SCHROEDER, S., BERBON, P. B., LANGDON, T. G. (2010). Principles of ECAP–Conform as a continuous process for achieving grain refinement: Application to an aluminum alloy. *Acta Materialia*, 58 (4), 1379-1386.

[5] MEDVEDEV, A., NG, H. P., LAPOVOK, R., ESTRIN, Y., LOWE, T. C., ANUMALASETTY, V. N. (2015). Comparison of laboratory-scale and industrial-scale equal channel angular pressing of commercial purity titanium. *Materials Letters*, 145, 308–311.

[6] DJAVANROODI, F., OMRANPOUR, B., EBRAHIMI, M., SEDIGHI, M. (2012), Designing of ECAP parameters based on strain distribution uniformity. *Progress in Natural Science: Materials International.*, 22 (5), 452–460.

[7] HOLMBERG, J., STEUWER, A., STORMVINTER, A., KRISTOFFERSEN, H., HAAKANEN, M., BERGLUND, J. (2016). Residual stress state in an induction hardened steel bar determined by synchrotron- and neutron diffraction compared to results from lab-XRD. *Materials Science and Engineering: A,* 667, 199–207.

[8] LEE, D.-H., SEOK, M.-Y., ZHAO, Y., CHOI, I.-C., HE, J., LU, Z., SUH, J.-Y., RAMAMURTY, U., KAWASAKI, M., LANGDON, T. G., JANG, J.-I. (2016). Spherical nanoindentation creep behavior of nanocrystalline and coarse-grained CoCrFeMnNi high-entropy alloys. *Acta Materialia*, 109, 314-322.

[9] LEYENS, C., PETERS, M. (2003). *Titanium and titanium alloys*. Wiley-VCH, Weinheim. ISBN:9783527305346.

[10] LÜTJERING, G., WILLIAMS, J. C. (2007). *Titanium*. 2nd edition. Springer, Berlin, Heidelberg, New York. ISBN 978-3-540-71397-5.

[11] PAWAR, R. R., DESHPANDE, V. T. (1968). The anisotropy of the thermal expansion of [alpha]-titanium. *Acta Crystallographica Section A*, 24 (2), 316-317.

[12] SPREADBOROUGH, J., CHRISTIAN, J. W. (1959). The measurements of the lattice expansions and Debye temperatures of titanium and silver by x-ray methods. *Proceedings of the Physical Society*, 74 (5), 609 – 615.

[13] PALÁN, J., PROCHÁZKA, R., DŽUGAN, J., NACHÁZEL, J., DUCHEK, M., NÉMETH, G., MÁTHIS, K., MINÁRIK, P., HORVÁTH, K. (2018). Comprehensive Evaluation of the Properties of Ultrafine to Nanocrystalline Grade 2 Titanium Wires. *Materials*, 11 (12), 2522.

[14] TYSON, W. R. (1969). Solution hardening of titanium by oxygen. *Scripta Metallurgica*, 3 (12), 917-921.

[15] WASZ, M. L., BROTZEN, F. R., MCLELLAN, R. B., GRIFFIN, A. J. (2013). Effect of oxygen and hydrogen on mechanical properties of commercial purity titanium. *International Materials Reviews*, 41 (1), 1-12.

[16] AMERICAN SOCIETY for METALS (1990). *Metals handbook. Volume 2, Properties and selection: nonferrous alloys and special-purpose materials*. 10th edition. ASM International, Metals Park, Ohio, ISBN 0871703785 9780871703781.

[17] SINGH, A. K., SCHWARZER, R. A. (2000). Texture and anisotropy of mechanical properties in titanium and its alloys. *Zeitschrift fur Metallkunde*, 91 (9), 702–716.

[18] MURTY, K. L. (2003). Effect of c/a-Ratio on Crystallographic Texture and Mechanical Anisotropy of Hexagonal Close Packed Metals. *Materials Science Forum*, 426-432 (4), 3575-3580.

[19] WANG, L., ZHANG, H., HUANG, G., CAO, M., CAO, X., MOSTAED, E., VEDANI, M. (2016). Formability and anisotropy of the mechanical properties in commercially pure titanium after various routes normal and different speed rolling. *Journal of Materials Research*, 31(21), 3372–3380.

[20] SRINIVASAN, N., VELMURUGAN, R., KUMAR, R., SINGH, S. K., PANT, B. (2016). Deformation behavior of commercially pure (CP) titanium under equi-biaxial tension. *Materials Science and Engineering: A*, 674, 540-551.

[21] SINHA, S., GHOSH, A., GURAO, N. P. (2016). Effect of initial orientation on the tensile properties of commercially pure titanium, *Philosophical Magazine*, 96 (15), 1485-1508.

[22] MISES, R.V. (1928). Mechanik der plastischen Formänderung von Kristallen. *ZAMM - Zeitschrift für Angewandte Mathematik und Mechanik*, 8, 161-185.

[23] DING, R., GONG, J., WILKINSON, A. J., JONES, I. P. (2014). 〈c+a〉 Dislocations in deformed Ti–6Al–4V micro-cantilevers. *Acta Materialia*, 76, 127-134.

[24] REN, J. Q., WANG, Q., LU, X. F., LIU, W. F., ZHANG, P. L., ZHANG, X. B. (2018). Effect of oxygen content on active deformation systems in pure titanium polycrystals. *Materials Science and Engineering: A*, 731, 530–538.

[25] TONDA, H., ANDO, S. (2002). Effect of temperature and shear direction on yield stress by {11-22} 〈11-23〉 slip in HCP metals. *Metallurgical and Materials Transactions A*, 33 (3), 831–836.

[26] JONES, I. P., HUTCHINSON, W. B. (1981). Stress-state dependence of slip in Titanium-6Al-4V and other H.C.P. metals. *Acta Metallurgica*, 29 (3), 951-968.

[27] LI, H., MASON, D. E., BIELER T. R., BOEHLERT C. J., CRIMP, M. A. (2013). Methodology for estimating the critical resolved shear stress ratios of a-phase Ti using EBSD-based trace analysis. *Acta Materialia,* 61 (20), 7555–7567.

[28] WILLIAMS, J. C., BAGGERLY, R. G., PATON, N. E. (2002). Deformation behavior of HCP Ti-Al alloy single crystals. *Metallurgical and Materials Transactions A*, 33 (3), 837–850.

[29] CAHN, R. W. (1954). Twinned crystals. *Advances in Physics*, 3 (12), 363-445.

[30] FARKAS, G. (2017). *Investigation of residual stresses and deformation mechanisms of magnesium-based composites by means of neutron diffraction and acoustic emission methods*. Dissertation thesis. Charles University, Faculty of Mathematics and Physics, Department of Physics of Materials.

[31] CHRISTIAN J. W., MAHAJAN, S. (1995). Deformation twinning. *Progress in Materials Science*, 39 (1-2), 1-157.

[32] YOO, M. H. (1981). Slip, Twinning, and Fracture in Hexagonal Close-Packed Metals. M*etallurgical Transactions A*, 12 (3), 409-418.

[33] PATON, N. E., BACKOFEN, W. A. (1970). Plastic deformation of titanium at elevated temperatures. *Metallurgical Transactions,* 1 (10), 2839- 2847.

[34] GLAVICIC, M. G., SALEM, A. A., SEMIATIN, S. L. (2004). X-ray line-broadening analysis of deformation mechanisms during rolling of commercial-purity titanium, *Acta Materialia*, 52 (3), 647-655.

[35] ZAEFFERER, S. (2003). A study of active deformation systems in titanium alloys: dependence on alloy composition and correlation with deformation texture. *Materials Science and Engineering: A*, 344 (1-2), 20-30.

[36] VALIEV, R. Z., ISLAMGALIEV, R. K., ALEXANDROV, I. V. (2000). Bulk nanostructured materials from severe plastic deformation. *Progress in Materials Science*, 45 (2), 103–189.

[37] SCHAFLER, E., STEINER, G., KORZNIKOVA, E., KERBER, M., ZEHETBAUER, M. J. (2005). Lattice defect investigation of ECAP-Cu by means of X-ray line profile analysis, calorimetry and electrical resistometry. *Materials Science and Engineering: A*, 410–411, 169-173.

[38] VINOGRADOV, A. (2015). Mechanical Properties of Ultrafine-Grained Metals: New Challenges and Perspectives. *Advanced Engineering Materials*, 17 (12), 1710-1722.

[39] HALL, E. O. (1951). The Deformation and Ageing of Mild Steel: III Discussion of Results. *Proceedings of the Physical Society. Section B*. 64 (9), 747-753.

[40] PETCH, N. J. (1953). The Cleavage Strength of Polycrystals. *Journal of the Iron and Steel Institute*, 174, 25–28.

[41] SEGAL, V. M. (1995). Materials processing by simple shear. *Materials Science and Engineering: A,* 197 (2), 157–164.

[42] VALIEV, R. Z., LANGDON, T. G. (2006). Principles of equal-channel angular pressing as a processing tool for grain refinement. *Progress in Materials Science*, 51 (7), 881–981.

[43] BRIDGMAN, P. W. (1943). On torsion combined with compression. *Journal of Applied Physics*, 14 (6), 273-283.

[44] LANGDON, T. G. (2013). Twenty-five years of ultrafine-grained materials: Achieving exceptional properties through grain refinement. *Acta Materialia*, 61 (19), 7035-7059.

[45] SAITO, Y., UTSUNOMIYA, H., TSUJI, N., SAKAI, T. (1999). Novel ultra-high straining process for bulk materials—development of the accumulative roll-bonding (ARB) process. *Acta Materialia*, 47 (2), 579-583.

[46] FARAJI, G., KIM, H. S., KASHI, H. T. (2018). *Severe Plastic Deformation : Methods, Processing and Properties.* 1st edition. Elsevier. ISBN: 9780128135679.

[47] IWAHASHI, Y., WANG, J., HORITA, Z., NEMOTO, M., LANGDON, T. G. (1996). Principle of equal-channel angular pressing for the processing of ultra-fine grained materials. *Scripta Materialia*, 35 (2), 143-146. https://doi.org/10.1016/1359-6462(96)00107-8

[48] RAAB, G. I., SOSHNIKOVA, E. P., VALIEV R. Z. (2004). Influence of temperature and hydrostatic pressure during equal-channel angular pressing on the microstructure of commercial-purity Ti. *Materials Science and Engineering: A*, 387-389, 674-677.

[49] KRYSTIAN, M., HORKY, J., COLAS, D., NEODO, S., DIOLOGENT, F. (2019). Microstructure, mechanical properties, and thermal stability of lean, copper-free silver alloy subjected to equal channel angular pressing (ECAP) and subsequent post-processing. *Materials Science and Engineering: A*, 757, 52-61.

[50] AFIFI, M. A., PEREIRA, P. H. R., WANG, Y. C., WANG, Y., LI, S., LANGDON, T.G. (2017). Effect of ECAP processing on microstructure evolution and dynamic compressive behavior at different temperatures in an Al-Zn-Mg alloy. *Materials Science and Engineering: A*, 684, 617-625.

[51] BLUM, W., LI, Y. J., ZHANG, Y., WANG, J. T. (2011). Deformation resistance in the transition from coarse-grained to ultrafine-grained Cu by severe plastic deformation up to 24 passes of ECAP. *Materials Science and Engineering: A*, 528 (29-30), 8621-8627.

[52] RAAB, G. J., VALIEV, R. Z., LOWE, T. C., ZHU, Y. T. (2004). Continuous processing of ultrafine grained Al by ECAP-Conform. *Materials Science and Engineering: A*, 382 (1-2), 30–34.

[53] PALÁN, J., PROCHÁZKA, R., ZEMKO, M. (2017). The microstructure and mechanical properties evaluation of UFG Titanium Grade 4 in relation to the technological aspects of the CONFORM SPD process. *Procedia Engineering*, 207, 1439-1444.

[54] NÉMETH, G., HORVÁTH, K., HERVOCHES, C., CEJPEK, P., PALÁN, J., DUCHEK, M., MÁTHIS, K. (2018). Characterization of the Microstructure, Local Macro-Texture and Residual Stress Field of Commercially Pure Titanium Grade 2 Prepared by CONFORM ECAP. *Metals*, 8 (12), 1000.

[55] RAUSCHNABEL, E., SCHMIDT, V. (1992). Modern applications of radial forging and swaging in the automotive industry. *Journal of Materials Processing Technology*, 35 (3-4), 371-383.

[56] MERTOVÁ, K, PALÁN, J, DUCHEK, M, STUDECKÝ, T, DŽUGAN, J, POLÁKOVÁ, I. (2020). Continuous Production of Pure Titanium with Ultrafine to Nanocrystalline Microstructure. *Materials,* 13 (2), 336.

[57] TOTTEN, G., HOWES, M, INOUE, T. (2002). *Handbook of Residual Stress and Deformation of Steel*. ASM International, Materials Park, OH. ISBN: 978-0-87170-729-1.

[58] KUNČICKA, L., KOCICH, R., HERVOCHES, C., MACHÁČKOVA, A., (2017). Study of structure and residual stresses in cold rotary swaged tungsten heavy alloy. *Materials Science and Engineering: A*, 704, 25-31.

[59] SCHAJER, G. S. (2013). *Practical Residual Stress Measurement Methods*. John Wiley & Sons. The Atrium, Southern Gate, Chichester, West Sussex, PO19 8SQ, United Kingdom. ISBN 978-1-118-34237-4

[60] LU, J., SOCIETY for EXPERIMENTAL MECHANICS (U.S.) (1996). *Handbook of Measurement of Residual stresses.* 1st edition. Fairmont Press, Lilburn, GA. ISBN: 978-0132557382.

[61] ROSSINI, N. S., DASSISTI, M., BENYOUNIS K. Y., OLABI A. G. (2012). Methods of measuring residual stresses in components. *Materials and Design*, 35, 572-588.

[62] WITHERS, P. J. (2017). Mapping residual and internal stress in materials by neutron diffraction. *Comptes Rendus Physique*, 8 (7-8), 806-820.

[63] WEBSTER, G. A., WIMPORY, R. W. OHMS, C., YOUTSOS, A. G. (2002). *Polycrystalline materials – determinations of residual stresses by neutron diffraction*. ISO/TTA3 International Standardization Organization, Technology Trends Assessment, Geneva. ISSN 1018-5593.

[64] HUTCHINGS, M. T., WITHERS, P. J., HOLDEN, T. M., LORENTZEN, T. (2005). *Introduction to the Characterization of Residual Stress by Neutron Diffraction*. 1st edition. CRC Press Taylor & Francis, Boca Raton, FL. ISBN 9780429220791.

[65] VOIGT, W. (1966). *Lehrbuch der Kristallphysik (mit Ausschluss der Kristalloptik).* Vieweg + Teubner Verlag, Springer Fachmedien Wiesbaden. ISBN 978-3-663-15884-4.

[66] REUSS, A. (1929). Berechnung der fliessgrenze von mischkristallen auf grund der plastizitötsbedingung fur einkristalle. *ZAMM - Zeitschrift für Angewandte Mathematik und Mechanik*, 9 (1), 49–58.

[67] ESHELBY, J. D. (1957). The determination of the elastic field of an ellipsoidal inclusion and related problems. *Proceedings of the Royal Society A*, 241 (1226), 376–396.

[68] GNÄUPEL-HEROLD, T., CREUZIGER, A. A., IADICOLA, M. (2012). A model for calculating diffraction elastic constants. *Journal of Applied Crystallography*, 45 (2), 197-206.

[69] MIKULA, P., KULDA, J., VRÁNA, M., CHALUPA, B. (1984). Proposal for a highly efficient double-crystal monochromator for thermal neutrons. *Journal of Applied Crystallography*, 17 (3), 189-195.

[70] MIKULA, P., LUKÁŠ, P., MICHALEC, R. (1987). An experimental test of an elastically bent silicon crystal as a thermal-neutron monochromator. *Journal of Applied Crystallography*, 20 (5), 428-430.

[71] www.ujf.cas.cz/cs/oddeleni/oddeleni-neutronove-fyziky/instruments/lvr15

[72] LITVINENKO, E. I., RYUKHTIN, V., BOGDZEL, A. A., CHURAKOV, A. V., FARKAS, G., HERVOCHES, C., LUKÁŠ, P., PILCH, J., ŠAROUN, J., STRUNZ P., ZHURAVLEV, V. V. (2017). Upgrade of detectors of neutron instruments at Neutron Physics Laboratory in Řež. *Nuclear Instruments and Methods in Physics Research, Section A: Accelerators, Spectrometers, Detectors and Associated Equipment*, 841, 5-11.

[73] BORBÉLY, A., GROMA, I. (2001). Variance method for the evaluation of particle size and dislocation density from x-ray Bragg peaks. *Applied Physics Letters,* 79 (12), 1772–1774.

[74] BORBÉLY, A., DRAGOMIR-CERNATESCU, J., RIBÁRIK, G., UNGÁR, T. (2003). Computer program ANIZC for the calculation of diffraction contrast factors of dislocations in elastically anisotropic cubic, hexagonal and trigonal crystals. *Journal of Applied Crystallography,* 36 (1), 160-162.

[75] http://ebsd.com/images/articles/10/fig_1b.jpg

[76] SCHWARZER, R. A., ZAEFFERER, S. (1994). An Inexpensive CCD Camera System for the Recording and On-Line Interpretation of TEM Kikuchi Patterns. *Materials Science Forum,* 157–162, 189–194.

[77] RAUCH, E. F., VERON, M. (2005). Coupled microstructural observations and local texture measurements with an automated crystallographic orientation mapping tool attached to a tem. *Materialwissenschaft und Werkstofftechnik*, 36 (10), 552–556.

[78] HIELSCHER, R., SILBERMANN, C. B., SCHMIDL, E., IHLEMANN, J. (2019). Denoising of crystal orientation maps. *Journal of Applied Crystallography,* 52 (5), 984-996.

[79] ŠAROUN, J., KULDA, J. (2004). Neutron ray-tracing simulations and data analysis with RESTRAX. *SPIE proceedings*, 5536, 124-133.

[80] ŠAROUN, J., KORNMEIER, J. R., HOFMANN, M., MIKULA, P., VRÁNA, M. (2013). Analytical model for neutron diffraction peak shifts due to the surface effect. *Journal of Applied Crystallography,* 46 (3), 628-638.

[81] MULCHRONE, K. F., CHOUDHURY, K. R. (2004). Fitting an ellipse to an arbitrary shape: implications for strain analysis. *Journal of Structural Geology*, 26 (1), 143-153.

[82] CHEN, Y. J., LI, Y. J., WALMSLEY, J. C., DUMOULIN, S., SKARET, P. C., ROVEN, H. J. (2010), Microstructure evolution of commercial pure

titanium during equal channel angular pressing. *Materials Science and Engineering: A*, 527 (3), 789-796.

[83] WROŃSKI, M., WIERZBANOWSKI, K., WOJTAS, D., SZYFNER, E., VALIEV, R. Z., KAWAŁKO, J., BERENT, K., SZTWIERTNIA, K. (2018). Microstructure, Texture and Mechanical Properties of Titanium Grade 2 Processed by ECAP (Route C). *Metals and Materials International*. 24 (4), 802–814.

[84] DYAKONOV, G. S., MIRONOV, S., SEMENOVA, I. P., VALIEV, R. Z., SEMIATIN, S. L. (2017). Microstructure evolution and strengthening mechanisms in commercial-purity titanium subjected to equal-channel angular pressing. *Materials Science and Engineering: A*, 701, 289-301.

[85] THAM, Y. W., FU, M. W., HNG, H. H., PEI, Q. X., LIM, K. B. (2007). Microstructure and Properties of Al-6061 Alloy by Equal Channel Angular Extrusion for 16 Passes. *Materials and Manufacturing Processes*, 22 (7-8), 819-824.

[86] MINÁRIK, P., KRÁL, R., PEŠIČKA, J., CHMELÍK, F. (2015). Evolution of mechanical properties of LAE442 magnesium alloy processed by extrusion and ECAP. *Journal of Materials Research and Technology*, 4 (1), 75-78.

[87] XU, C., FURUKAWA, M., HORITA, Z., LANGDON, T. G. (2005). The evolution of homogeneity and grain refinement during equal-channel angular pressing: A model for grain refinement in ECAP. *Materials Science and Engineering: A*, 398 (1-2), 66-76.

[88] PROCHÁZKA, R., SLÁMA, P., DLOUHÝ, J., KONOPÍK, P., TROJANOVÁ, Z. (2020). Local Mechanical Properties and Microstructure of EN AW 6082 Aluminium Alloy Processed via ECAP–Conform Technique. *Materials*, 13 (11), 2572.

[89] BEAUSIR, B., TÓTH, L. S., NEALE, K. W. (2007). Ideal orientations and persistence characteristics of hexagonal close packed crystals in simple shear. *Acta Materialia,* 55 (8), 2695-2705.

[90] SUWAS, S., MONDAL, S. (2019). Texture Evolution in Severe Plastic Deformation Processes. MATERIALS TRANSACTIONS, 60 (8), 1457-1471.

[91] SUWAS, S., BEAUSIR B., TÓTH, L. S., FUNDENBERGER, J.-J., GOTTSTEIN, G. (2011). Texture evolution in commercially pure titanium

after warm equal channel angular extrusion. *Acta Materialia*, 59 (3), 1121-1133.

[92] TÓTH, L. S., MASSION, R. A., GERMAIN, L., BAIK, S. C., SUWAS, S. (2004). Analysis of texture evolution in equal channel angular extrusion of copper using a new flow field. *Acta Materialia*, 52 (7), 1885-1898.

[93] BOZZOLO, N., DEWOBROTO, N., GROSDIDIER, T., WAGNER, F. (2005). Texture evolution during grain growth in recrystallized commercially pure titanium. *Materials Science and Engineering: A*, 397 (1-2), 346-355.

[94] GUNDEROV, D. V., POLYAKOV, A. V., SEMENOVA, I. P., RAAB, G. I., CHURAKOVA, A. A., GIMALTDINOVA, E. I., SABIROV, I., SEGURADO, J., SITDIKOV, V. D., ALEXANDROV, I. V., ENIKEEV, N. A., VALIEV, R. Z. (2013). Evolution of microstructure, macrotexture and mechanical properties of commercially pure Ti during ECAP-conform processing and drawing. *Materials Science and Engineering: A*, 562, 128-136.

[95] ATTARILAR, S., SALEHI, M.-T., DJAVANROODI, F. (2019). Microhardness evolution of pure titanium deformed by equal channel angular extrusion. Metallurgical Research & Technology, 116 (4), 408.

[96] DIAS, A. M., PINA, J., BATISTA, A. C., DIOGO, E. (2002). About the Effect of Residual Stresses on Microhardness Readings. *Materials Science Forum,* 404-407, 349-354.

[97] BALASUBRAMANIAN, N., LANGDON, T. G. (2016). The Strength–Grain Size Relationship in Ultrafine-Grained Metals. *Metallurgical and Materials Transactions A*, 47 (12), 5827–5838.

[98] QU, J., CHERKAOUI M. (2006). *Fundamentals of micromechanics of solids*. John Wiley & Sons, Hoboken, NJ. ISBN: 978-0-471-46451-8

[99] PARNELL, W. J. (2016). The Eshelby, Hill, Moment and Concentration Tensors for Ellipsoidal Inhomogeneities in the Newtonian Potential Problem and Linear Elastostatics. *Journal of Elasticity,* 125 (2), 231–294.

[100] KIM, H. S. (2001). Finite element analysis of equal channel angular pressing using a round corner die. *Materials Science and Engineering: A*, 315 (1-2), 122–128.

[101] EL AAL, M. I. A. (2017). 3D FEM simulations and experimental validation of plastic deformation of pure aluminum deformed by ECAP and

combination of ECAP and direct extrusion. *Transactions of Nonferrous Metals Society of China,* 27 (6), 1338−1352.

[102] MURUGAN, N., NARAYANAN, R. (2009). Finite element simulation of residual stresses and their measurement by contour method. *Materials & Design*, 30 (6), 2067-2071.

[103] RIZZUTI, S., UMBRELLO, D., FILICE, L. SETTINERI, L. (2010). Finite element analysis of residual stresses in machining. *International Journal of Material Forming*, 3 (1), 431–434.

[104] LEE, H. H., GANGWAR, K. D., PARK, K.-T., WOO, W., KIM, H. S. (2017). Neutron diffraction and finite element analysis of the residual stress distribution of copper processed by equal-channel angular pressing. *Materials Science and Engineering: A*, 682, 691-697.

[105] STRUNZ, P., KOCICH, R., CANELO-YUBERO, D., MACHÁČKOVÁ, A., BERAN, P., KRÁTKÁ, L. (2020). Texture and Differential Stress Development in W/Ni-Co Composite after Rotary Swaging. *Materials*, 13 (12), 2869.

[106] ASHBY, M. F. (1970). The deformation of plastically non-homogeneous materials. *The Philosophical Magazine: A Journal of Theoretical Experimental and Applied Physics*, 21 (170), 399-424.

[107] NYE, J. F. (1953). Some geometrical relations in dislocated crystals. *Acta Metallurgica*, 1 (2), 153-162.

[108] PANTLEON, W. (2008). Resolving the geometrically necessary dislocation content by conventional electron backscattering diffraction. *Scripta Materialia*, 58 (11), 994-997.

[109] HUGHES, D. A., HANSEN, N., BAMMANN D. J. (2003). Geometrically necessary boundaries, incidental dislocation boundaries and geometrically necessary dislocations. *Scripta Materialia*, 48 (2), 147-153.

[110] WANG, M., WANG, Y., HUANG, A., GAO, L., LI, Y. HUANG, C. (2018). Promising Tensile and Fatigue Properties of Commercially Pure Titanium Processed by Rotary Swaging and Annealing Treatment. *Materials*, 11 (11), 2261.

[111] MENG, A., CHEN, X., NIE, J., GU, L., MAO, Q., ZHAO, Y. (2021). Microstructure evolution and mechanical properties of commercial pure

titanium subjected to rotary swaging. *Journal of Alloys and Compounds,* 859, 158222.

[112] MORENO-VALLE, E. C., PACHLA, W., KULCZYK, M., SAVOINI, B., MONGE, M. A., BALLESTEROS, C., SABIROV, I. (2013). Anisotropy of uni-axial and bi-axial deformation behavior of pure Titanium after hydrostatic extrusion. *Materials Science and Engineering: A*, 588, 7-13.

[113] ZHEREBTSOV, S., LOJKOWSKI, W., MAZUR, A., SALISHCHEV, G. (2010). Structure and properties of hydrostatically extruded commercially pure titanium. *Materials Science and Engineering: A*, 527 (21-22), 5596-5603.

[114] LIANG, S. J., LIU, Z. Y., WANG, E. D. (2008). Microstructure and mechanical properties of Mg-Al-Zn alloy deformed by cold extrusion. *Materials Letters*, 62 (17-18), 3051-3054.

[115] MABUCHI, M., CHINO, Y., IWASAKI, H., AIZAWA, T., HIGASHI, K. (2001). The grain size and texture dependence of tensile properties in extruded Mg-9Al-1Zn. *Materials Transactions*, 42 (7), 1182-1189.

[116] WANG, Y. M., MA, E. (2004). Strain hardening, strain rate sensitivity, and ductility of nanostructured metals. *Materials Science and Engineering: A*, 375-377, 46-52.

[117] JIA, D., WANG, Y. M., RAMESH, K. T., MA, E., ZHU, Y. T., VALIEV, R. Z. (2001), Deformation behavior and plastic instabilities of ultrafine-grained titanium. *Applied Physics Letters*, 79 (5), 611-613.

[118] ELIAS, C. N., MEYERS, M. A., VALIEV, R. Z., MONTEIRO, S. N. (2013). Ultrafine grained titanium for biomedical applications: An overview of performance. *Journal of Materials Research and Technology*, 2 (4), 340-350.

[119] SALEM, A. A., KALIDINDI, S. R., DOHERTY, R. D. (2003). Strain hardening of titanium: Role of deformation twinning. *Acta Materialia*, 51 (14), 4225-4237.

[120] LI, Z., WANG, B., ZHAO, S., VALIEV, R. Z., VECCHIO, K. S., MEYERS, M. A. (2017). Dynamic deformation and failure of ultrafine-grained titanium. *Acta Materialia*, 125, 210-218.

[121] BAUDOIN, P., HAMA, T., TAKUDA, H. (2019). Influence of critical resolved shear stress ratios on the response of a commercially pure titanium

oligocrystal: Crystal plasticity simulations and experiment. *International Journal of Plasticity*, 115, 111-131.

List of publications

TROJANOVÁ, Z., MATHIS, K., LUKÁČ, P., NÉMETH, G., CHMELÍK F. (2011). Internal stress and thermally activated dislocation motion in an AZ63 magnesium alloy. *Materials Chemistry and Physics,* 130 (3), 1146-1150.

MOLNÁROVÁ, O., MÁLEK, P., NÉMETH, G., KOZLÍK, J., LUKÁČ, F., CHRASKA, T., CINERT, J. (2016). The investigation of an Al7075 alloy prepared by spark plasma sintering of milled powders. *METAL 2016 - 25th Anniversary International Conference on Metallurgy and Materials, Conference Proceedings,* 1200-1205.

TROJANOVÁ, Z., LUKÁČ, P., MINÁRIK, P., NÉMETH, G., GUPTA, M., SEETHARAMAN, S., DI FABIO, G. (2016). Influence of inconel particles on mechanical and physical properties of an extruded magnesium. *METAL 2016 - 25th Anniversary International Conference on Metallurgy and Materials, Conference Proceedings,* 1248-1253.

TROJANOVÁ, Z., DŽUGAN, J., HALMEŠOVÁ, K., NÉMETH, G., MINÁRIK, P., LUKÁČ, P., BOHLEN, J. (2018). Influence of accumulative roll bonding on the texture and tensile properties of an AZ31 magnesium alloy sheets. *Materials,* 11 (1), 73.

TROJANOVÁ, Z., DŽUGAN, J., HALMEŠOVÁ, K., NÉMETH, G., MINÁRIK, P., LUKÁČ, P. (2018). Effect of accumulative roll bonding of an AZ31 alloy on the microstructure and tensile stress. *Acta Physica Polonica A,* 134 (3), 863-866.

NÉMETH, G., HORVÁTH, K., HERVOCHES, C., CEJPEK P., PALÁN, J., DUCHEK, M., MATHIS K. (2018). Characterization of the microstructure, local macro-texture and residual stress field of commercially pure Titanium grade 2 prepared by CONFORM ECAP. *Metals,* 8 (12), 1000.

PALÁN, J., PROCHÁZKA, R., DŽUGAN, J., NACHÁZEL, J., DUCHEK, M., NÉMETH, G., MATHIS, K., MINÁRIK, P., HORVÁTH, K. (2018). *Materials,* 10 (12), 2522.

MATHIS, K., DROZDENKO, D., NÉMETH, G., HARJO, S., GONG, W., AIZAWA K., YAMASAKI, M., KAWAMURA, Y. (2019). In-situ Investigation of the Microstructure Evolution in Long-Period-Stacking-Ordered (LPSO) Magnesium Alloys as a Function of the Temperature. *Frontiers in Materials,* 6, 270.

TROJANOVÁ, Z., DROZD, Z., ŠKRABAN, T., MINÁRIK, P., DŽUGAN, J., HALMEŠOVÁ, K., NÉMETH, G., LUKÁČ, P., CHMELÍK, F. (2020). Effect of Rotary Swaging on Microstructure and Mechanical Properties of an AZ31 Magnesium Alloy. *Advanced Engineering Materials,* 22 (1), 1900596.

TROJANOVÁ, Z., DROZD, Z., LUKÁČ, P., MINÁRIK, P., NÉMETH, G., SEETHARAMAN, S., DŽUGAN, J., GUPTA, M. (2020). Magnesium reinforced with inconel 718 particles prepared ex situ-microstructure and properties. *Materials,* 13 (3), 798.

MERTOVÁ, K., PALÁN, J., NÉMETH, G., FINTOVÁ, S., DUCHEK, M., STUDECKÝ, T., VESELÝ, J., MATHIS, K., DŽUGAN, J., TROJANOVÁ, Z. (2020). Optimization of the mechanical performance of titanium for biomedical applications by advanced, high-gain spd technology. *Crystals,* 10 (6), 422.

TROJANOVÁ, Z., DROZD, Z., HALMEŠOVÁ, K., DŽUGAN, J., ŠKRABAN, T., MINÁRIK, P., NÉMETH, G., LUKÁČ, P. (2021). Strain hardening in an AZ31 alloy submitted to rotary swaging. *Materials,* 14 (1), 157.